ISSN 2078-7405

МІНІСТЕРСТВО ОСВІТИ ТА НАУКИ УКРАЇНИ

РІЗАННЯ ТА ІНСТРУМЕНТИ

В ТЕХНОЛОГІЧНИХ СИСТЕМАХ

102’2025

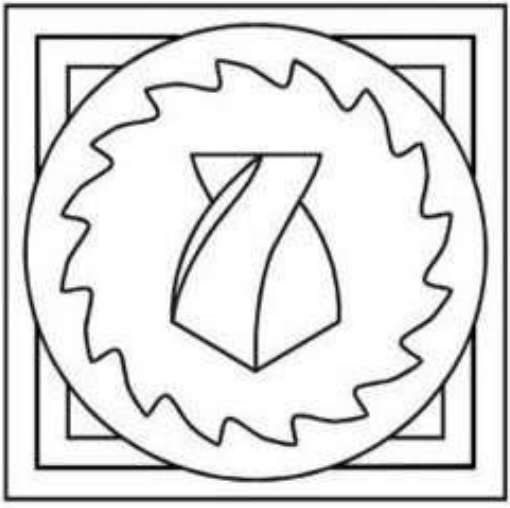

МІНІСТЕРСТВО ОСВІТИ ТА НАУКИ УКРАЇНИ

НАЦІОНАЛЬНИЙ ТЕХНІЧНИЙ УНІВЕРСИТЕТ
«ХАРКІВСЬКИЙ ПОЛІТЕХНІЧНИЙ ІНСТИТУТ»

Ministry of Education & Science of Ukraine
National Technical University
«Kharkiv Polytechnic Institute»

РІЗАННЯ ТА ІНСТРУМЕНТИ в технологічних системах

CUTTING & TOOLS IN TECHNOLOGICAL SYSTEM

Збірник наукових праць
Collection of scientific papers

Заснований у 1966 р. М. Ф. Семко
Found by M. F. Semko in 1966

ВИПУСК № 102
Edition № 102

Харків НТУ «ХПІ» – 2025 – Kharkiv NTU «KhPI»

ISSN (print) 2078-7405
УДК 621.91

Ідентифікатор медіа R30-02559, згідно з рішенням Національної ради України з питань телебачення і радіомовлення від 27.07.2023 р. №598
Друкується за рішенням Вченої ради НТУ "ХПІ", протокол № 7 від 27 червня 2025 р.

У збірнику представлені наукові статті, в яких розглядаються актуальні питання в області механічної обробки різних сучасних матеріалів із застосуванням високопродуктивних технологій, нових методик, вимірювальних приладів для контролю якості оброблених поверхонь і високоефективних різальних інструментів. Розглядаються аспекти оптимізації та математичного моделювання на різних етапах технологічного процесу.

Для інженерів і наукових співробітників, що працюють в області технології машинобудування, різання матеріалів, проектування різальних інструментів в технологічних системах.

Збірник наукових праць «Різання та інструменти в технологічних системах» включений в Перелік фахових видань України категорії «Б», наказ МОН України від 17.03.2020 р., № 409

Різання та інструменти в технологічних системах/Cutting and Tools in Technological Systems: Збірник наукових праць. – Харків: НТУ «ХПІ», 2025. – Вип. 102. – 140 с.

Адреса редакційної колегії: вул. Кирпичова, 2, Харків, 61002, Національний технічний університет «Харківський політехнічний інститут», кафедра «Інтегровані технології машинобудування» ім. М.Ф. Семка, тел. +38 (057) 706-41-43.

УДК 621.91

UDC 621.923: **doi:10.20998/2078-7405.2025.102.01**

CURRENT RESEARCH IN THE DEVELOPMENT OF TREATMENT AND POLISHING TECHNOLOGIES TO OBTAIN HIGH-QUALITY SURFACES (REVIEW)

Valerii **Lavrinenko**[1][0000-0003-2098-7992], Volodymyr **Solod**[2][0000-0002-7516-9535], Yevgeniy **Ostroverkh**[3][0000-0002-8926-1324], Vladimir **Fedorovich** [3][0000-0001-7015-8653]

[1]V. Bakul Institute for Superhard Materials NAS Ukraine, Kyiv, Ukraine
[2]Dniprovsk State Technical University, Kamianske, Ukraine
[3]National Technical University «Kharkiv Polytechnic Institute», Kharkiv, Ukraine
lavrinenko@ism.kiev.ua

Received: 15 April 2025 / Revised: 25 April 2025 / Accepted: 25 May 2025 / Published: 20 June 2025

Abstract. *Modern research indicates the effectiveness of using abrasive and chemical-mechanical methods in polishing, taking into account the characteristics of the abrasives used. At the same time, for chemical-mechanical polishing (CMP), researchers consider two directions: the influence of different abrasives, i.e., emphasis on the mechanical component of CMP, and the influence of suspension, i.e., emphasis on the chemical component. As an abrasive for polishing, diamonds are used in the tool in the form of metallic Cu_6Sn_5 and polymer diamond film overlays, as well as with the use of a mixed abrasive suspension of cerium and diamond. The features of polishing Al_2O_3–SiO_2 with mixed particles and pure – SiO_2, as well as new abrasives of the core-shell type SiO_2@A-TiO_2 are separately considered. In new suspensions containing Fe, Al_2O_3, a new material is added - graphene oxide (GO), and deionized water is also used in CMP, and this is a certain modern research trend.*
Keywords: *surface finishing; chemical-mechanical polishing; diamond abrasives; graphene oxide; deionized water.*

1. Introduction

Previous practice of tool production and the use of cutting tools in industry has proven that to achieve effective and economical use of this modern high-value tool, it is necessary not only to ensure a high-quality polished surface, but also to have a proven cutting edge. This is the same for tools made of high-speed steels, when it is necessary to avoid unwanted burrs on the cutting edge, and for hard alloys, ceramics and superhard ceramics, when it is necessary to avoid chipping on the edge. This can only be achieved by finishing the cutting edge after grinding, and even polishing it, when the roughness of the front and rear surfaces of the tool is brought

to R_a 0.05 μm, or even less, which significantly increases the wear resistance of the cutting tool and the quality of the surface processed by it.

Meanwhile, there are currently studies aimed at supposedly increasing wear resistance by changing the surfaces of the cutting tool, but the roughness of these surfaces is not paid attention at all. A striking example of such neglect is the article [1], which considers increasing the wear resistance of ground hard alloy plates by chemical treatment (passivation). At the same time, the surface roughness of the original plate was 1.3±0.2 μm in terms of R_a, and the roughness of the etched surface was 0.6–0.7 μm [1]. This leads to the conclusion that the wear resistance of the etched plate increases by 2 times. It would seem to be a new word in the processing of hard alloys. But in fact, such a study only causes surprise. If we have such roughness, it usually differs by 2 times, then the wear will also differ by 2 times. But this is not the main thing. The main thing is what kind of roughness it is. In fact, the cutting inserts RNMN 120400T (as in the article [1]) with the roughness specified above are defective, because such inserts must have a surface roughness of R_a no more than 0.20 μm and be proven. That is, the above-mentioned plates of the author [1] are defective both in the initial state and in the passivated state, and conducting these studies and drawing conclusions based on them [1] is not only incorrect, but also generally unacceptable. The importance of having proven plate surfaces, and therefore cutting edges, was pointed out 50 years ago by domestic researchers: Bakul V.M., Zakharenko I.P., Shepelev A.O., Grabchenko A.I., Matyukha P.G. and others. But over time, the practice of domestic production to a certain extent leads to simplification and a certain neglect of finishing and polishing technologies, which also affects the reduction of domestic publications. Meanwhile, foreign researchers are now paying more attention to the study of finishing and polishing technologies for mechanical engineering products.

2. The state of the art in the field of research in the field of polishing cutting tool surfaces

The surface treatment of hard alloy to the atomic level is a long-standing task in the field of manufacturing and processing of materials. To obtain high-quality products from cemented carbide with complex shapes, a new process ‘chemistry enhanced shear thickening polishing’ (C-STP) using Fenton reagent is proposed in the paper [2] to obtain polishing at a speed that is twice the speed of conventional STP. In the C-STP process, the chemical reagent in the polishing slurry, due to its high chemical affinity, diffuses to the workpiece surface and reacts with the workpiece (WC-Co). The surface material WC-Co is oxidized to a reaction layer, which is easily removed due to the simultaneous mechanical action of the grains.

Based on the results of EDS and XPS analysis, Fig. 1 shows the mechanism of material removal from tungsten carbide–cobalt alloy with Fenton suspension in the C-STP process. In the first stage, the Co element on the surface of the WC–Co alloy is first oxidized to $Co(OH)_2$ by the strong oxidant •OH, since it has a lower reaction potential than WC. Subsequently, some of the WC is oxidized to WO_3. In addition, the reaction layer formed on the upper surface is loose, which means that it is easier to remove than the WC-Co alloy. In the second stage, the $Co(OH)_2$ on the surface layer of the hard alloy is quickly removed due to the abrasive particles. In the third stage, the Co element, which is a binding phase in the hard alloy, is removed. The bonds between the hard WC phase disappear, so the WC grains and its loose oxides are relatively easily removed by abrasive particles. As a result, the fresh surface is exposed again, which can accelerate the oxidation reaction, and the synergy of both chemical and mechanical action increases the efficiency of polishing the hard alloy [2].

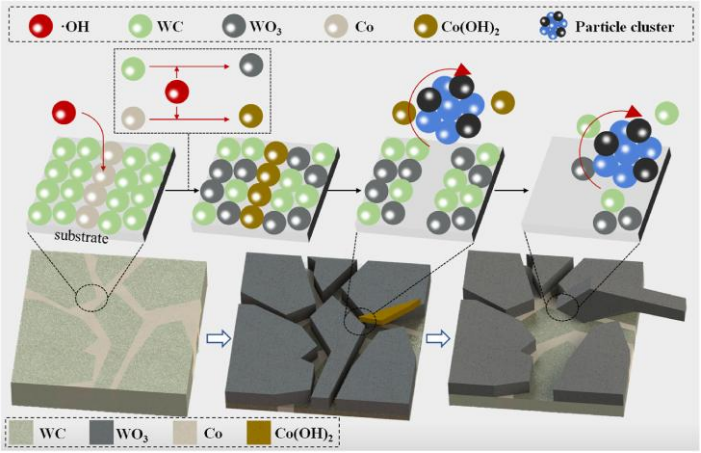

Fig. 1. Mechanism of material removal from tungsten carbide cobalt alloy by C-STP method with Fenton reagent [2].

Microdrills (Shenzhen Jinzhou Precision Technology Co., China) made of YG-6 carbide were selected to test the application of C-STP with Fenton reagent. Fig. 2(a) shows the edge shape structure of the microdrill after grinding with a diameter of 0.4 mm, with numerous defects clearly observed on the cutting edge. To solve this problem, STP and C-STP methods were used to polish the microdrill for 3 min. As shown in Fig. 2 (a), after 3 min. STP, there is still some chipping on the cutting edge and grinding marks on the front surface. The microdrill after 3 min. C-

STP (using Fenton reagent, in wt%: 0.1 H_2O_2 and 0.6 $FeSO_4$) is shown in Fig. 2 (b), where it can be seen that the cutting edge is completely smoothed and the grinding marks on the front surface are eliminated. The proposed C-STP process helped reduce the surface roughness of the carbide from the initial value of S_a 120±10 nm to 8.4±0.5 nm in less than 9 min. Elimination of microdefects on the cutting edge allows to reduce the intensity of its wear and increase the reliability and productivity of the cutting process [2].

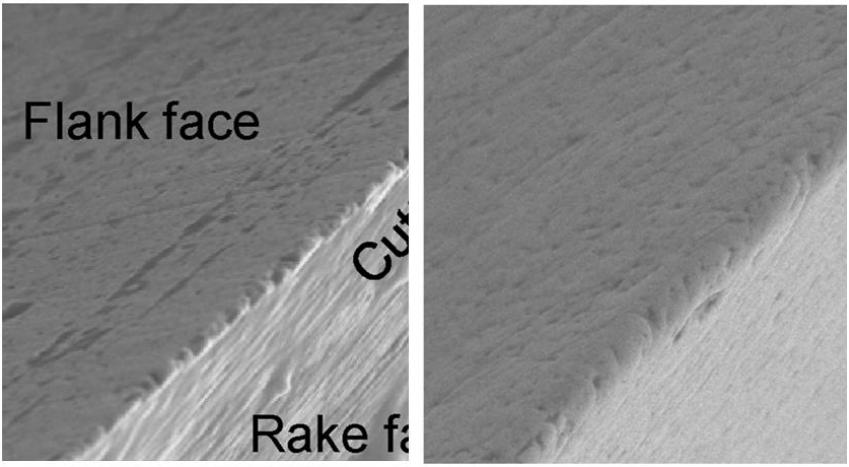

a b

Fig. 2. Comparison of the cutting edge of a microdrill: (a) edge without polishing, (b) polishing with C-STP suspension [2].

In the paper [3], an abrasive wheel for solid-state chemical-mechanical polishing (SPCMP) and effective sharpening of the cutting edge of a carbide tool (WC–Co) was developed. Measurements by X-ray diffraction and electron backscatter diffraction showed that the SPCMP method removes hidden scratches from the surface of WC–Co materials applied by a diamond wheel. Fig. 3 shows the interaction between the cutting tool and the workpiece during the cutting process. When observed under an electron microscope, the cutting edges of commercial tools have significant irregularities, which increases the contact area with the workpiece and the cutting resistance. The unevenness of the cutting edge also affects the temperature increase during cutting, and the surface of the workpiece is subjected to increased machining deformation due to the unsatisfactory shape of the cutting edge, which further increases the unevenness of the machined surface. The method of sharpening the cutting edge proposed in this work is designed to reduce the contact

area with the workpiece and the cutting resistance, and thus reduces the mechanical deformation of the machined surface. The developed grinding wheel SPCMP [3] with a diameter of 100 mm was manufactured on a phenolic binder using green silicon carbide (GC) as an abrasive component. In this study, the SPCMP grinding wheel was fabricated to avoid the transition from WC to W_2C phase during carbide machining, and to induce the oxidation of WC phase and its removal by GC. The main function of the SPCMP wheel was to obtain sharp cutting edges for carbide tools (WC–Co). When cutting with WC–Co tools with cutting edges sharpened by SPCMP, the cutting resistance was low and the wear rate was reduced. In addition, the cutting speed of WC–Co tools when cutting Ti–6Al–4V and Inconel 718 after sharpening the cutting edge with SPCMP was approximately twice that before SPCMP. It has been established that cutting heat-resistant alloys with a WC–Co tool with a sharp cutting edge leads to structural defects only near the surface, and the crystalline structure is preserved at a certain depth from the surface [3].

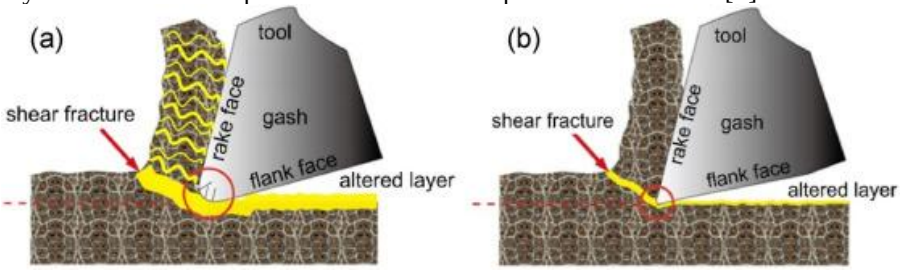

Fig. 3. Cutting with a commercial tool (a) and a tool with an edge sharpened using the technology proposed in the study [3] (b): (a) the workpiece is significantly changed by the tool during the cutting process, (b) the workpiece shows minor changes during cutting.

Bondless tungsten carbide (B-WC) is a hard and brittle ceramic material, which is mainly used for the manufacture of precision molds in the field of optics, but it is not satisfactory for precise and high-performance polishing. In the paper [4], a semi-rigid cover (SRB) tool with a radius of 40 mm is used to solve this problem. It consists of three layers. The outer and inner layers are rubber membranes with a Shore hardness of 75 HA. The middle layer is made of a 0.3 mm thick stainless steel sheet, which allows to increase the rigidity of the tool and maintain a certain flexibility. The outer rubber film is covered with a polishing pad. In [4], experiments were conducted to demonstrate the polishing and material removal characteristics of SRB on B-WC substrates. It is noted that the rough surface turned into a mirror-like surface after just 2.5 minutes of polishing. And the surface roughness in Sa was reduced from 104 nm on average to 3.7 nm. In addition, deep grinding tool marks

were effectively removed, leaving only nanometer scratches from the polishing abrasive. The results indicate that SRB is effective for rapid polishing of B-WC with good surface and subsurface quality.

The above indicates that foreign researchers pay due attention to the polishing of hard alloys and a high-quality cutting edge. At the same time, they consider the processes of chemical-mechanical [2, 3] and abrasive polishing [4]. At the same time, we will also pay attention to modern work on polishing with the use of cerium oxide, which is aimed exclusively at physical influence. Here, polishing, according to the author [5], occurs without physical contact of the lapping compound and the processed material. The removal of the processed material, the wear of cerium oxide particles and the lapping surface is a consequence of the Förster resonant energy transfer between them, which occurs in the processed surface–polishing powder–lapping surface system due to excitonic transitions between the energy levels of donor-acceptor pairs in an open microresonator [5]. That is, it is not a direct mechanical impact that is used here, but a resonant action in a microresonator between the processed material and the lapping. Such physical non-contact polishing raises more questions than answers, but in this case, we will pay attention to the fact that the most common polishing methods are divided by type of action only into: mechanical (abrasive) and chemical-mechanical, which we will consider further in a review of the most modern works of foreign researchers.

3. Formulation of the purpose of the research

The above studies indicate the effectiveness of the use of abrasive and chemical-mechanical methods in polishing and taking into account the characteristics of the abrasives used, therefore the purpose of this article was to investigate the latest (2024–2025) developments in technologies for finishing and polishing surfaces of a wide range of modern materials and to identify areas for increasing the effectiveness of such developments.

4. Presenting main material

Let us first consider developments in abrasive finishing and polishing of surfaces of various ceramic materials.

In [6], a new strategy for using the intermetallic compound Cu_6Sn_5 as a bond in a diamond grinding wheel for grinding and finishing SiC wafers with high service life and low damage processing is proposed. A ball mill for Cu_6Sn_5 powder is used to effectively reduce the particle size, increase the oxygen content and realize

the surface ceramization of the intermetallic powder. After 26 hours of ball milling, the average diameter of Cu_6Sn_5 powder decreased from 7.673 μm to 0.777 μm, and the oxygen content increased from 0.2503 to 1.613% compared to the original powder. The brittleness of the sintered Cu_6Sn_5 block increases due to the formation of Sn–O chemical bonds on the surface of the powder. The use of ball milled Cu_6Sn_5 powder as a binder for preparing diamond grinding wheels for grinding SiC wafers allowed achieving good grinding performance (Fig. 4). The maximum current of the grinding machine, wear coefficient, SiC wafer roughness and damaged layer thickness were 5.9 A, 0.22, 1.519 nm and 0.76 μm, respectively. This new strategy of using a surface-ceramic intermetallic compound as a grinding wheel bond is important for the development of a high-performance technology for grinding and finishing SiC wafers [6].

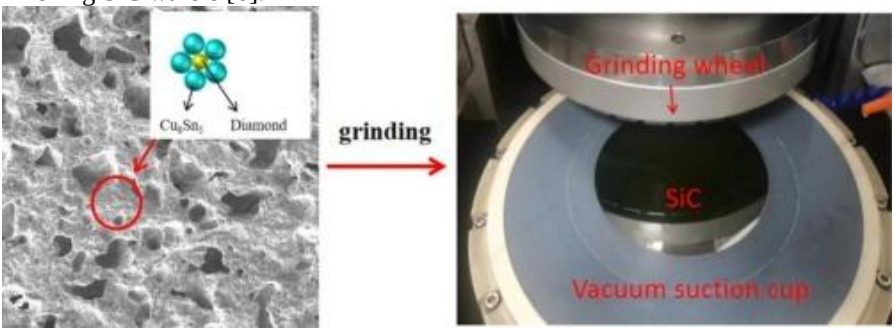

Fig. 4. Application of the intermetallic compound Cu_6Sn_5 as a bond in a diamond grinding wheel for grinding and finishing SiC plates [6].

The study [7] examined the material removal rate (MRR) for machining single-crystal SiC substrates using a fixed abrasive pad of agglomerated diamond (AD) (FADAP). At the same time, the MRR of the CMP process of a single-crystal SiC substrate reached 36.26 μm/h at a polishing pressure of 27.6 kPa and a size range of the initial AD abrasive particles of 7–10 μm. That is, the possibility of effective processing of single-crystal SiC substrates using FADAP was confirmed.

Cylindrical rollers made of Si_3N_4 ceramics serve as rolling elements of precision bearings. These rollers are especially advantageous for equipment operating under heavy loads and at high speeds. The quality of the outer surface of these rollers significantly affects both the accuracy of movement and the service life of the bearing. Considering the high hardness and brittleness of Si_3N_4 ceramics, the processing of this material is quite problematic. In the study [8], a new method of double-sided grinding using diamond film pads (DFP) for processing cylindrical Si_3N_4 rollers is presented. The results show that the maximum achievable MRR is

1.237 μm/min. The abrasive size has the greatest impact on the MRR, followed by the loading pressure and the speed ratio. Reducing the abrasive size correlates with a lower average surface roughness R_a, while using larger abrasives with a higher loading pressure and a speed ratio of 1 can reduce the R_a value. For finer abrasives, reducing the loading pressure and reducing the processing time can improve the surface roughness R_a. In this study, defect-free surfaces of ceramic cylindrical rollers with a minimum average roughness of 6 nm and a deviation of 2 nm were obtained. In addition, this process using DFP only requires the addition of deionized water, making it environmentally friendly. The principles and device of double-sided grinding using DFP for cylindrical rollers are shown in Fig. 5. Before the grinding process begins, the DFP is securely attached to both the upper and lower plates. During grinding, the spindle ensures simultaneous rotation of both the upper and lower plates, applying a constant load pressure to the workpiece. At the same time, the workpiece is rotated by the conductor, while deionized water is continuously injected as a working fluid into the grinding zone. As a result, material is removed from the workpiece surface through the abrasive action provided by film gaskets attached to the upper and lower plates [8].

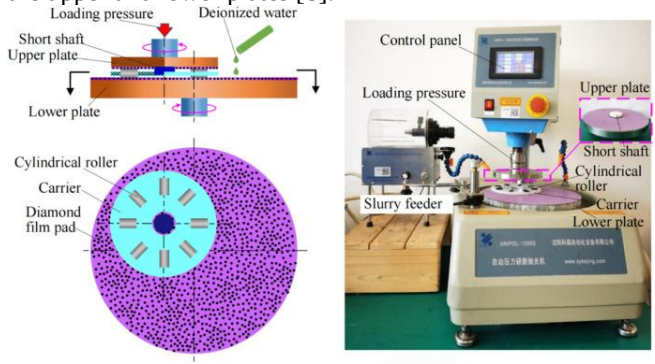

Fig. 5. Grinding principle and equipment used for double-sided grinding using DFP [8].

As we have shown above in Section 2, CMP is currently the most widely used method of material removal and surface leveling. Researchers are considering two directions: the effect of various abrasives, i.e., the emphasis on the mechanical component of CMP [9–11], and the effect of suspensions [12–18], i.e., the emphasis on the chemical component.

In the study [9], an environmentally friendly method for improving the performance of glass polishing using a mixed abrasive suspension of cerium and diamond was proposed. The addition of diamond abrasive improved the polishing

properties of the cerium-based abrasive. Polishing experiments showed that compared to a single cerium abrasive, the material removal rate (MRR) of the mixed abrasive slurry increased from 82.7 nm/min to 109.6 nm/min, while the surface roughness (Ra) decreased from 26.4 nm to 0.6 nm after polishing.

It is usually believed that abrasive particles play a role only in "mechanical wear" in CMP, neglecting their influence on chemical reactions. The study [10] reveals the chemical role of Al_2O_3 particles in ruthenium CMP by comparing the properties and polishing performance of Al_2O_3–SiO_2 mixed particles and pure SiO_2 (Fig. 6). The results show that Al_2O_3 particles enhance the mechanical impact by reducing the Zeta potential and promote the chemical action by catalyzing hydrogen peroxide to produce hydroxyl radical (Fenton-type reaction) on the Ru surface. They increase the MRR of ruthenium (Ru) in CMP with mixed abrasive particles by almost 5 times, and the surface roughness is reduced by 60%. The chemical reaction mechanism stimulated by the increase in the concentration of hydroxyl radicals on the Ru surface is confirmed by the increase in the corrosion current, the thickness of the oxide layer, and the fraction of high-valent RuO in the oxide layer. Among them, the thickened oxide layer is a significant factor contributing to the significant increase in the MRR of Ru and the decrease in the surface roughness.

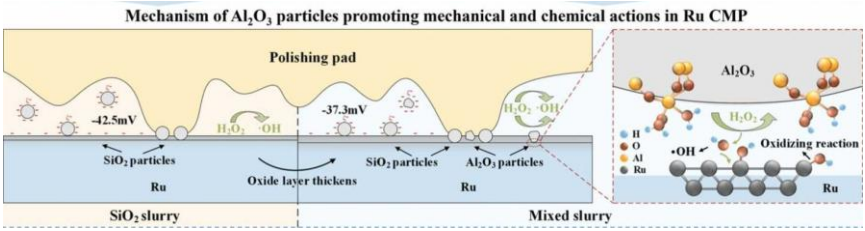

Fig. 6. Mechanism of influence of Al_2O_3 particles on mechanical and chemical effects during CMP of ruthenium [10].

It is extremely difficult to obtain an atomic surface on fused silica with a high MRR. In addition, toxic and corrosive suspensions are widely used in traditional CMP. To solve these problems, core-shell SiO_2@A-TiO_2 abrasives were fabricated and a new photocatalytic CMP was developed [11]. The developed suspension consists of sodium carbonate, hydrogen peroxide, sodium carboxymethyl cellulose and deionized water. After CMP, an atomic surface with a surface roughness Sa of 0.181 nm was obtained at a scanning area of 50×50 μm^2 and a high MRR of 10.727 μm/h. The developed SiO_2@A-TiO_2 abrasives can generate electrons and holes when irradiated with simulated sunlight, producing free radicals

(OH–) (Fig. 7). As a result, OH– combine with Si atoms on the surface of fused quartz, forming Si-OH-Si bonds. This engineered relationship between the suspension and the fused quartz surface through SiO_2@A-TiO_2 abrasives improves the synergistic effect between chemical and mechanical functions. The prepared SiO_2@A-TiO_2 abrasives with core-shell structure were applied to develop a new suspension for realizing highly efficient photocatalytic chemical-mechanical polishing of fused quartz under artificial sunlight irradiation.

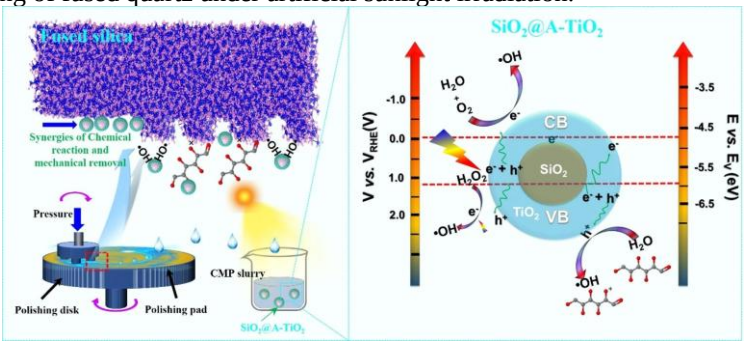

Fig. 7. Mechanism of influence of SiO_2@A-TiO_2 abrasives on mechanical and chemical actions in CMP [11].

In [12], a new approach using colloidal silica and organic salt additives for ultra-precision processing of GaN films was presented. The chemical-mechanical polishing process significantly reduced the surface roughness (S_q) to a minimum of 0.63 nm, while simultaneously increasing the material removal rate by 60 % (from 70 nm/h to 112 nm/h). Contact angle experiments confirmed the increased wettability of the slurry due to organic salts, when the contact angle between the polishing slurry and the GaN surface decreases from 20° to an angle of less than 10°.

Increasing the interfacial reactivity of the polishing slurry is crucial for improving the polishing efficiency and surface quality of sapphire wafers. In the study [13], a new green polishing slurry was developed containing aminomethylpropanol, xylitol, highly active silica, and deionized water. Experiments showed that the new green polishing slurry reduced the surface roughness by 12.5 % and increased the material removal rate by 71.3 % compared to the traditional polishing slurry. The results showed that aminomethylpropanol promotes chemical reactions between the green polishing slurry and the sapphire wafers, leading to the conversion of the intermediate product $Al(OH)_3$ to $Al(OH)_4^-$. In addition to the complexation reaction between xylitol and $Al(OH)_4^-$, it was found

that ions accelerate the removal of surface materials from sapphire plates during polishing, which leads to increased polishing efficiency and surface quality.

Planarization of silicon carbide (SiC) by CMP is a serious problem. In [14], the CMP performance of a new suspension containing Fe, Al_2O_3 and graphene oxide (GO) was investigated. Morphological characterization revealed a significant increase in Fe dispersion due to the presence of GO, as the latter, as an excellent support material, can significantly improve the catalytic performance. In addition, CMP results showed that the material removal rate (MMR) using the new slurry can reach 700 nm/h, which leads to a decrease in the average surface roughness (Sa) to 0.6175 nm. By varying the concentration of hydroxyl radical (•OH), it was found that the new slurry generates sufficient amount of •OH to oxidize the SiC surface.

The above referred to the polishing of ceramic materials, but researchers also pay due attention to the processing of metal materials.

Titanium alloy TC4 has become one of the important materials for aerospace and medical device applications due to its advantages such as good biocompatibility and high specific strength. However, the high hardness and low thermal conductivity of TC4 make it difficult to process. Therefore, a new suspension consisting of SiO_2, H_2O_2 and 2-ANA was developed for CMP of TC4 [15]. The results show that the suspension containing 2-aminobenzoic acid (2-ANA) as a chelating agent exhibits the best polishing characteristics with an R_a of 0.661 nm and a material removal rate of 173.9 nm/min. The complexing agent 2-aminobenzoic acid promotes the formation and dissolution of the oxide film. Based on the characteristics of XPS and infrared study, the following mechanism of CMP TC4 was revealed: hydrogen peroxide oxidizes the Ti element into high-valent oxides, the −N–H and −O–H groups in 2-ANA combine with metal ions in solution to form complexes, and this chemical process reaches a dynamic equilibrium with the mechanical action of abrasive grains, which ultimately provides super-smooth polishing of TC4 (Fig. 8).

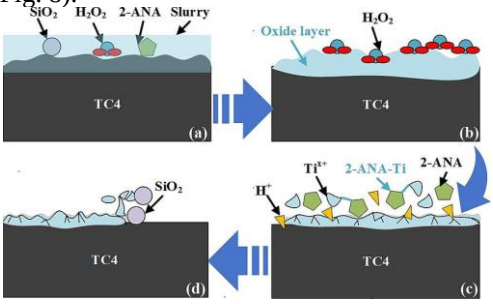

Fig. 8. Mechanism of CMP of titanium alloy TiC4 [15].

Cobalt-chromium-molybdenum (CoCrMo) alloy is characterized by good wear resistance, high corrosion resistance and excellent biocompatibility. However, high-performance devices with CoCrMo require the surface roughness R_a to be less than 1 nm, which makes ultra-precision machining difficult. To solve this problem, a new environmentally friendly CMP method containing silicon oxide, hydrogen peroxide, tartaric acid and deionized water has been developed [16]. After CMP, a surface roughness of R_a 0.16 nm is achieved for the CoCrMo alloy. X-ray, photoelectron and infrared spectroscopy showed that hydrogen peroxide dominates the oxidation processes in CMP. Co-oxides were softened and dissolved by hydrogen ions. Cr and Mo oxides showed relatively better stability and less dissolution in tartaric acid, which avoids excessive corrosion. Other oxides are removed by silica. The released metal ions are chelated by tartaric acid during the polishing process (Fig. 9).

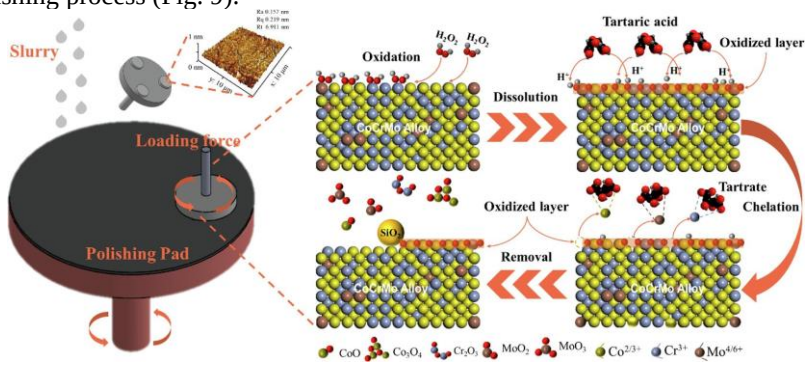

Fig. 9. CMP mechanism Cobalt-chromium-molybdenum alloy [16].

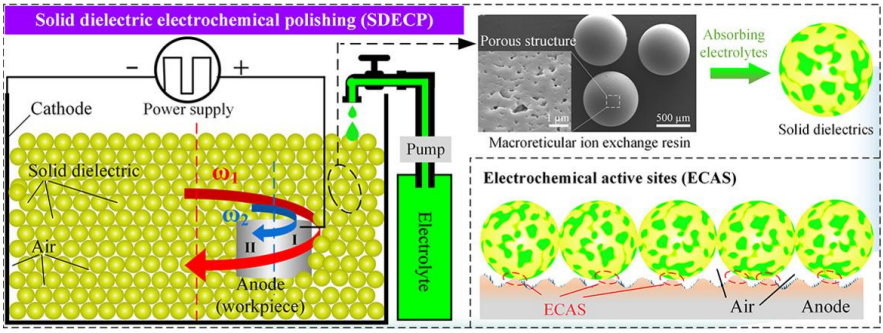

Fig. 10. Mechanism of solid dielectric electrochemical polishing (SDECP) [17].

Surface post-processing of metal additive manufacturing components is a challenging task due to their typically complex geometry (e.g., curved surfaces) combined with high initial surface roughness. In the article [17], an effective method of solid dielectric electrochemical polishing (SDECP) is proposed, which uses ion exchange resin particles with a porous structure that absorbs and stores electrolytes as a conductive medium (Fig. 10). This method improves the surface quality of additively manufactured components with Bezier curved surfaces to a specular gloss, achieving improvements in S_a, S_q, and S_z of 91.5 %, 91.7 %, and 86.9 %, respectively. The results show that the bidirectional planetary motion in SDECP effectively improves the uniformity of surface roughness and material removal in different regions of the part.

The study [18] used macroscopic CMP and microscopic atomic force microscopy to investigate the mechanism of microscratching on copper during CMP from the perspective of abrasive particles. In a near-neutral suspension containing low concentrations of H_2O_2, copper can be oxidized to cupric oxide and/or cuprous oxide, forming a brittle oxide layer that can be removed by abrasive silica particles. The removed copper oxides can adhere to the abrasive silica particles by electrostatic attraction, changing the surface state (Fig. 11). The adhered copper oxides have irregularities and high hardness, which probably causes high local contact stresses and leads to micro-scratches on the copper surface being polished. Therefore, the study showed that the adhesion of copper oxides to silica particles should be avoided.

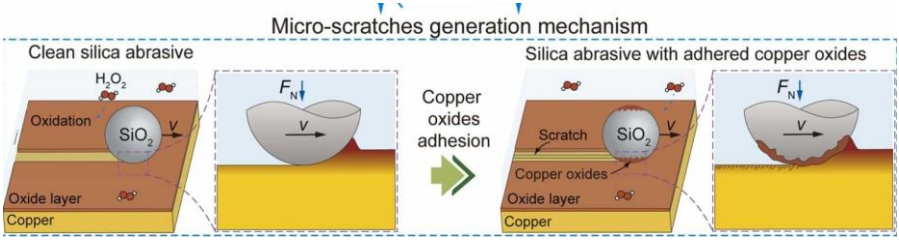

Fig. 11. Modeling the formation of scratches on the copper surface during polishing [18].

Ultra-precision surfaces of rotation are crucial for mechanical components such as bearings, but they are difficult to achieve by conventional machining. Meanwhile, it is difficult to predict the evolution law of surface roughness during machining. In the study [19], a super-precision chemical mechanical polishing (CMP) method was proposed for machining surfaces of rotation. A theoretical model of surface roughness R_a was created, assuming that the three-dimensional surface morphology can be simplified to two-dimensional identical triangles, each peak can

be removed uniformly, and the removal of material in the depressions can be neglected compared to the removal of material at the peaks (Fig. 12). The model provides an intuitive understanding of the evolution law of R_a during CMP. Interestingly, R_a initially decreases parabolically, which is determined by the initial surface roughness R_{a0}, the material removal rate MRR_V, and the polishing time t. It then stabilizes. The cylindrical guide surface of the bearing was polished using the developed CMP method. In 6 min R_a can be significantly reduced from the initial 201.09 nm to 1.50 nm almost parabolically and stabilizes. The experimental results mostly confirm the theoretical model of R_a, except that the slow reduction stage appears in the intermediate stage, since the real surface cannot be perfectly uniform. In addition, the roundness error RONt is reduced by 34 %.

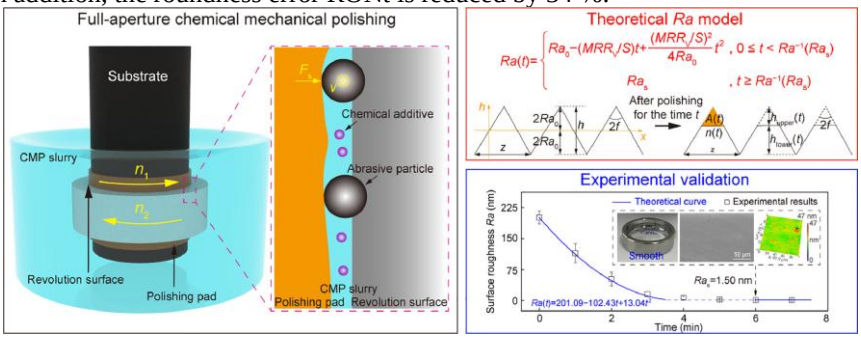

Fig. 12. CMP mechanism and theoretical model of surface roughness [19].

5. Conclusions

Thus, it is possible to draw the following conclusions from the above.

1. Modern studies indicate the effectiveness of using abrasive [6–9] and chemical-mechanical [10–18] methods in polishing, taking into account the characteristics of the abrasives used. For CMP, researchers consider two directions: the influence of different abrasives, i.e., emphasis on the mechanical component of CMP [9–11], and the influence of suspension [12–18], i.e., emphasis on the chemical component.

2. Research into the priority of the abrasive component is presented in [6] by a new strategy of using the intermetallic compound Cu_6Sn_5 as a bond in a diamond grinding wheel for grinding and finishing SiC plates with high service life and low damage processing. In the study [8], a new method of double-sided grinding using diamond film pads (DFP) for processing cylindrical Si_3N_4 rollers is presented.

In the article [9], an environmentally friendly method for improving polishing performance using a mixed abrasive suspension of cerium and diamond is proposed.

3. The study [10], as a transition from mechanical to chemical component, reveals the chemical role of abrasive Al_2O_3 particles in ruthenium CMP by comparing the properties and performance of polishing Al_2O_3–SiO_2 mixed particles and pure SiO_2. In work [11], core-shell SiO_2@A-TiO_2 abrasives were prepared in a new suspension for the implementation of highly efficient photocatalytic chemical-mechanical polishing under irradiation with artificial sunlight.

4. We will pay special attention to the use of deionized water in CMP, as this is a certain modern research trend [8, 11, 13, 18].

5. In [14], the characteristics of CMP were investigated with a new suspension containing Fe, Al_2O_3 and a new material – graphene oxide (GO), since the latter is an excellent carrier material, the characteristics of which can significantly improve the catalytic characteristics of the suspension.

References: 1. *Botvinko V.P.* Pivischennia znosostiikosti shlifovanych rizhuchih plastin z tverdych splaviv shliahom himichnoi obrobky. Instrumentalne materialoznavstvo: Zbirnuk naukovyh prats. – V. 25. Kyiv: ISM im. V.M. Bakulia NAS Ukraine, 2022. pp. 271–285. DOI 10.33839/2708-731X-24-1-271-285. **2.** Mechanism of material removal in tungsten carbide-cobalt alloy during chemistry enhanced shear thickening polishing / *Jiahuan Wang, Zewei Tang, Saurav Goel, Yu Zhou, Yanfei Dai, Jinhu Wang, Qiankun He, Julong Yuan, Binghai Lyu.* Journal of Materials Research and Technology. Volume 25, July–August 2023, pp. 6865-6879. https://doi.org/10.1016/j.jmrt.2023.07.112. **3.** *Yayoi Tanaka, Hisashi Sato, Osamu Eryu.* Improved cemented carbide tool edge formed by solid phase chemical–mechanical polishing. Journal of Materials Research and Technology. Volume 20, September–October 2022, pp. 606-615. https://doi.org/10.1016/j.jmrt.2022.07.077 **4.** Theoretical and experimental investigation of material removal in semi-rigid bonnet polishing of binderless tungsten carbide / *Xiaolong Ke, Wei Wu, Chenchun Shi, Kangsen Li, Yongheng Yu, Tianyi Wang, Bo Zhong, Zhenzhong Wang, Jiang Guo, Chi Fai Cheung, Chunjin Wang*. Journal of Materials Research and Technology. Volume 24, May–June 2023, pp. 1597-1611. https://doi.org/10.1016/j.jmrt.2023.03.090. **5.** Mechanism of polishing scintillators based on polystyrene / *Filatov Yu. D., Boyarinstsev A.Y., Sidorko V.I., Kovalev S.V., Kolesnikov O.V., Novgorodsev V.O., Polupan Ya.I.* J. Superhard Mater. 2024. Vol. 46(5). pp. 390–401. DOI 10.3103/S1063457624050034. **6.** Preparation and properties of Cu_6Sn_5 intermetallic-bonded diamond grinding wheel for thinning SiC wafer / *Shuai-peng Chen, Hao Li, Xi-yue Kang, Yao Jiang, Wen-bo Ma, Xiao-can Yan, Yue-hui He*. Diamond and Related Materials. Volume 152, February 2025, 111874. https://doi.org/10.1016/j.diamond.2024.111874. **7.** *Pengfei Wu, Ning Liu, Xue Li, Yongwei Zhu.* Material removal rate model for chemical–mechanical polishing of single-crystal SiC substrates using agglomerated diamond abrasive. Precision Engineering. Volume 88, June 2024, pp. 572-583. https://doi.org/10.1016/j.precisioneng.2024.04.002. **8.** Surface roughness and material removal of Si_3N_4 cylindrical rollers using double-side grinding with diamond film pads / *Fenfen Zhou, Yongkang Jin, Qi Shao, Weifeng Yao, Hongyun Wang*. Journal of Materials Research and Technology. Volume 34, January–February 2025, pp. 2788-2801. https://doi.org/10.1016/j.jmrt.2024.12.234. **9.** Evaluation of chemical mechanical polishing characteristics using mixed abrasive slurry: A study on polishing behavior and material removal mechanism / *Xiaoxiao Zhu, Juxuan Ding, Zhangchao Mo, Xuesong Jiang, Jifei Sun, Hao Fu, Yuziyu Gui, Boyuan Ban, Ling Wang, Jian Chen*. Applied Surface Science. Volume 679, 15 January 2025, 161157.

https://doi.org/10.1016/j.apsusc.2024.161157. **10.** Role of alumina particles in chemical-mechanical synergies in ruthenium polishing / *Hongyu Di, Ping Zhou, Yunxiang Lu, Ke Yang, Dongming Guo.* Journal of Materials Processing Technology. Volume 330, September 2024, 118477. https://doi.org/10.1016/j.jmatprotec.2024.118477. **11.** Development of core–shell SiO_2@A-TiO_2 abrasives and novel photocatalytic chemical machinal polishing for atomic surface of fused silica / *Chunjing shi, Yuanhang Fan, Zhenyu Zhang, Xingqiao Deng, Jiaxin Yu, Hongxiu Zhou, Fanning Meng, Junyuan Fen.* Applied Surface Science. Volume 652, 15 April 2024, 159293. https://doi.org/10.1016/j.apsusc.2024.159293. **12.** Exploring the mechanism of gallium nitride surface quality enhancement by green organic additives in chemical mechanical polishing / *Wenhao Xian, Baoguo Zhang, Min Liu, Dexing Cui, Shitong Liu.* Applied Surface Science. Volume 670, 15 October 2024, 160646. https://doi.org/10.1016/j.apsusc.2024.160646. **13.** *Yongchao Xu, Cheng Peng, Youji Zhan, Qianting Wang.* Machining performance and material removal mechanism of sapphire with novel polishing slurry. Applied Surface Science. Volume 671, 30 October 2024, 160756. https://doi.org/10.1016/j.apsusc.2024.160756. **14.** *Shidong Chen, Hong Lei.* Polishing performance and mechanism of a novel Fe-based slurry for chemical mechanical polishing. Tribology International. Volume 194, June 2024, 109549. https://doi.org/10.1016/j.triboint.2024.109549. **15.** A novel slurry for ultra-smooth chemical mechanical polishing of TC4 titanium alloy / *Longxing Liao, Fuli Cai, Xuefeng Chang, Chengbin Zhao, Jingyu Mo, Jian Shun.* Applied Surface Science. Volume 686, 30 March 2025, 162167. https://doi.org/10.1016/j.apsusc.2024.162167. **16.** Atomic surface of cobalt-chromium-molybdenum alloy induced by novel green chemical mechanical polishing through controlling pH values and oxidation processes / *Haoran Liu, Zhenyu Zhang, Xingqiao Deng, Jiaxin Yu, Chunjing Shi, Hongxiu Zhou, Fanning Meng, Junyuan Feng.* Applied Surface Science. Volume 652, 15 April 2024, 159356. https://doi.org/10.1016/j.apsusc.2024.159356. **17.** Solid dielectric electrochemical polishing of 3D-printed parts: Performance and mechanisms / *Shenggui Liu, Chaojiang Li, Xin Jin, Dingyifei Ma, Qi Yan, Guodong Liu, Jue Liu, Xun Cao, Hao Wang.* International Journal of Mechanical Sciences. Volume 285, 1 January 2025, 109822. https://doi.org/10.1016/j.ijmecsci.2024.109822. **18.** *Yushan Chen, Liang Jiang, Linmao Qian.* Micro-scratches generation mechanism by copper oxides adhered on silica abrasive in copper chemical mechanical polishing. Tribology International. Volume 194, June 2024, 109434. **19.** Surface roughness evolution law in full-aperture chemical mechanical polishing / *Wumao Peng, Liang Jiang, Chaopeng Huang, Yu Chen, Yiming Tian, Yanjun Han, Shaohua Zhang, Linmao Qian.* International Journal of Mechanical Sciences. Volume 277, 1 September 2024, 109387. https://doi.org/10.1016/j.ijmecsci.2024.109387. **20.** Surface roughness evolution law in full-aperture chemical mechanical polishing / *Wumao Peng, Liang Jiang, Chaopeng Huang, Yu Chen, Yiming Tian, Yanjun Han, Shaohua Zhang, Linmao Qian.* International Journal of Mechanical Sciences. Volume 277, 1 September 2024, 109387. https://doi.org/10.1016/j.ijmecsci.2024.109387.

Валерій Лавріненко, Київ, Україна, Володимир Солод, Кам'янське, Україна, Євгеній Островерх, Володимир Федорович, Харків, Україна

СУЧАСНІ ДОСЛІДЖЕННЯ В РОЗРОБЦІ ТЕХНОЛОГІЙ ДОВЕДЕННЯ ТА ПОЛІРУВАННЯ ДЛЯ ОДЕРЖАННЯ ВИСОКОЯКІСНИХ ПОВЕРХОНЬ (ОГЛЯД)

Анотація. *Попередньою практикою інструментального виробництва та застосування різального інструменту у промисловості доведено, що для досягнення ефективного та економного використання цього сучасного високовартісного інструменту треба не тільки забезпечити високоякісну шліфовану їх поверхню, але і мати доведену різальну крайку. Досягнути*

цього можливо лише доведенням після шліфування різальної крайки, а і навіть її поліруванням, коли шорсткість передньої та задньої поверхонь інструменту доводиться до R_a 0,05 мкм, а іноді навіть менше, що значно підвищує зносостійкість різального інструменту та якість обробленої ним поверхні. Сучасні дослідження свідчать про ефективність застосування при поліруванні абразивних і хіміко-механічних методів та врахуванні при цьому особливостей абразивів, які застосовуються, тому метою даної статті було дослідити найновіші (2024–2025 рр.) розробки в технологіях доведення та полірування поверхонь широкої гами сучасних матеріалів та визначити напрямки підвищення ефективності таких розробок. При цьому для хіміко-механічного полірування (CMP) дослідниками розглядається два напрямки: вплив різного абразиву, тобто наголос на механічний складовій CMP, та вплив суспензії, тобто наголос на хімічній складовій. Дослідження в напрямку пріоритетності абразивної складової представлені новою стратегією застосування інтерметалічної сполуки Cu_6Sn_5 у якості зв'язки в алмазному шліфувальному кругі для шліфування і доведення пластин SiC з високим терміном служби і обробки з низьким рівнем пошкоджень. Досліджено новий метод двостороннього шліфування із застосуванням алмазних плівкових накладок для обробки циліндричних роликів Si_3N_4. Запропонований екологічно чистий метод поліпшення продуктивності поліровки із застосуванням змішаної абразивної суспензії церію і алмаза. Дослідження , як перехідне від механічної до хімічної складової, розкриває хімічну роль абразивної Al_2O_3–частинки при CMP рутенію шляхом порівняння властивостей і продуктивності поліровки Al_2O_3–SiO_2 змішаними частинками і чистими – SiO_2. Представлені нові розробки з виготовлення абразивів типу ядро-оболонка SiO_2@A-TiO_2 в новій суспензії для реалізації високоефективної фотокаталітичної хіміко-механічної поліровки при опроміненні штучним сонячним світлом. Досліджені характеристики CMP за нової суспензії, що містила Fe, Al_2O_3 і новітній матеріал – оксид графена, оскільки останній є чудовим матеріалом-носієм, характеристики якого можуть значно поліпшити каталітичні характеристики суспензії. Окремо звернено увагу на застосування при CMP деіонізованої води, оскільки це є певним сучасним трендом досліджень.

Ключові слова: *доведення поверхні; хіміко-механічне полірування; алмазні абразиви; оксид графена; деіонізована вода.*

UDC 531.67, 621.923 **doi: 10.20998/2078-7405.2025.102.02**

MODELING THE IMPACT OF NONLINEAR OSCILLATIONS ON THE QUALITY OF THE WORKING SURFACE OF PARTS IN FINISHING OPERATIONS

Anatoliy **Usov** [0000-0002-3965-7611], Maksym **Kunitsyn** [0000-0003-1764-8922]

National University "Odessa Polytechnic", Odessa, Ukraine
usov_a_v@op.edu.ua

Received: 22 April 2025 / Revised: 29 April 2025 / Accepted: 20 May 2025 / Published: 20 June 2025

Abstract. *The paper investigates the influence of finishing operations on the roughness of machined surfaces in the case when the machine-tool-fixture-tool-part (MTFTP) system is in the zone of nonlinear oscillations. For this purpose, models of dynamic oscillatory processes accompanying the machining of working surfaces of parts are built in the Simulink system of the MATLAB package. The formation of self-excited oscillations of the MTFTP mechanical system during finishing operations is determined with one or two degrees of freedom associated with the heterogeneity of the processed material and external disturbing forces in the ranges of fundamental and subharmonic resonances containing, in addition to the excitatory element itself, also zones of dry friction of the tool with the processed surface. These studies not only demonstrate the behavior of mechanical systems capable of self-excited oscillations, but also allow their results to be successfully applied to optimize the quality characteristics of machined surfaces during finishing operations. It has been shown that resonant curves under nonlinear oscillations of mechanical systems of finishing operations affect not only the formation of the roughness of the machined surface, but also the appearance of scorch marks on them and the formation of defects such as cracks.*
Keywords: *finishing operations; nonlinear oscillations; models; Simulink system; oscillation amplitudes; stability.*

1. Introduction

Unlike an ideal surface, the surface of a part after finishing operations is not smooth, but always has microscopic irregularities that form roughness [1], [2]. Despite the rather small size of the roughness-forming irregularities, they have a significant impact on various operational properties of parts [3], [4], [5]. In the operations preceding grinding, the roughness of the machined surface affects the concentration of stresses, vibration activity, and the formation of thermal defects, which, under the influence of thermomechanical phenomena accompanying finishing operations, form cauterization, cracks, and chips on the machined surfaces [6], [7]. Numerous theoretical and experimental studies have been devoted to the study of this process [8], [9], [10]: the effect of grinding wheel wear, the creation of macro- and microrelief of the ground surface, fluctuations in thermomechanical

parameters in the contact zone of the grinding wheel with the treated surface, and vibration of the machine-tool, fixture, tool, and part (MTFTP) system.

2. Analysis of sources and problem description

Let us consider the influence of finishing operations on the roughness of machined surfaces in the case where the MTFTP system is in the zone of nonlinear oscillations. To do this, consider modeling dynamic oscillatory processes in the Simulink system of the MATLAB package [11].

The high speed of abrasive wheels when processing the working surfaces of machine parts highlights the need for the most accurate calculation of their dynamic properties, i.e., the calculation of their natural frequencies, resonance curves, maximum amplitudes, transfer functions, areas of instability, and amplitudes of self-excited vibrations in unstable areas.

The presence of nonlinear couplings, such as, for example, the gap in the connection of individual elements of the MTFTP, contact deformations, nonlinear damping forces, stochastic nature of external influences, etc., leads to the fact that existing classical methods of linear dynamics do not take into account nonlinear oscillations, and there is a need to study the dynamic properties of mechanical systems using nonlinear mechanics [12].

The formation of the quality characteristics of machined surfaces when the mechanical system of the MTFTP falls into the field of nonlinear oscillations is currently relevant.

Theoretical methods for solving these problems are approximate, they are based mostly on certain assumptions, and therefore it is almost always necessary to check the adequacy of theoretical calculations and the limits of applicability of the results obtained on models, both mathematical and simulation [13].

As for the complexity of the models under study, we can say that the main focus is on systems that can be described by a mathematical model with two degrees of freedom.

In the case of grinding, the non-linear factor is, for example, the cutting forces and friction forces in the contact zone between the tool and the surface to be machined (Fig. 1).

To study the properties of self-excited oscillations of the mechanical system of the MTFTP during finishing operations with one or two degrees of freedom associated with the influence of the heterogeneity of the processed material, external disturbing forces in the ranges of fundamental and subharmonic resonances containing, in addition to the self-exciting element, also the zone of dry friction of the tool with the processed surface [14].

The main types of the studied systems are shown in Fig. 1 and differ, on the one hand, in the number of degrees of freedom and, on the other hand, in the location of the self-exciting element.

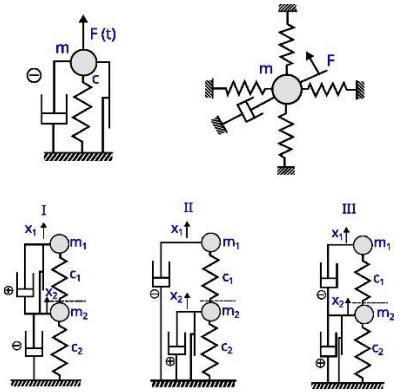

Fig. 1 Types of studied systems of MTFTP finishing operations

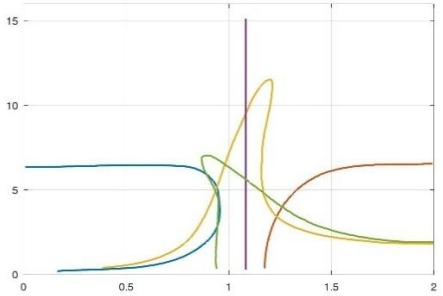

Fig. 2. An example of the behavior of a MTFTP system with one degree of freedom

In the analytical calculation of steady-state oscillations, the harmonic balance method was used, assuming a solution in the form of two independent harmonic components. The stroboscopic method based on the direct solution of the differential equations of motion was used to determine the areas of attraction.

3. Research objectives

- Develop mathematical models of the MTFTP system with one and two degrees of freedom, which take into account key nonlinearities - material heterogeneity, contact gaps, nonlinear damping and friction in finishing operations;
- Implement and simulate these models in the Simulink (MATLAB) environment to capture self-excited and forced vibrations under the conditions of fundamental and subharmonic resonance;
- Analyze the influence of nonlinear vibrations on surface quality indicators (roughness, burn-in, crack initiation) by extracting amplitude-frequency and phase-frequency characteristics from the simulated resonance curves;
- Apply harmonic balance and stroboscopy methods to isolate stability regions, forced vibrations, self-excited vibrations, and mixed modes, as well as to construct maps of their attraction;

- Quantify the impact of critical parameters - damping coefficients, frictional properties, excitation amplitude/frequency, gap size - on the amplitudes of oscillations and the resulting formation of surface defects;
- Propose and evaluate optimization strategies, such as the use of non-linear vibration dampers or adjusted friction coefficients, aimed at suppressing unwanted oscillations and improving the quality of the machined surface;
- Validate the models by comparing theoretical predictions with numerical simulation results (and experimental data, if available) to confirm the adequacy of the models and their applicability to real finishing processes.

4. Research methods

Almost all of the cases studied were verified using computational methods. Thus, the behavior of the MTFTP system in finishing operations with 1 degree of freedom is described by a differential equation with initial conditions [15], [16]:

$$\ddot{y} - (\beta - \delta y^2)\dot{y} + y + \mu y^3 = \eta^2 \cos(\eta t + \varphi)$$
$$y(t_0) = y_0, \qquad \ddot{y}(t_0) = y_{01} \tag{1}$$

where $y(t)$, $\dot{y}(t)$, $\ddot{y}(t)$ are the vertical component, the rate of change, and the acceleration of nonlinear oscillations; β, δ, μ are the coefficients of inhomogeneity of the material of the treated surface characterizing the disturbing forces; η, φ are the spectral characteristics of nonlinear oscillations, and its approximate solution $y = A\cos\eta\, t + R\cos(\omega t + \varphi)$ is shown in Fig. 2.

The amplitude of self-excited oscillations within the fundamental resonances decreases to zero. In this region, the system oscillates only by forced oscillations with amplitude A and frequencies η, Ω. Outside the resonance region, vibrations are created consisting of harmonic components with frequency Ω, which is confirmed by the numerical solution.

It is sometimes convenient to study the behavior of the MTFTP system in the stroboscopic phase plane. For a frequency $\eta = 0.8$, there is only a limiting cycle L_s corresponding to self-excited oscillations.

At an increased frequency $\eta = 1.35$, the limiting cycle L_s and the unstable center F_n reappear, but a stable special point F_s has appeared, which corresponds to stable forced oscillations. The separatrix S limits the regions of initial conditions leading to purely forced oscillations or their combination with self-excited oscillations.

Consider solving a non-homogeneous problem with a right-hand side and a constant term Q:

$$\ddot{y} - (\beta - \delta y^2)\dot{y} - ay + \mu y^3 = Q + \cos(\eta t + \varphi) \tag{2}$$

This term is manifested in a much more complex form of resonance curves, as can be seen in Fig. 3. The solution showed more significant deviations in the

subharmonic resonance region. Therefore, attention was also drawn to the mutual influence of self-excited and forced oscillations in the subharmonic resonance region of order $1/2$. These studies have brought about new information on the shapes of the resonance curves and the shape of the attraction region.

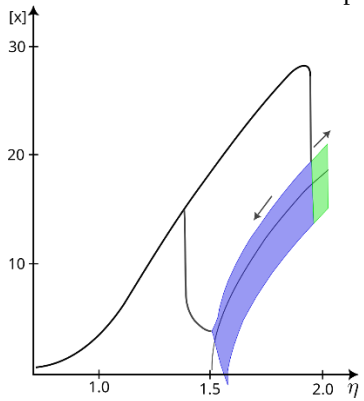

Fig. 3 Shapes of the resonance curve with a region of forced oscillations, a region of ambiguity, and a region of mixed two-frequency motion

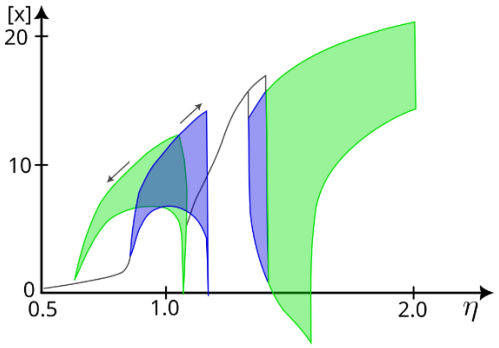

Fig. 4 Results of measurements of the change in the shape of the resonance curves at a slight change in the parameters g, $\varkappa$

Two-degree-of-freedom systems have been studied for two main types: on the one hand, for two-mass systems and, on the other hand, for systems with two degrees of freedom, but containing only 1 mass, the grinding wheel. The latter can, in the case of equality of linear stiffnesses in the x and y directions, be considered as the basic grinding model, which can include external damping, nonlinearity of restoring forces in bearings, and imbalance.

The equations of motion of a single mass case are determined by the following formulas [16]:

$$\ddot{x} + g\eta\dot{y} + \varkappa\dot{x} + \beta\eta y + [1 + \mu(x^2 + y^2)]x = \eta^2 \cos\eta t \quad (3)$$

$$\ddot{y} - g\eta\dot{x} + \varkappa\dot{y} - \beta\eta x + [1 + \mu(x^2 + y^2)]y = \eta^2 \sin\eta t \quad (4)$$

$$y(t_0) = y_0, \quad \dot{y}(t_0) = y_{01}, \quad x(t_0) = x_0, \quad \dot{x}(t_0) = x_{01}$$

where $\ddot{x}$, $\dot{x}$, x, $\ddot{y}$, $\dot{y}$, y are horizontal and vertical subharmonic vibrations and their dynamic components; y_0, y_{01}, x_0, x_{01} initial conditions g, χ, β, μ are nonlinear characteristics of the elements of the dynamic system of the MTFTP; μ is the proportionality coefficient of the movement of the system links.

Equations (3)-(4) were solved analytically and numerically. An example of the shape of the resonance curve is shown in Fig. 3, where the regions of purely forced oscillations, the region of ambiguity, and the region of mixed two-frequency motion are visible.

The measurement results of the slightly modified case are shown in Fig. 4. It can be seen that even a slight change in the grinding wheel speed parameter causes a significant change in the shape of the resonance curves. These studies made it possible to formulate the basic laws that govern the behavior of such systems.

In this paper a similar one-mass system was considered, but with respect to grinding machines [17], [18]. As a source of self-excited oscillations, in addition to the terms $(1-x^2)\dot{x}$, $(1-y^2)\dot{y}$, we considered the assumption of a coordinate relationship, which gives rise to the equation:

$$\ddot{x} + B_1 y + n_1^2 x - \varepsilon(1-x^2)\dot{x} = 0 \quad (5)$$

$$\ddot{y} + B_2 x + n_2^2 y - \varepsilon(1-y^2)\dot{y} = 0 \quad (6)$$

and, depending on the value of the constants B_1, B_2, n_1, n_2, the equilibrium state can also be either stable or unstable at $\varepsilon = 0$. The behavior of the system (Fig. 5) is depicted in the phase plane, in which the bifurcation properties of the system can be studied, i.e. the conditions under which single-frequency or two-frequency solutions exist. In this case, it was determined how to use a dry friction damper to stabilize the equilibrium state of oscillation of a self-excited system with two degrees of freedom and thereby achieve improvements in the operational properties of grinding machines. These research results have been confirmed experimentally. Thus, works [9], [19] show the occurrence of self-excited oscillations during grinding, taking into account the influence of coordinate coupling. First, the influence of the connection between the machining parameters and the roughness of the machined surface of the workpiece and the oscillating MTFTP system was taken into account.

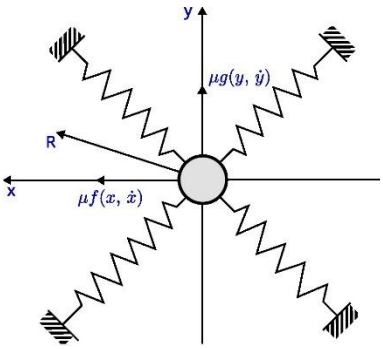

Fig. 5 Single mass system for calculating self-excited vibrations during grinding

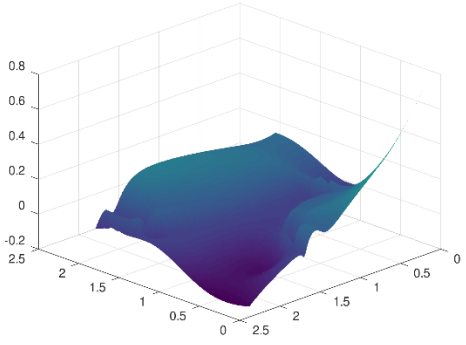

Fig. 6 An example of reduction of self-excited oscillations by changing the parameters B_1, B_2

The main means of reducing self-excited vibrations is the method of fixing the tool to an elastic base or attaching it to damping elements. This means can be applied to other elements of the MTFTP. It turns out that self-excited vibrations can be

suppressed quite successfully in a wide range of system parameters. An example of reducing oscillations by changing the image parameters is shown in Fig. 6.

These studies not only demonstrate the behavior of mechanical systems capable of self-excited oscillations, but also allow their results to be successfully applied to optimize the quality characteristics of machined surfaces in finishing operations. Self-excited oscillation can be caused in mechanical MTFTP systems for a number of reasons. One of these reasons is, for example, the connection between the processes occurring in the oscillating system and the external environment.

The instability of motion in a mechanical system can also be caused by periodic changes in the internal parameters of the system.

The amplitudes of the oscillations of the studied system, in which instabilities or significantly increased amplitudes of oscillations are formed, are determined. It is shown that the dependence of the amplitude A in the main resonance as a function of the frequency variation α and the cubic damping β in the region of relative motion oscillation is self-excited, and the influence of the frequency variation α on the multivalued resonant amplitude A is also observed. Let us consider the case of nonlinear oscillations of the mechanical system of the MTFTP described by the system of differential equations:

$$y' + \lambda y = \varepsilon \mathrm{E}y'' + \mathrm{F}y_1'' + y_2'' + \mathrm{B}y'' + \mathrm{D}y_3' + \mathrm{y}(\mathrm{Y}\cos \mathrm{k\,ar} + \mathrm{U}\sin \mathrm{k\,ar}) + \mathrm{y}_2 + \mathrm{I}\sin \mathrm{k\,ar} + \Phi(\mathrm{r}) \quad (7)$$

where y is the vector of relative motion and motion of the supports, λ is the diagonal matrix of the system eigenvalues, ε is a small parameter, B, D, E, F, Y, U, I are the matrix coefficients, and $f(t)$ is the vector of excitatory forces.

The torsional vibrations of a MTFTP mechanical system with n degrees of freedom and Hooke joints were studied. The motion is described by a linearized system of equations with periodic coefficients of the following type [16]:

$$M\ddot{q} + \varepsilon B\dot{q} + Cq + \lambda(t)q = f(t) \quad (8)$$

here ε is a small parameter; M, B, C are symmetric matrices of order n, $\lambda(t)$ is a diagonal matrix; $q(t)$ are generalized coordinates.

From the theoretical analysis based on orthonormalized transformations, the boundary curves of the instability region and the damping value conditions that ensure stability in a given speed range were obtained.

The areas of the main subharmonic and subultraharmonic resonances have been experimentally studied. The oscillation of a mechanical system is significantly complicated when shocks appear in the MTFTP system due to inhomogeneities in the surface layer of the parts to be ground or internal shocks at limited gaps in the connection of individual MTFTP elements.

These systems were analyzed using mathematical models that can be schematically represented by systems with one or two degrees of freedom, in which

the limiters are arranged differently and in which the oscillations are excited either by external harmonic forces or contain self-excited terms.

A system with two degrees of freedom and one pair of restraints is shown in Fig. 7. While the impacts occur in the lower part of the system, a device is introduced into the upper part, exerting a force $F_b - F_b$ on both masses m_1 and m_2. The form of these forces is shown in Fig. 7. The flat hysteresis curve of the excitatory effects depends on the parameters of the relative motion between the masses. Depending on the initial conditions, there are different types of motion. These types of motion also depend on the magnitude of the self-exciting force F, on the attenuation, and on the size of the gaps r_1 between the elements of the MTFTP.

An example of the regions of existence and stability of different types of motion depending on the parameters $\bar{h}$ and $\bar{r} = r_1 r_2 / F_0$ is shown in Fig. 8. At the boundaries A_1, A, there is a transition from motion without shocks to motion with shocks. The inclined shaded areas correspond to the main periodic single-impact motions with the first or second form of oscillations; the horizontally shaded areas correspond to the beating type motions. It can be seen that for some combinations of $\bar{h}$, $\bar{r}$ parameters, only one type of motion can occur, and for other combinations there are several possible types of motion.

The system with two pairs of impactors is shown in Fig. 9. The static gaps between the restraints are labeled r_1 and r_2. Since the system contains two strong non-linearities, its motion is very complex. Separate types of motion differ in the number of strokes per period of the excitation force and can exist only under certain conditions. Fig. 10 shows the regions of existence for different gap sizes: $\overline{r_1} = r_1 c / F_0$ and $\overline{r_2} = r_2 c / F_0$. The symbols z_1 and z_2 represent the number of strokes in the lower and upper regions of the change in machining modes.

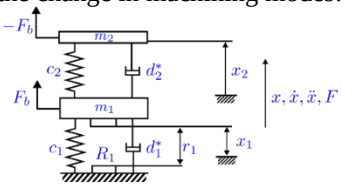

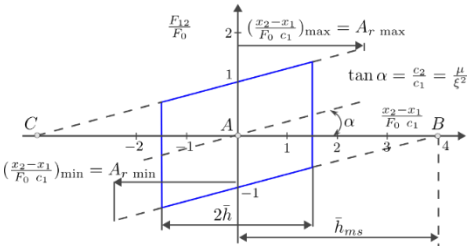

Fig. 7. The MTFTP system with two degrees of freedom and one pair of limiters

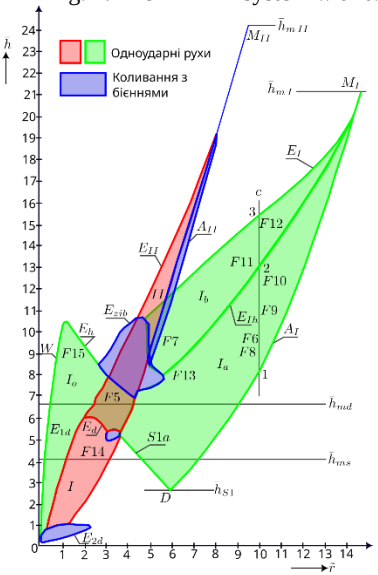

Fig. 8 An example of the region of existence and stability of different types of motion depending on the parameters $\bar{h}$ and $\bar{r} = \frac{r_1 r_2}{F_0}$

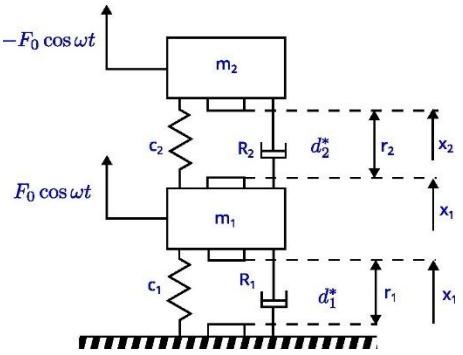

Fig. 9 A two-mass MTFTP system with static gaps r_1 and r_2 and two strong nonlinearities

These studies lead to larger-scale investigations of the effect of viscous damping and dry friction type dampers on the vibrations of systems with impacts, studies of the properties of systems containing plastic impacts, and solutions to optimal problems that allow finding the parameters of a technological system with maximum microimpact energy (for example, when the treated surface has inhomogeneities) or with minimum amplitudes in resonant regions.

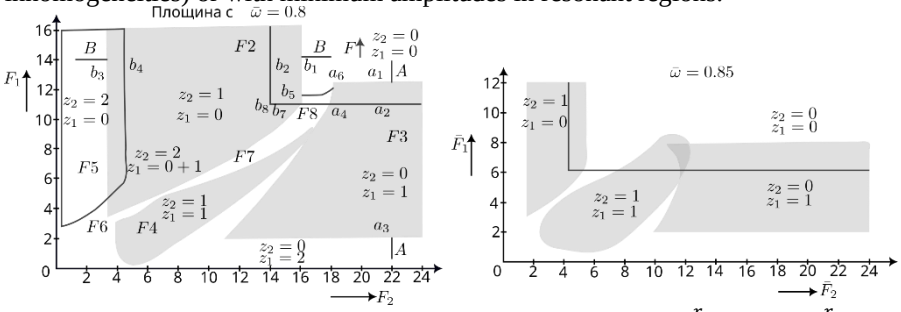

Fig. 10 Image of the region of existence at different gap sizes $\bar{r}_1 = \frac{r_1}{F_0} c$ and $\bar{r}_2 = \frac{r_2}{F_0} c$

Research on impact systems is mainly aimed at finding out the basic laws of behavior and optimization of the impact-impacted MTFTP accompanying finishing operations in terms of forming a machined surface from a heterogeneous material and its quality characteristics [14], [20], [21].

In addition to impacts, there is another type of highly nonlinear, non-analytical dependence in MTFTP mechanical systems; this is the friction zone between the tool and the machined surface. The friction forces generated in the machining zone, although much smaller than the cutting forces, have a decisive influence on oscillations in the resonant regions and on the occurrence of self-excited oscillations.

The oscillations of the MTFTP mechanical system that occur during the grinding of materials of heterogeneous structure are excited by the unevenness of the cutting forces and the friction forces. A diagram of such a studied system with two degrees of freedom is shown in Fig. 11.

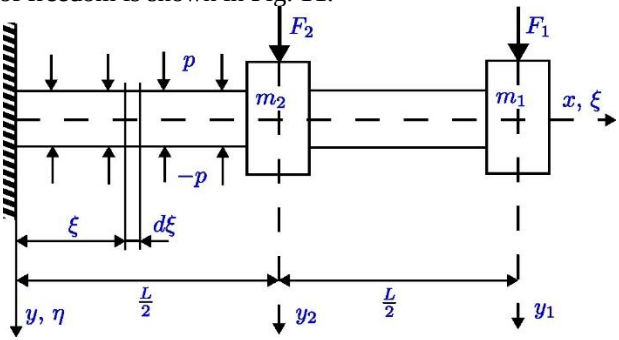

Fig. 11. Scheme of studying the MTFTP system with two degrees of freedom

When masses m_1 and m_2 move, elastic slippage occurs between two or more masses located on a beam connecting mass m_2 to the base. The analytical and numerical solution method based on the Krylov-Bogolyubov-Mitropolsky method allowed us to calculate the amplitude-frequency and phase-frequency characteristics of the steady-state vibrations. The equivalent attenuation and stiffness coefficients of this connection were determined for different elements of the MTFTP, the resonance characteristics under harmonic excitation were calculated, and the limiting values of forces for which it is impossible to constructively dampen vibrations at resonance. In this case, the amplitudes of oscillations grow unlimitedly, leading to the so-called resonant instability.

The example shown in Fig. 12 demonstrates the resonance amplitude curves of a system with hysteresis damping. Fig. 13 shows an example of optimizing the damping properties of a MTFTP system. With the correct choice of the friction coefficient, expressed by the parameter δ_0, which is achieved by using certain

lubricating cooling process media, the minimum height of the resonant peak can be achieved.

5. Research results

Theoretical results were verified by modeling in the Simulink system of the MATLAB package. The coincidence of theory and experiments confirmed the validity of the applied method.

The analytical solution using the statistical linearization method is supplemented and verified by calculations in MATLAB. The system of equations under study has the following form [11], [22]:

$$\ddot{y}_2 + \delta_\gamma(\dot{y}_2 - \dot{y}_1) + \gamma^2[(y_2 - y_1) + sy_0^2(y_2 - y_1)^3] = 0 \quad (9)$$

$$\ddot{y}_1 + y_1 + v\ddot{y}_2 = x(t) \quad (10)$$

where $x(t)$ is a random process with the character of frequency-bounded white noise.

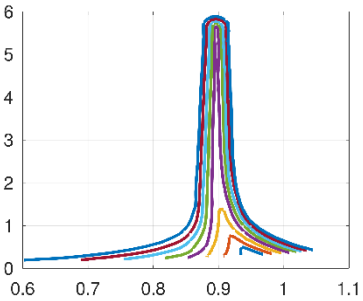

Fig. 12 Image of the amplitude resonance curves of the MTFTP system with hysteresis damping

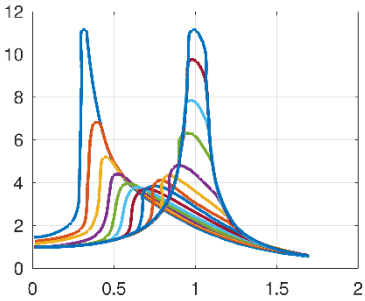

Fig. 13 Optimization of the attenuation properties of the MTFTP system due to the coefficient of friction between the tool and the machined surface

The non-linear oscillations of the systems were studied by the statistical identification method, which allowed us to determine the main characteristics of stochastically excitable systems.

When studying the properties of nonlinear systems with two degrees of freedom, attention was also drawn to the possibility of using a nonlinear vibration damper to reduce the amplitudes of a stochastically excited technological system.

It turns out that the correct choice of the nonlinearity coefficients sy_0^2, related to the technological conditions of finishing operations, can significantly reduce the oscillations of the MTFTP system. The dependence of the variance of the input signal $D[\dot{X}]$ and the output signal $D[\dot{Y}]$ at different nonlinearities sy_0^2 is shown in

Fig. 14, which can also serve as the basis for optimizing the characteristics of the nonlinear damper of stochastic oscillations of the mechanical system of the MTFTP.

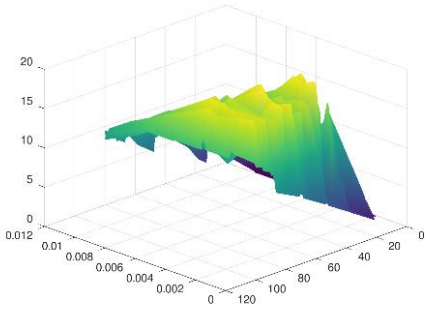

Fig. 14 Dependence of the variance of the input signal $D[\dot{X}]$ and the output signal $D[\dot{Y}]$ for different nonlinearity of sy_0^2 caused by technological parameters

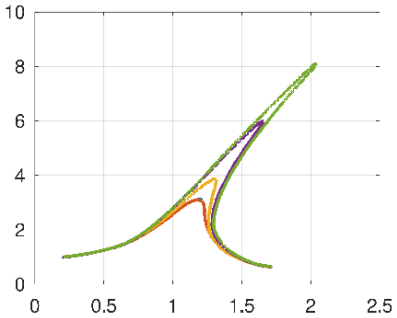

Fig. 15 Shapes of the amplitude and phase resonance curve for a system with one degree of freedom

It should be noted that the field of synthesis and identification of nonlinear systems, i.e., the compilation of the structure of a computational model, the determination of its parameters, or the characteristics of nonlinear terms based on the analysis of the motion of the mechanical system of the MTFTP, is a complex problem.

These studies have shown that it is not enough to calculate only the amplitude spectrum, but it is also necessary to determine the phase shift between the individual components of the oscillation.

Mathematical modeling of nonlinear oscillatory processes has shown that the use of identification methods for nonlinear systems is of a qualitative nature, which uses knowledge of the shape of some responses of nonlinear systems. For this reason, spectral analysis of the shape of the machined surface at the finishing stage is quite effective.

In [23], the main properties of the resonance curves expressed by the dependence of the real ($\mathrm{u} = \mathrm{a}\cos\psi$) and imaginary ($v = a\sin\psi$) parts of the response of a nonlinear dynamic system are shown. For a system with one degree of freedom, in which the shapes of the amplitude and phase resonance curves are well known (Fig. 15), the same resonance curves in the variables u and v have a special character (Fig. 16).

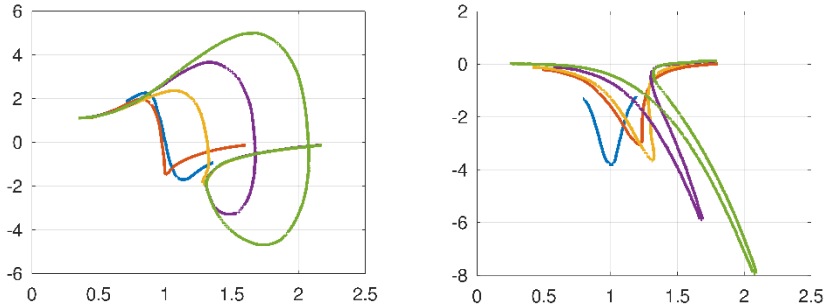

Fig. 16 Resonance curves in the variables u and v

As the attenuation decreases, the resonant peak of the real part increases but gradually tilts. The resonance curve for two degrees of freedom has a similar shape (Fig. 17 – real component). Unstable branches are indicated by dashed lines. The results of the measurements in the Simulink system are shown in Fig. 18.

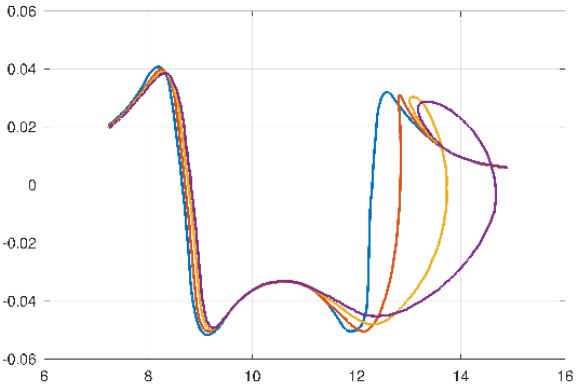

Fig. 17 Resonance curve for two degrees of freedom of the MTFTP system

The full and dashed lines indicate the resonance curves of the first and second masses in a nonlinear system with 2 degrees of freedom; the arrows indicate jumps in the resonance.

It has been shown that resonant curves during nonlinear vibrations of mechanical systems of finishing operations affect not only the formation of the roughness of the machined surface, but also the appearance of burn marks on them and the formation of defects such as cracks [11], [14], [24].

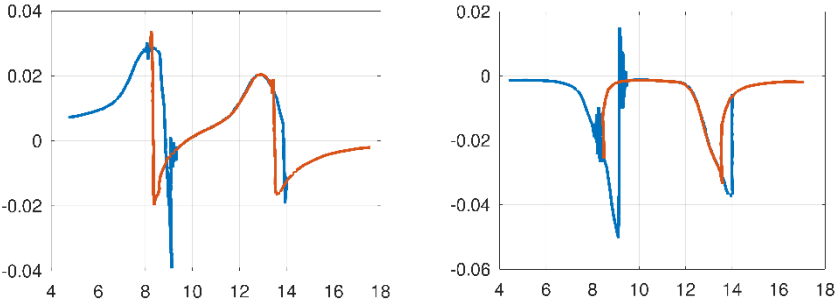

Fig. 18 Results of measuring the resonance curves in the SIMULINK system

These resonance curves are used to calculate the maximum amplitudes of forced oscillations in a given frequency domain, to determine the natural frequencies, to estimate the attenuation, and to calculate the characteristics of the nonlinear term (element) (Fig. 19).

All the conclusions that follow from the experimental study of nonlinear systems are more reliable the more accurately the oscillation parameters are measured, especially the amplitudes and phases of the fundamental or higher harmonic components.

In this case, we study, first of all, the possibilities of registering those quantities and phenomena that are typical for nonlinear oscillations.

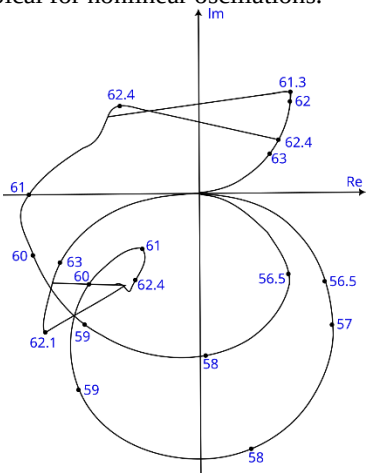

Fig. 19 Image of the resonance curves of a nonlinear system in the Kennedy-Pank diagram

Measuring instruments for oscillatory processes containing non-linear elements are practically identical to those used to measure linear systems. It is

necessary, however, to pay special attention to the accuracy of measuring the amplitude and phase resonance curves, and to the possibilities of a comprehensive analysis of the response of a nonlinear system.

An example of the measured amplitude and phase resonance curves is shown in Fig. 20. For comparison, the full results of the theoretical solution are also included. A relatively good agreement of both approaches is visible. To identify nonlinear oscillations, the method of measuring oscillations of mechanical systems and their processing using Simulink was improved [25], [26].

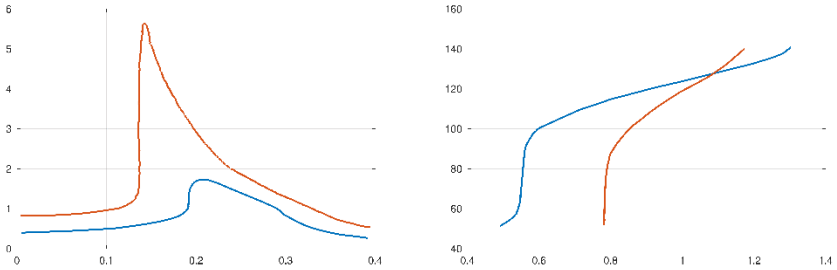

Fig. 20 (a) Theoretical and (b) experimental values of the amplitude and phase resonance curves

Since the numerical recording of measured quantities is more accurate and the numerical processing of measured indicators, for example, using Fourier analysis, is much more accurate, it can be expected that the use of the Simulink system allows for a more detailed and accurate study of the nonlinear properties of the MTFTP in finishing operations and a more accurate determination of the nonlinear characteristics of their elements.

6. Conclusions

The presented calculations and experimental studies of nonlinear oscillations in the mechanical system of finishing operations have shown their significant influence on the formation of qualitative characteristics when processing the working surfaces of parts made of materials containing inhomogeneities. This especially applies to resonance curves, which are used to calculate the maximum amplitudes of forced oscillations in a given frequency range, to establish natural frequencies, to estimate damping, and to calculate the characteristics of non-linear members of the mechanical system of the MTFTP.

References: 1. *W. Grzesik*, 'Influence of surface textures produced by finishing operations on their functional properties', Journal of Machine Engineering, vol. 16, no. 1, pp. 15–23, 2016. **2.** *W. Grzesik*, 'Influence of surface roughness on fatigue life of machine elements – the development in experimental

investigations and simulations', Mechanik, vol. 5–6, pp. 307–313, May 2019, doi: 10.17814/mechanik.2019.5-6.39. **3.** *V. Lavrinenko and V. Solod*, 'The ralationship betwheen the parameters of roughness and features of surface formation with a special microprofile', Cutting & Tools in technol. syst., vol. 96, pp. 99–109, Mar. 2022, doi: 10.20998/2078-7405.2022.96.11. **4.** *I. I. Khafizov and I. G. Nurullin*, 'Influence of roughness on operational properties of details', IOP Conf. Ser.: Mater. Sci. Eng., vol. 570, no. 1, p. 012048, Jul. 2019, doi: 10.1088/1757-899X/570/1/012048. **5.** *N. Kheir*, Systems modeling and computer simulation. Routledge, 2018. **6.** *T. N. Ivanova*, 'Design and technological methods of reducing of thermal stress in grinding process', MATEC Web Conf., vol. 224, p. 01006, 2018, doi: 10.1051/matecconf/201822401006. **7.** *A. Bezpalova, V. Lebedev, N. Klimenko, T. Chumachenko, and I. Uryadnikova*, 'Investigation and analysis of the possibility of diffusionless phase transformations in the surface layer of a part under the action of grinding temperatures', EEJET, vol. 4, no. 12 (94), pp. 36–42, Aug. 2018, doi: 10.15587/1729-4061.2018.140982. **8.** *T. N. Ivanova*, 'Research of working capacity of grinding wheels', MATEC Web Conf., vol. 224, p. 01005, 2018, doi: 10.1051/matecconf/201822401005. **9.** *O. Yakimov, L. Bovnegra, S. Uminsky, V. Tonkonogyi, and Y. Shichireva*, 'Wear grinding wheels with precise working surface', Cutting & Tools in technol. syst., vol. 92, pp. 197–207, Jul. 2020, doi: 10.20998/2078-7405.2020.92.21. **10.** *V. Gusev*, 'Surface microgeometry treated with a precast textured grinding wheel', MATEC Web Conf., vol. 329, p. 03019, 2020, doi: 10.1051/matecconf/202032903019. **11.** *E. B. Belov, S. L. Leonov, and A. A. Sitnikov*, 'Forecasting of Machined Surface Waviness on the Basis of Self-Oscillations Analysis', AMM, vol. 788, pp. 35–40, Aug. 2015, doi: 10.4028/www.scientific.net/AMM.788.35. **12.** *R. Strelchuk*, 'Surface roughness modeling during electric discharge grinding with variable polarity of electrodes', Cutting & Tools in technol. syst., vol. 94, pp. 77–84, Jun. 2021, doi: 10.20998/2078-7405.2021.94.09. **13.** *Y. Menshikov*, 'Criteria for Adequacy Estimation of Mathematical Descriptions of Physical Processes', in Computational Models in Engineering, K. Volkov, Ed., IntechOpen, 2020. doi: 10.5772/intechopen.82725. **14.** *V. I. Gurei*, 'Modeling the amplitude-frequency characteristic of the friction hardening process of flat surfaces of machine parts', Bulletin of the National Technical University "KhPI". Series: Dynamics and Strength of Machines, vol. 2, pp. 30–35, Apr. 2020, doi: 10.20998/2078-9130.2020.1.219636 (in Ukrainian). **15.** *G. A. Oborsky, A. F. Dashchenko, A. V. Usov, and D. V. Dmytryshyn*, Modeling of systems: monograph. Odesa: Astroprint, 2013 (in Russian). **16.** *A. V. Usov, O. M. Dubrov, and D. V. Dmytryshyn*, Modeling of Systems with Distributed Parameters: Monograph. Odesa: Astroprint, 2002 (in Ukrainian). **17.** *T. Liu, Z. Deng, L. Lv, S. She, W. Liu, and C. Luo*, 'Experimental Analysis of Process Parameter Effects on Vibrations in the High-Speed Grinding of a Camshaft', SV-JME, vol. 66, no. 3, pp. 175–183, Mar. 2020, doi: 10.5545/sv-jme.2019.6294. **18.** *C.-C. Wang, X.-X. Zhuo, and Y.-Q. Zhu*, 'Optimization Analysis of Vibration for Grinder Spindle', Sensors and Materials, vol. 32, no. 1, p. 407, Jan. 2020, doi: 10.18494/SAM.2020.2603. **19.** *S. Dyadya, O. Kozlova, E. Kushnir, and D. Karamushka*, 'Research of oscillations during end-milling and their influence on the formation of the machined surface', HMT, vol. 2, pp. 71–77, Jan. 2023, doi: 10.15588/1607-6885-2022-2-12. **20.** *T. I. Zohdi*, 'Modeling and simulation of the post-impact trajectories of particles in oblique precision shot-peening', Comp. Part. Mech., vol. 3, no. 4, pp. 533–540, Nov. 2016, doi: 10.1007/s40571-015-0048-5. **21.** *M. Rifat, E. C. DeMeter, and S. Basu*, 'Microstructure evolution during indentation of Inconel-718 created by additive manufacturing', Materials Science and Engineering: A, vol. 781, p. 139204, Apr. 2020, doi: 10.1016/j.msea.2020.139204. **22.** *V. Fedorovich, I. Pyzhov, and I. Voloshkina*, 'Modeling of the process of vibratory grinding by finite element method', Cutting & Tools in technol. syst., vol. 90, pp. 136–150, May 2019, doi: 10.20998/2078-7405.2019.90.14. **23.** *B. Ma and Y. Ren*, 'Nonlinear Dynamic Analysis of the Cutting Process of a Nonextensible Composite Boring Bar', Shock and Vibration, vol. 2020, pp. 1–13, Oct. 2020, doi: 10.1155/2020/5971540. **24.** *F. Novikov*, 'Optimisation of interrupted grinding parameters according to the temperature criterion', Cutting & Tools in technol. syst., vol. 98, pp. 59–72, May 2023, doi: 10.20998/2078-7405.2023.98.06. **25.** *P. Sivák, I. Delyová, J. Bocko, and J. Šarloši*, 'Some methods of analysis of chaos in mechanical systems', AJME, vol. 2, no. 7, pp. 199–203, Nov. 2014, doi: 10.12691/ajme-2-7-6. **26.** *V. Nekhaev, V. Nikolaev, and M. Safronova*, 'Numerical simulation of oscillations of a nonlinear mechanical system with

a spring-loaded viscous friction damper', MATEC Web Conf., vol. 265, p. 05030, 2019, doi: 10.1051/matecconf/201926505030.

Анатолій Усов, Максим Куніцин, Одеса, Україна

МОДЕЛЮВАННЯ ВПЛИВУ НЕЛІНІЙНИХ КОЛИВАНЬ НА ЯКІСТЬ РОБОЧОЇ ПОВЕРХНІ ДЕТАЛЕЙ НА ФІНІШНИХ ОПЕРАЦІЯХ

Анотація. *Досліджується вплив фінішних операцій на шорсткість оброблюваних поверхонь у випадку, коли система «Верстат-Пристосування-Інструмент-Деталь» (ВПІД) знаходиться в зоні нелінійних коливань. Для досягнення поставленої мети будуються математичні моделі динамічних коливальних процесів, що супроводжують обробку робочих поверхонь деталей, із використанням середовища Simulink пакету MATLAB. Проведене моделювання дозволяє визначити умови формування самозбуджених коливань механічної системи ВПІД під час фінішних операцій, як у випадку однієї, так і двох ступенів свободи, що виникають внаслідок неоднорідності оброблюваного матеріалу, зовнішніх збурюючих сил та їхнього впливу в діапазонах основних і субгармонічних резонансів. Враховано також наявність зон сухого тертя між інструментом і оброблюваною поверхнею, що істотно впливає на характер коливань. Наведені в роботі дослідження демонструють не тільки поведінку механічних систем, здатних до виникнення автоколивань, але й дають змогу успішно застосовувати результати моделювання для оптимізації якісних характеристик оброблюваних поверхонь на етапі фінішних операцій. Особлива увага приділена аналізу резонансних кривих, які при наявності нелінійних коливань у механічних системах фінішної обробки впливають не лише на формування шорсткості обробленої поверхні, але й сприяють виникненню дефектів, таких як припіки, мікротріщини та інші пошкодження поверхневого шару матеріалу. Результати моделювання показали, що характер автоколивань і резонансних явищ істотно залежить від параметрів з'єднань, властивостей оброблюваного матеріалу, а також від умов зовнішнього навантаження. Це дозволяє запропонувати методи регулювання процесу обробки через зміну технологічних режимів, зокрема використання демпфувальних елементів або контрольованого сухого тертя для зменшення амплітуд небажаних коливань. Отримані дані можуть бути використані для вдосконалення конструкції елементів технологічного оснащення, підвищення точності обробки та поліпшення експлуатаційних характеристик деталей машин.*

Ключові слова*: фінішні операції; нелінійні коливання; моделі; система SIMULINK; амплітуди коливань; стійкість.*

UDC 621.9.048.7 **doi: 10.20998/2078-7405.2025.102.03**

ANALYSIS OF PARAMETERS OF LASER-INDUCED PERIODIC MICROSTRUCTURES (LIPSS) ON THE SURFACE OF STAINLESS STEEL USING AUTOCORRELATION FUNCTIONS

Emiliia **Saprykina**[1,2][0009-0004-4780-6316], Sergey **Dobrotvorskiy**[1,3][0000-0003-1223-1036], Borys **Aleksenko**[1][0000-0001-9680-9370], Dmytro **Trubín**[1][0009-0000-7953-6139], Denys **Moskal**[2][0000-0003-3919-8651], Jiri **Martan**[2][0000-0002-5832-4425].

[1]National Technical University «Kharkiv Polytechnic Institute», Kharkiv, Ukraine
[2]University of West Bohemia, Plzen, Czech Republic
[3]Poznan University of Life Sciences, Poznan, Poland
jmartan@ntc.zcu.cz

Received: 29 April 2025 / Revised: 19 May 2025 / Accepted: 29 May 2025 / Published: 20 June 2025

Abstract. *In modern mechanical engineering, the control of surface quality of components, which directly affects their operational characteristics, is becoming increasingly important. One of the key aspects is the analysis of surface microstructure, particularly its periodicity, as it determines properties such as wear resistance and corrosion resistance. Laser processing is one of the promising technologies that allows the formation of regular microstructures, such as LIPSS (Laser-Induced Periodic Surface Structures). Despite extensive research, the mechanism of LIPSS formation remains not fully understood, and the results often show variable periodicity and orientation. To accurately analyze these structures, mathematical and statistical methods, such as two-dimensional autocorrelation analysis (ACF) and fast Fourier transform (FFT), are required. This study proposes a methodology for evaluating the periodicity of microstructures obtained during laser treatment of metallic samples, using digital video microscopy. The application of two-dimensional autocorrelation and spectral analysis within the Gwyddion environment ensures reproducible and objective assessment of microstructures, while demonstrating the effectiveness of ACF for surface topography analysis. The obtained data show the presence of pronounced periodicity in the studied microstructure and confirm the complexity of the LIPSS formation mechanisms, contributing to accurate quantitative analysis and adaptive control of laser modification processes.*
Keywords: *laser processing; LIPSS; autocorrelation analysis; microstructure.*

1. Introduction

Modern mechanical engineering imposes increasingly high demands on the quality of component surfaces, which directly affect their reliability, durability, and operational characteristics [1, 2]. Special attention is paid to the microstructure of

the surface layer, as it determines parameters such as wear resistance, corrosion resistance, and fatigue load resistance.

One of the key aspects of microstructure analysis is the identification and quantitative assessment of its periodicity [3, 4]. Periodic structures can arise from various technological processes, such as surface plastic deformation, electroerosion processing, magnetic-abrasive processing, and laser treatment. Understanding the patterns of formation of these structures allows optimizing technological modes and improving the operational properties of products.

Surface engineering in the context of modern high-tech production is becoming increasingly important, especially in terms of precise control of material microstructure. In industries such as aerospace [5], automotive [6,7], microelectronics [8, 9] and biomedicine [10], key characteristics include not only the chemical composition and macroform of products, but also the properties of the surface layer [11], including its microtopography and texture.

One of the most promising surface modification technologies in recent years is laser processing. Thanks to its high precision, localized impact, and the ability to finely control radiation parameters, laser methods can form regular microstructures and nanostructures, such as LIPSS (Laser-Induced Periodic Surface Structures). These structures are wave-like reliefs with characteristic periods of the order of the wavelength of the radiation and smaller, arising from the interference of the incident laser beam with excited surface plasmonic fields.

However, despite extensive research, the process of LIPSS formation [12] is not fully understood, and often the result is random, with varying periodicity and orientation. As Bonse and Gräf [13] note, even slight changes in irradiation parameters—polarization, angle of incidence, pulse duration—can drastically change the resulting morphology. This creates the need to develop precise methods for quantitative analysis of the periodicity and regularity of the structures formed [14, 15].

Classical metrological methods, such as roughness measurements (R_a, R_z), are unable to adequately describe the periodic nature of LIPSS [16, 17]. To address this, mathematical-statistical approaches are increasingly being applied—such as two-dimensional autocorrelation analysis and fast Fourier transform (FFT)—to identify the dominant frequencies and directions of the relief [18 – 20]. Such methods not only provide numerical assessments but also serve as tools for visualizing periodicity, which is suitable for automated quality control.

In particular, as research by Abdelmalek et al. [21] and Magonov et al. [22] showed, the combination of Fourier analysis with high-resolution scanning microscopy (SEM, AFM) provides reliable results when controlling laser-modified surfaces. The use of available software packages, such as Gwyddion, ImageJ, and

MATLAB, allows reproducible image processing and the acquisition of objective characteristics [23].

The aim of this research is to develop and demonstrate a methodology for assessing the periodicity of microstructures obtained by laser surface treatment of metallic samples. For this, two-dimensional autocorrelation and spectral analysis of images obtained by scanning microscopy are applied, followed by processing in the Gwyddion environment. The work aims to enhance the reproducibility of the assessment and lay the groundwork for adaptive control of laser surface modification processes.

2. Applied methods

Metallic samples (material grade: AISI 304) were used in this study, having undergone laser processing to form regular microstructures. The treatment was carried out using a femtosecond laser with a wavelength of 1030 nm, a pulse duration of 300 fs, and a repetition rate of 100 kHz. The pulse energy and scanning speed were varied within a range that ensured the stable formation of LIPSS (Laser-Induced Periodic Surface Structures).

After laser processing, the samples were cleaned in an ultrasonic bath with ethanol and dried at room temperature. No additional mechanical or chemical post-treatment was applied to the surfaces in order to preserve the structure formed exclusively by laser exposure.

Method of image acquisition.

Surface morphology was investigated using a digital video microscope (HIROX KH-7700), which provides optical magnification ranging from 0.1× to 7000× and a camera resolution of 1600×1200 pixels (UXGA). These specifications ensure adequate spatial resolution for identifying surface microstructural features resulting from variations in laser processing parameters. The acquired high-resolution images, saved in TIFF and JPG formats, were subsequently utilized for numerical analysis.

Method of periodicity analysis.

Image analysis was performed using the open-source software package Gwyddion — a freely available tool for processing scanning probe microscopy data, offering functions for autocorrelation analysis, spectral transformations, filtering, and visualization.

The primary analytical method employed in this study was the two-dimensional autocorrelation function (ACF), which enables the identification of characteristic distances between repeating microstructural features, regardless of their shape or orientation. The use of ACF provides not only a quantitative assessment of periodicity but also a visual insight into the structural regularity, symmetry, and the presence of local defects.

For each image, the ACF was computed, and the dominant spatial frequency was determined from the central cross-section. The periodicity was calculated based on the position of the first maximum of the autocorrelation function. Additionally, the fast Fourier transform (FFT) was applied to confirm the results obtained via the autocorrelation method and to evaluate the orientation of structural elements.

Visualization and data processing.

The resulting autocorrelation maps and Fourier spectra were visualized using Gwyddion's built-in tools [24], which provide accurate scale referencing and convenient image navigation. Additional statistical analysis — including the calculation of the standard deviation of periods, regularity assessment, and histogram plotting — was performed in the Python environment using the NumPy, SciPy, and Matplotlib libraries.

This approach ensured a reproducible and objective evaluation of the microstructures formed during laser treatment, and demonstrated the effectiveness of combining ACF and FFT for surface topography analysis.

3. Results and discussion

The samples of structures on the surface of AISI 304 steel obtained after laser processing (Fig. 1) demonstrate the presence of periodicity in the form of regularly spaced features aligned along specific directions, characteristic of laser-induced periodic surface structures (LIPSS).

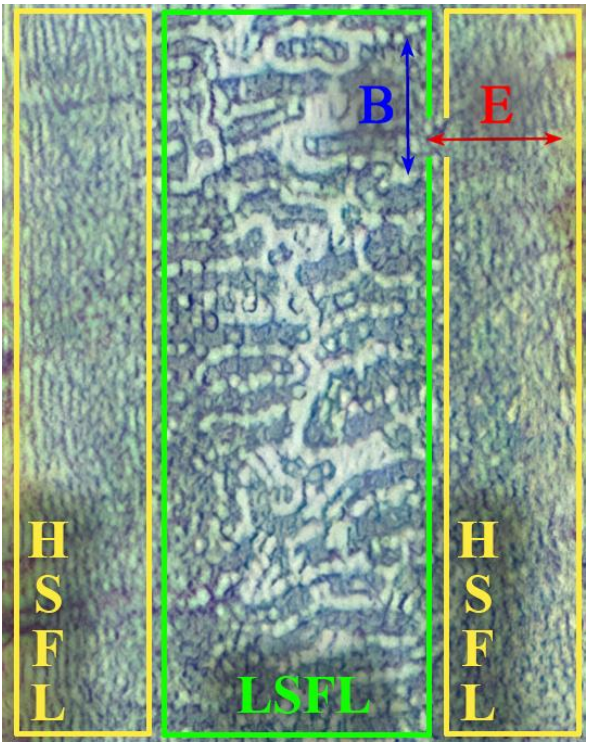

Fig. 1. Surface microstructure formed on the surface of AISI 304 steel.

The microscopy results clearly demonstrate the presence of low-spatial-frequency laser-induced periodic surface structures (LSFL) and high-spatial-frequency LIPSS (HSFL) on the sample surface (Fig. 1), as described in [25].

Autocorrelation analysis was carried out using the Gwyddion software, with preliminary selection of regions exhibiting structures of different spatial frequencies. To measure the isotropy of a surface, the autocorrelation function (1) is used:

$$R(\tau) = \int_{-\infty}^{\infty} f(x) \cdot f(x+\tau) dx, \quad (1)$$

$R(\tau)$ — autocorrelation function, $f(x)$ — the function for which the autocorrelation is calculated, τ — shift (the parameter by which the function is shifted during the calculation process).

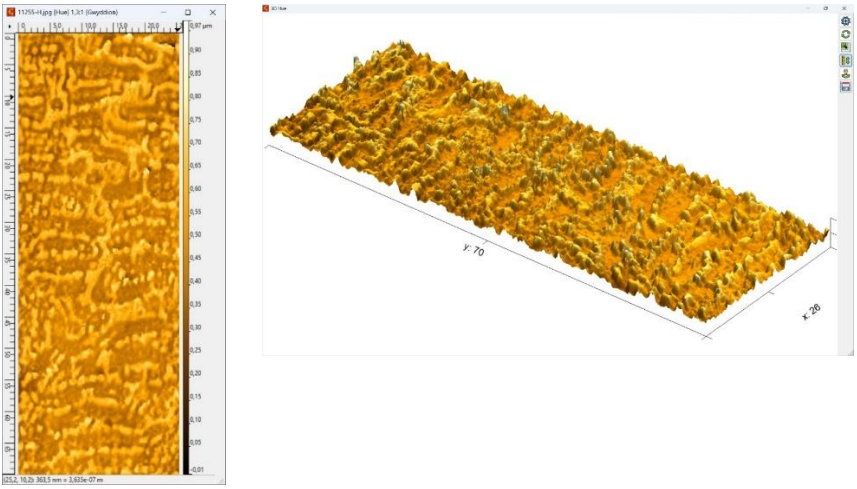

A B

Fig. 2. Analysis of the surface microstructure section with LSFL in the Gwyddion software package. A – 2D plot; B – Surface plot.

Autocorrelation analysis performed in the Gwyddion environment revealed characteristic spatial periods at the level of 3.536 μm, confirmed by regular maxima of the autocorrelation function. The measured peak parameters (height, area, width) indicate a high degree of microstructure regularity.

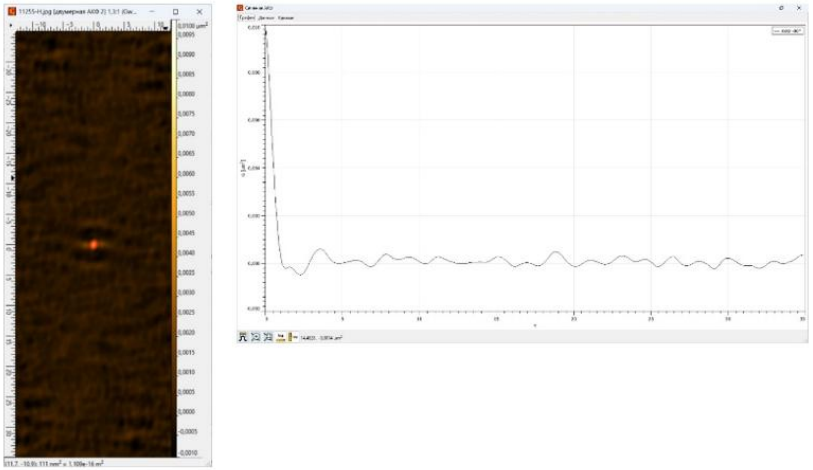

A B

Fig. 3. Cross-section of the autocorrelation function (ACF) (-90°) of the area with a low-frequency spatial LIPSS structure. A – 2D plot; B – Graph.

The analysis of the surface microstructure area with HSFL was carried out in a similar manner.

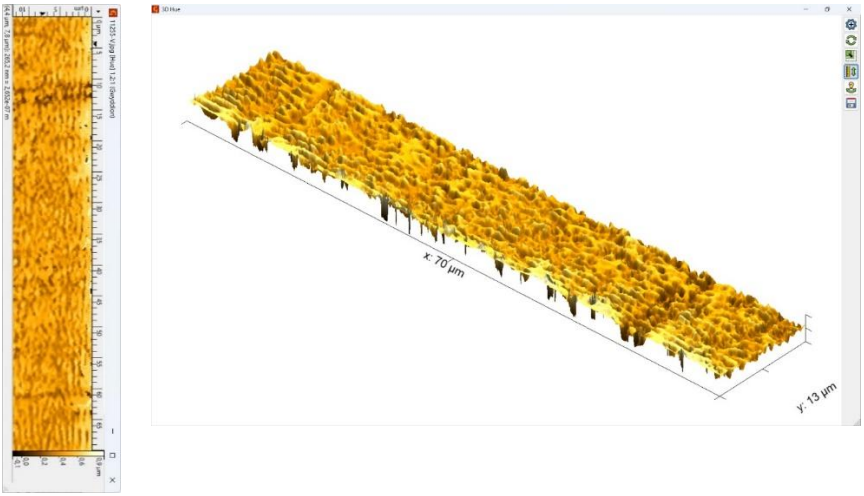

A B

Fig. 4. Analysis of the surface microstructure section with HSFL in the Gwyddion software package. A – 2D plot; B – Surface plot.

Autocorrelation analysis of the region with high-spatial-frequency LIPSS (HSFL) revealed characteristic spatial periods at the level of 1.0186 µm, confirmed by regular maxima in the autocorrelation function. The measured peak parameters (height, area, width) also indicate a high degree of microstructure regularity.

For a more in-depth analysis of the regularity of the spatial structures, a Fast Fourier Transform (FFT) of the autocorrelation function (ACF) was performed. Although the identification of a principal spatial period was expected, the spectral distribution predominantly exhibited a central peak with only minor side deviations—this may be attributed to measurement noise, low structural regularity, or fluctuations in the amplitude profile.

Nevertheless, the presence of side 'shoulders' near the 1 μm^{-1} coordinate confirms the existence of a dominant spatial frequency. This indicates partial structural regularity and may reflect a characteristic scale of repeating elements.

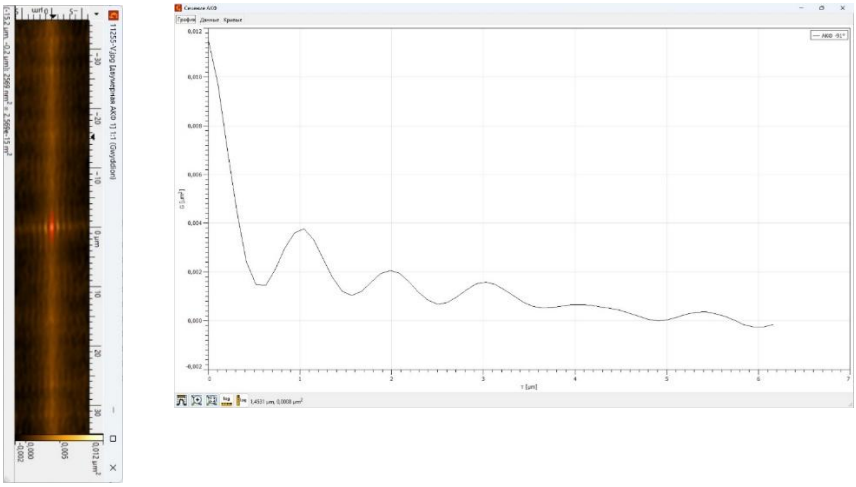

A B

Fig 5. Cross-section of the autocorrelation function (ACF) (-90°) of the area with a high-frequency spatial LIPSS structure. A – 2D plot; B – Graph.

Such a spectral pattern is typical for surfaces modified by laser irradiation in the LIPSS regime, where the formation of periodic features results from the interplay of both interference and thermal processes, often superimposed on one another.

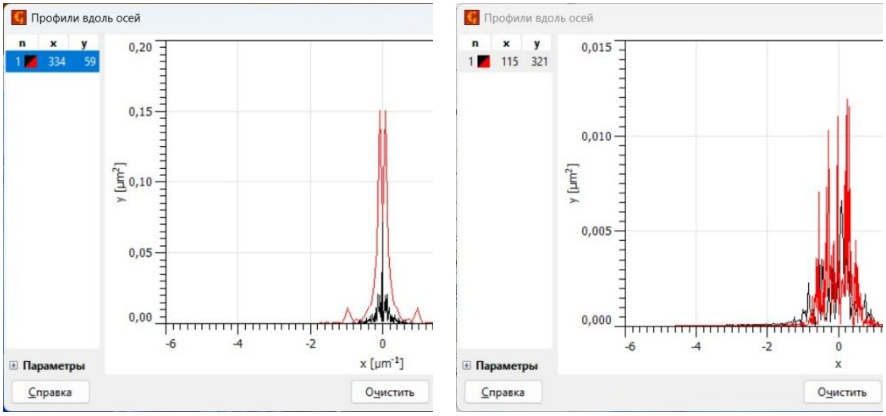

A B

Fig. 6. FFT spectra of the autocorrelation function (ACF). A – LSFL; B – HSFL.

Thus, in this case, the FFT spectrum of the ACF serves rather as a supplementary diagnostic tool to confirm the presence of periodic components, rather than a primary method of quantitative analysis. Visual inspection of the ACF and identification of the first-order maxima remains the preferred approach in terms of accuracy and interpretability of the results.

4. Conclusions

Analysis of the autocorrelation functions (ACFs) derived from microscopic images of the processed surfaces revealed a pronounced spatial periodicity. Figure 4 presents an example of an ACF along the -90° direction, generated in Gwyddion based on the original topographic data.

The first local maximum is observed at $\boldsymbol{\tau} \approx 3.54$ μm, corresponding to the characteristic period of the regular structure. Additional maxima appear at intervals of approximately 7–8 μm, indicating repeatability of the pattern within the analyzed area.

To quantitatively describe the structural regularity, local maxima on the ACF plot were marked (see Fig. 5). The coordinates of the first five maxima are listed in Table 1.

№	**τ**, μm	**h**	**A**	**w**
1	3,54	835,7	998,2	0,425
2	11,21	289,6	307,8	0,427
3	18,80	608,6	689,9	0,429
4	26,40	396,7	347,1	0,323
5	29,99	442,9	592,1	0,613

Table 1. Coordinates of the ACF maxima and repeatability parameters of the surface icrostructure section with LSFL.

Despite partial irregularity in the amplitude characteristics (**h**, **A**), where the heights (**h**) and areas (**A**) of the ACF peaks provide an estimate of the structural contrast and repeatability, the spatial positioning of the maxima exhibits satisfactory equidistance, confirming the presence of a stable periodic structure. The variation in τ values between adjacent maxima does not exceed 0.6–0.8 μm.

In addition to the primary periodic structure with a characteristic pitch of approximately 3.5 μm, high-frequency formations oriented perpendicularly to the primary ones were detected in certain surface areas (Fig. 1). These features are

identifiable both in the topographic data and in the corresponding ACF cross-sections.

Figure 6 shows the annotation of additional maxima corresponding to the secondary (high-frequency) pattern. Table 2 provides their numerical characteristics.

№	**τ,** μm	**h**	**A**	**w**
1	1,02	2510,9	1 198 600	177,3
2	1,99	1194,3	586 048	180,4
3	3,01	970,2	538 348	206,7
4	4,05	389,5	336 519	263,4
5	5,38	482,5	273 321	200,7

Table 2. Coordinates of the ACF maxima and repeatability parameters of the surface microstructure section with HSFL.

As can be seen from the presented data, this structure has a smaller period (on the order of 1–2 μm), a higher frequency, and a relatively higher amplitude of autocorrelation function (ACF) oscillations in the initial interval. The width of the ACF peak (parameter **w**) can be interpreted as an indicator of the variability or dispersion in the structural periodicity. This parameter (**w**) varies from 177 to 263 nm.

Such a two-level periodicity may indicate the superposition of different mechanisms of structure formation during laser processing: the primary one is of an interference nature, while the secondary one is caused by modulations of the local thermal gradient or inhomogeneities in the energy distribution of the laser beam.

The obtained data is consistent with the formation characteristics of LIPSS structures during laser processing, where periods on the order of 1–5 μm are typically formed, depending on the wavelength and irradiation parameters. Since the mechanism of LIPSS generation remains complex and includes interference, capillary, and thermoelastic components, additional quantitative processing of the ACF helps to improve the reliability of the analysis of the resulting structure.

Such spatial decomposition of periodicities within a single processed area can serve as additional confirmation of the complexity and multi-component nature of the laser impact mechanisms. The presented data allows for the identification of the parameters of both structures with high accuracy, with the autocorrelation function serving as the primary tool for quantitative analysis, ensuring the objective identification of periods without prior assumptions about the shape or direction of the modules.

Acknowledgements

This article has been supported by the projects: SGS-2025-025: Research and development for innovation in Machining, additive technology and quality assurance; and "Formation and transformation of periodic nanocarbon-containing structures on metal surfaces with short-pulse laser, microwave, and plasma methods" SR. no. 0124U000481.

References: 1. *Abellán-Nebot, J.V., Vila Pastor, C. and Siller, H.R.* A Review of the Factors Influencing Surface Roughness in Machining and Their Impact on Sustainability. Sustainability, [online] 16(5), 2024, p.1917. https://doi.org/10.3390/su16051917. **2**. *Xu, J., Yu, H., Xiao, R., Liu, Q. and Chen, S.* Features detection of Al alloy porosity during GTAW process based on arc spectrum and improved porosity-focus decision tree. Journal of Manufacturing Processes, [online] 88, 2023, pp.71–83. https://doi.org/10.1016/j.jmapro.2023.01.015. **3**. *Sidor, J.J.* Quantitative Indicators of Microstructure and Texture Heterogeneity in Polycrystalline System. Materials, [online] 17(24), 2024, pp.6057–6057. https://doi.org/10.3390/ma17246057. **4**. *Grajcar, A., Aleksandra Kozłowska, Krzysztof Radwański and Skowronek, A.* Quantitative Analysis of Microstructure Evolution in Hot-Rolled Multiphase Steel Subjected to Interrupted Tensile Test. Metals, [online] 9(12), 2019, pp.1304–1304. https://doi.org/10.3390/met9121304. **5**. *Jin, Z.-Z., Zha, M., Wang, H.-Y., Ma, J.-G. and Liu, Y.-C.* Achieving remarkable enhancement of yield strength and high ductility in a fine-grained Mg-6Zn-0.2Ca alloy via rotated hard-plate rolling. Materials & Design, 234, 2023, p.112345. https://doi.org/10.1016/j.matdes.2023.112345. **6**. *Senuma, T., Okayasu, M. and Mohrbacher, H.* Microstructural Control and Alloy Design for Improving the Resistance to Delayed Fracture of Ultrahigh-Strength Automotive Steel Sheets. Metals, [online] 13(8), 2023, p.1368. https://doi.org/10.3390/met13081368. **7**. *Mojtaba Karamimoghadam, Rezayat, M., Moradi, M., Mateo, A. and Casalino, G.* Laser Surface Transformation Hardening for Automotive Metals: Recent Progress. Metals, 14(3), 2024, pp.339–339. https://doi.org/10.3390/met14030339. **8**. *Tien, T.-C., Hsieh, T.-E., Lee, Y.-S., Wang, Y.-H. and Lee, M.-L.* Electrical and Hysteresis Characteristics of Top-Gate InGaZnO Thin-Film Transistors with Oxygen Plasma Treatment Prior to TEOS Oxide Gate Dielectrics. Coatings, 12(3), 2022, pp.383–383. https://doi.org/10.3390/coatings12030383. **9**. *Sun, Y., Gao, B., Hu, L., Li, K. and Zhang, Y.* Effect of CeO2 on Corrosion Resistance of High-Current Pulsed Electron Beam Treated Pressureless Sintering Al-20SiC Composites. Coatings, 11(6), 2021, pp.707–707. https://doi.org/10.3390/coatings11060707. **10**. *Müller, F., Kunz, C. and Gräf, S.* Bio-Inspired Functional Surfaces Based on Laser-Induced Periodic Surface Structures. Materials, 9(6), 2016, p.476. https://doi.org/10.3390/ma9060476. **11**. *Li, X., Su, H., Li, H., Tan, X., Lin, X., Wu, Y., Xiong, X., Li, Z., Jiang, L., Xiao, T., Chen, W. and Tan, X.* Photothermal superhydrophobic surface with good corrosion resistance, anti-/de-icing property and mechanical robustness fabricated via multiple-pulse laser ablation. Applied surface science, 646, 2024, pp.158944–158944. https://doi.org/10.1016/j.apsusc.2023.158944. **12**. *Bonse, J.* Quo Vadis LIPSS?—Recent and Future Trends on Laser-Induced Periodic Surface Structures. Nanomaterials, 10(10), 2020, 1950. https://doi.org/10.3390/nano10101950. **13**. *Bonse, J., & Gräf, S.* Ten Open Questions about Laser-Induced Periodic Surface Structures. Nanomaterials, 11(12), 2021, 3326. https://doi.org/10.3390/nano11123326. **14**. *Belousov, D.A., Bronnikov, K.A., Okotrub, K.A., Mikerin, S.L., Korolkov, V.P., Terentyev, V.S. and Dostovalov, A.V.* Thermochemical Laser-Induced Periodic Surface Structures Formation by Femtosecond Laser on Hf Thin Films in Air and Vacuum. Materials, 14(21), 2021, p.6714. https://doi.org/10.3390/ma14216714. **15**. *Lübcke, A., Zsuzsanna Pápa and Matthias Schnürer* Monitoring of Evolving Laser Induced Periodic Surface Structures. Applied Sciences, 9(17), 2019, pp.3636–3636. https://doi.org/10.3390/app9173636. **16**. *Goodhand, M.N., Walton, K., Blunt, L., Lung, H.W., Miller, R.J. and Marsden, R.* The Limitations of 'Ra' to Describe Surface

Roughness. 2015. https://doi.org/10.1115/gt2015-43329. **17**. *Wonneberger, R., Gräf, S., Bonse, J., Wisniewski, W., Freiberg, K., Hafermann, M., Ronning, C., Müller, F. A., & Undisz, A.* Tracing the Formation of Femtosecond Laser-Induced Periodic Surface Structures (LIPSS) by Implanted Markers. ACS Applied Materials & Interfaces, 17(1), 2024, 2462–2468. https://doi.org/10.1021/acsami.4c14777. **18**. *Podulka, P.* Resolving Selected Problems in Surface Topography Analysis by Application of the Autocorrelation Function. Coatings, 13(1), 2022, p.74. https://doi.org/10.3390/coatings13010074. **19**. *Podulka, P.* Selection of Methods of Surface Texture Characterisation for Reduction of the Frequency-Based Errors in the Measurement and Data Analysis Processes. Sensors, 22(3), 2022, p.791. https://doi.org/10.3390/s22030791. **20**. *Peng, Z. and Kirk, T.B.* Two-dimensional fast Fourier transform and power spectrum for wear particle analysis. Tribology International, 30(8), 1997, pp.583–590. https://doi.org/10.1016/s0301-679x(97)00026-1. **21**. *Abdelmalek, A., Giakoumaki, A.N., Bharadwaj, V., Sotillo, B., Phu, T.L., Bollani, M., Zeyneb Bedrane, Ramponi, R., Eaton, S.M. and Maaza, M.* Morphological Study of Nanostructures Induced by Direct Femtosecond Laser Ablation on Diamond. Micromachines, 12(5), 2021, pp.583–583. https://doi.org/10.3390/mi12050583. **22**. *Magonov, S., Alexander, J. and Belikov, S.* Exploring Surfaces of Materials with Atomic Force Microscopy. Nanostructure Science and Technology, 2012, pp.203–253. https://doi.org/10.1007/978-1-4614-5016-0_7. **23**. *D Nečas, P Klapetek and M Valtr.* Estimation of roughness measurement bias originating from background subtraction. Measurement Science and Technology, 31(9), 2020, pp.094010–094010. https://doi.org/10.1088/1361-6501/ab8993. **24**. Gwyddion.net. (2021). *Gwyddion – Features*. [online] Available at: https://gwyddion.net/features.php [Accessed 8 May 2025. **25**. *Bonse, J. and Gräf, S.* Maxwell Meets Marangoni—A Review of Theories on Laser-Induced Periodic Surface Structures. *Laser & Photonics Reviews*, 14(10), 2020, p.2000215. https://doi.org/10.1002/lpor.202000215.

Емілія Саприкіна, Сергій Добротворський, Борис Алексенко, Дмитро Трубін, Харків, Україна, Денис Москаль, Іржі Мартан, Плзень, Чехія

АНАЛІЗ ПАРАМЕТРІВ ЛАЗЕРНО-ІНДУКОВАНИХ ПЕРІОДИЧНИХ МІКРОСТРУКТУР (LIPSS) НА ПОВЕРХНІ НЕРЖАВІЮЧОЇ СТАЛІ З ВИКОРИСТАННЯМ АВТОКОРЕЛЯЦІЙНИХ ФУНКЦІЙ

Анотація. *У сучасному машинобудуванні дедалі більшого значення набуває контроль якості поверхні компонентів, що безпосередньо впливає на їхні експлуатаційні характеристики. Одним з ключових аспектів контролю якості є аналіз мікроструктури поверхні, зокрема такої її трибологічної характеристики як періодичність, оскільки це визначає такі властивості, як зносостійкість, оптичні властивості та корозійна стійкість. Лазерна обробка є однією з перспективних технологій, що дозволяє формувати регулярні мікроструктури, такі як LIPSS (лазерно-індуковані періодичні поверхневі структури). Незважаючи на чисельні дослідження, механізм утворення LIPSS залишається вивченим не до кінця, і результати часто демонструють змінну періодичність та орієнтацію отриманих в процесі дослідження мікроструктур. Для точного аналізу цих структур необхідні математичні та статистичні методи, такі як двовимірний автокореляційний аналіз (ACF) та швидке перетворення Фур'є (FFT). У представленому дослідженні пропонується методологія оцінки періодичності мікроструктур, які були отримано під час лазерної обробки металевих зразків. Структури було вивчено за допомогою цифрової відеомікроскопії, після чого був проведений аналіз отриманих зображень поверхні з використанням програмного середовища Gwyddion. Застосування двовимірної автокореляції та спектрального аналізу в середовищі Gwyddion забезпечує відтворювану та об'єктивну оцінку мікроструктур, одночасно демонструючи ефективність ACF для аналізу*

топографії поверхні. Для більш глибокого аналізу регулярності просторових структур було виконано швидке перетворення Фур'є (ШПФ) отриманої автокореляційної функції (АКФ). Спостереження наявності незначних додаткових бічних піків на графіку (ШПФ) поблизу координати головного піку підтверджує існування домінуючої просторової частоти. Це вказує на часткову структурну регулярність і може відображати характерний масштаб повторюваних елементів. Отримані за допомогою автокореляційного аналізу (ACF) дані показують наявність вираженої періодичності в досліджуваній мікроструктурі, одночасно підтверджуючи складність механізмів формування LIPSS, сприятимуть точному кількісному аналізу та адаптивному керуванню процесами лазерної модифікації.
Ключові слова: *лазерна обробка; LIPSS; автокореляційний аналіз; мікроструктура.*

UDC 621.9.02 **doi: 10.20998/2078-7405.2025.102.04**

COMPUTATIONAL AND ANALYTICAL MODELS OF THE MAJOR TYPES OF CUTTING TOOL FAILURE

Galyna **Klymenko** [0000-0002-1022-6324], Viktor **Kovalov** [0000-0001-5091-5856], Yana **Vasylchenko** [0000-0002-4566-8827], Maksym **Shapovalov** [0000-0002-8039-8834], Dmytro **Grygorenko** [0009-0002-3382-2644]

Donbass State Engineering Academy (DSEA), Kramatorsk, Ukraine
wasilchenko.ua@gmail.com

Received: 10 May 2025 / Revised:19 May 2025 / Accepted: 29 May 2025 / Published: 20 June 2025

Abstract. *The paper presents analytical and numerical models for assessing the reliability of cutting tools used in the processing of critical parts for the defence and energy industries. The criteria of boundary wear on the back and front surfaces, possible fatigue failure and plastic deformation of the cutting edge are taken into account. Analytical dependencies have been constructed to calculate the number of parts that can be machined before tool failure, taking into account the physical and mechanical characteristics of the tool and processed materials, technological modes and thermal loading conditions. The results allow for the selection of tools and cutting parameters based on increased reliability and process optimisation. These mathematical dependencies make it possible to take into account the predominant type of cutting tool wear, which is especially important when working with large parts on heavy machine tools. The results of the study are of practical importance for industry, as they allow to increase the stability and productivity of technological processes.*
Keywords: *reliability; tool wear; fatigue; heavy engineering; cutting; adhesive wear; thermomechanical load; plastic deformation; cutting edge.*

1. Introduction

In heavy engineering, machining parts intended for use under high loads and temperatures, particularly in the defence and energy sectors, requires high precision and stability of the cutting tool. Tool reliability is one of the key parameters that determines the quality and efficiency of the technological process. The relevance of the topic is driven by the need to predict and extend the life of cutting tools by mathematically modelling the processes of wear and fracture. The aim of the study is to create reliable calculation models that allow determining the maximum number of parts that can be machined before tool failure.

2. Problem statement

The task is to build mathematical models for assessing the reliability of a cutting tool according to the criteria of limit wear, fatigue failure and plastic deformation. The input parameters are the physical and mechanical properties of the tool and

processed materials, cutting modes (speed, depth, feed), and temperature conditions in the contact zone. The output parameter is the number of parts that can be machined without losing tool life. It is necessary to take into account various wear mechanisms, as well as random fluctuations in parameters that affect the accuracy of the forecast.

3. Literature review

The study of the problem of cutting tool reliability has become widespread in the scientific literature. A considerable number of papers [1–5] are devoted to the analysis of back surface wear as the main failure mechanism. Studies [6–8] examine the processes of adhesive and abrasive wear, as well as the influence of tool microgeometry. Some works [9–11] focus on thermomechanical loading in the cutting zone and modelling of temperature fields. However, insufficient attention is paid to a comprehensive assessment taking into account fatigue fracture and plastic deformation, which significantly affects reliability in heavy cutting conditions. This study aims to extend the existing models by using computational and analytical approaches and experimental observations.

4. Materials and Methods

The calculations are based on mathematical models that take into account adhesive wear on the back and front surfaces, fatigue, and plastic buckling. The modelling takes into account steels 40KhNMA (AISI 4340), X18H9T (AISI 321) and tool materials T14K8 (HS410), P6M5 (AISI M2). The dependences of contact pressures, cutting temperature, and wear parameters obtained by statistical processing of experimental data were used. The number of machined parts before failure was estimated based on the criteria of ultimate wear of the height, depth of the hole, ultimate plastic deformation, and fatigue failure.

The number of parts that can be machined before the maximum allowable height of the wear area on the rear surface is formed

$$N_{0.1} = \begin{cases} [h_{зn}] \cdot \sqrt{\dfrac{3{,}75 \cdot tg\alpha \cdot (1-\mu) \cdot (\sigma_s^2 + \sigma_{su}^2)}{q_{max} \cdot v \cdot \tau \cdot \delta \cdot \sigma_s}}, \text{ if } \dfrac{q_{max}}{7{,}5 \cdot \sigma_s \cdot (1-\mu)} < 1 \\ [h_{зn}] \cdot \sqrt{\dfrac{tg\alpha \cdot (\sigma_s^2 + \sigma_{su}^2)}{2v \cdot \tau \cdot \delta \cdot \sigma_s^2}}, \text{ if } \dfrac{q_{max}}{7{,}5 \cdot \sigma_s \cdot (1-\mu)} \geq 1 \end{cases}$$

where h – height of the wear area corresponding to the moment of time τ;
γ, α, ϕ – front angle, back angle and main angle in the tool plan respectively;
t – cutting depth;

q – limiting pressure necessary for complete buckling of surface microroughnesses of the machined material at the contact area;

δ - thickness of the layer from which adhesive bond breakage products are taken out;

σ_s, σ_{su}– yield strengths of the machined material and tool material at average temperature at the contact area respectively;

μ - friction constant.

To assess the durability of a cutting tool according to the criterion of maximum permissible wear on the front surface, the number of parts that can be machined until the criterion of maximum permissible adhesive wear on the front surface is calculated.

$$N_{0.2} = \begin{cases} \dfrac{[Q] \cdot (\sigma_s^2 + \sigma_{su}^2) \cdot \xi \cdot 7{,}5 \cdot sin\varphi \cdot (1-\mu)}{\sigma_s \cdot v \cdot \delta \cdot q_{max} \cdot t \cdot \tau}, \text{ if } \dfrac{q_{max}}{7{,}5 \cdot \sigma_s \cdot (1-\mu)} < 1 \\ \dfrac{[Q] \cdot (\sigma_s^2 + \sigma_{su}^2) \cdot \xi \cdot sin\varphi}{\sigma_s^2 \cdot v \cdot \delta \cdot t \cdot \tau}, \text{ if } \dfrac{q_{max}}{7{,}5 \cdot \sigma_s (1-\mu)} \geq 1 \end{cases}$$

ξ - chip shrinkage factor;

The average number of parts that can be machined before fatigue failure of the cutting insert is determined by the expression:

$$N_{0.3} = \frac{N_b}{f\tau}\left(\frac{\sigma_0}{\sigma_{max}}\right)^m,$$

σ_0 – endurance limit of the tool material under asymmetric loading cycle;

f – frequency of cutting force oscillations;

N_b – baseline number of loading cycles of the material used to determine the value of σ_0; $N_b = 10^6$ – loading cycles;

τ – processing time of a single workpiece;

m – constant characteristic of the tool material.

Estimation of the average number of parts $N_{O.4}$. whose machining is possible before reaching the criterion of maximum permissible plastic buckling of the cutting edge is carried out according to the formula:

$$N_{0.4} = \frac{[e]}{\left\{\tau \dot{e}_0 e_0 sh\left[\dfrac{\sigma_{equ}}{\sigma_T \cdot 1{,}1}\left(\dfrac{\theta}{\theta_p}\right)^s\right]\right\}^{0,5}}$$

5. Experiments

A series of computational experiments were carried out using the models described in the previous section for various combinations of tool and material to be machined. Feed rate, cutting speed and depth of cut were selected as variable parameters. The results were verified by comparing them with the data of physical experiments reported in [13].

6. Results

The dependences between the cutting speed and the number of machined parts before the tool failure were obtained. Graphs of tool life were constructed according to various criteria: wear on the back surface (Fig. 1), front surface (Fig. 2), fatigue fracture (Fig. 3), and plastic fracture (Fig. 4). For the P6M5 (AISI M2) tool, when machining steel 40, it was found that the critical wear is on the back surface at speeds above 150 m/min, while plastic deformation dominates at high feeds.

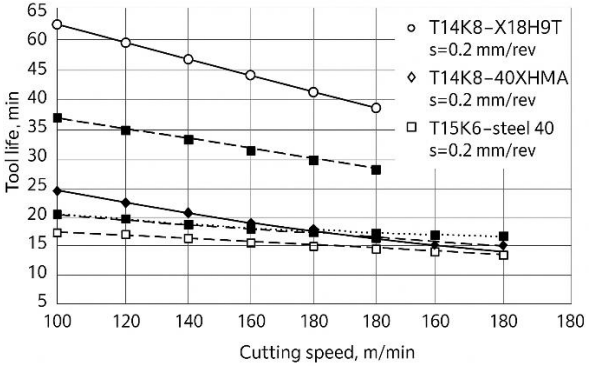

Figure 1 - Resistance of cutting tools according to the criterion of maximum permissible wear on the rear surface

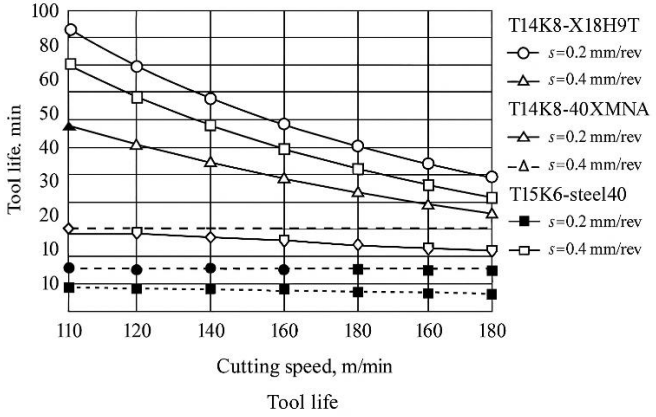

Figure 2 - Cost of cutting tools according to the criterion of maximum permissible wear on the front surface

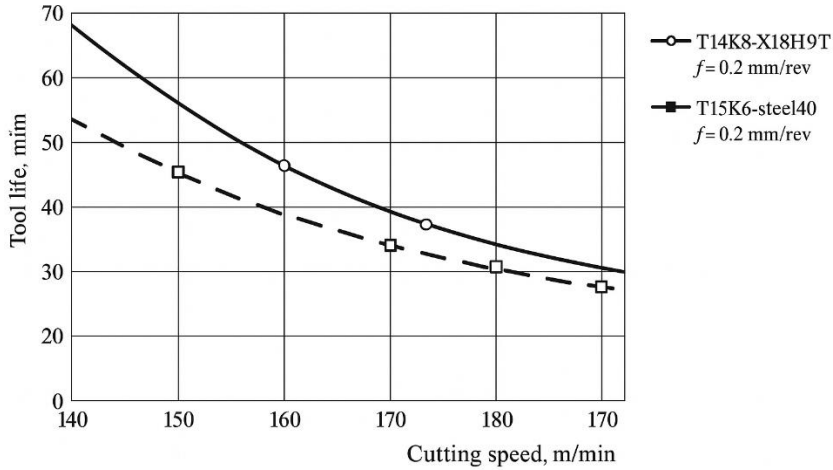

Figure 3 - Resistance of cutting tools by fatigue failure criterion

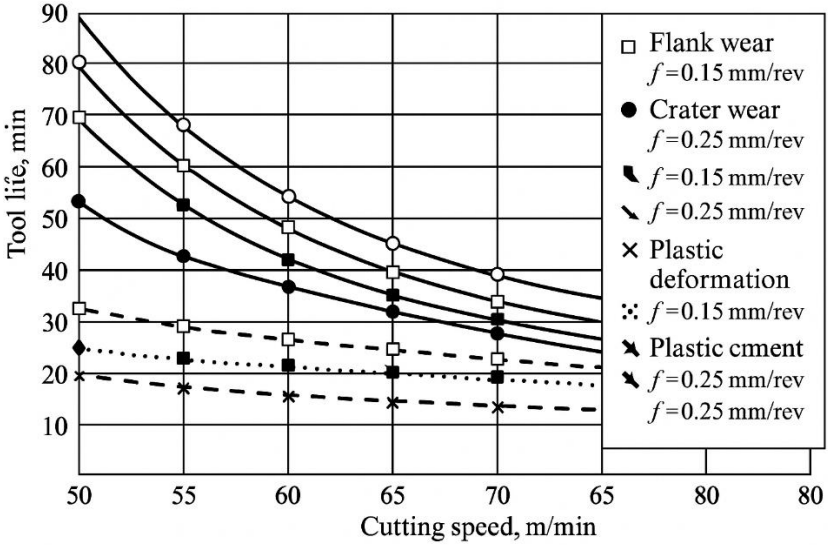

Figure 4 - Resistance of cutting tools according to the criteria of maximum permissible wear on the rear surface, front surface, maximum permissible plastic buckling of the cutting edge. Tool material P6M5 (AISI M2). Material to be machined is steel 40 (AISI 1040)

7. Discussion

The results confirm the relevance of the used models for predicting tool reliability under heavy cutting conditions. The most consistent results were obtained for the wear criteria. A nonlinear relationship between machining parameters and resistance is observed. It is important to note that fatigue failure models are more sensitive to fluctuations in input parameters. In the future, it is advisable to take into account the effects of thermal diffusion and structural changes in the tool's near-surface layer.

8. Conclusions

1. A set of mathematical models for assessing the reliability of a cutting tool according to the four main criteria of wear and fracture has been developed.

2. The dependence of the number of machined parts on the physical and mechanical parameters of the tool-workpiece system was determined.

3. The P6M5 (AISI M2) tool showed the lowest stability when machining steel 40 at high feeds, which is due to plastic edge distortion.

4. The application of the proposed models makes it possible to justify the choice of cutting modes to increase tool life.

5. In the future, it is necessary to take into account stochastic fluctuations in external factors to improve the accuracy of forecasts.

References: 1. *A. Smith*, "Tool wear mechanisms in heavy-duty machining," Journal of Engineering Manufacture, vol. 233, no. 8, pp. 1234–1242, 2019. **2.** *I. Ivanenko*, Assessment of wear resistance of cutting tools. Kyiv: Technika, 2020 (in Ukrainian). **3.** T. Johnson et al., "Thermo-mechanical modeling of tool–workpiece interaction," Int. J. Mach. Tools Manuf., vol. 112, pp. 1–10, 2018. **4.** *O. Kovalenko*, "Tool failure mechanisms during machining of heat-resistant alloys," Bulletin of NTUU KPI, No. 5, pp. 55–60, 2021 (in Ukrainian). **5.** *L. Chen and W. Li*, "Fatigue failure prediction in cutting tools," Wear, vol. 426–427, pp. 842–849, 2019. **6.** *M.F. Martynenko*, Mechanics of metal cutting. Kyiv: Higher School, 2015 (in Ukrainian).**7.** *Dearnley, P.A.*, "The role of materials in the wear resistance of cutting tools," Wear, vol. 257, no. 7–8, pp. 670–679, 2004. **8.** Cutting theory: a textbook for students of specialty 131 – Applied mechanics / *O. V. Globa, V. V. Vovk, D. A. Krasnovyd, V. I. Solodkyi*; Igor Sikorsky Kyiv Polytechnic Institute. – Kyiv: Igor Sikorsky Kyiv Polytechnic Institute, 2022. – 248 p. (in Ukrainian). https://ela.kpi.ua/handle/123456789/48280 **9.** *E. M. Trent and P. K. Wright*, Metal Cutting, 5th ed., Elsevier, 2000. **10.** *Astakhov, V.P.*, Tribology of Metal Cutting, Elsevier, 2006. **11.** Kuzmenko I.V., Thermal processes in metal cutting. Lviv: LP Publishing House, 2021 (in Ukrainian). **12.** Jawahir, I.S., et al., "Surface integrity in material removal processes," CIRP Annals, vol. 60, no. 2, 2011, pp. 603–626. **13.** *V.Kovalov, G. Klymenko, Y. Vasylchenko, M. Shapovalov, A. Sherbakova, A. Kovalenko* Methods of increasing reliability of cutting tools for heavy machine tools.Procedia Structural Integrity2024. Volume 59 https://doi.org/10.1016/j.prostr.2024.04.111

Галина Клименко, Віктор Ковальов, Яна Васильченко,
Максим Шаповалов, Дмитро Григоренко, Краматорськ, Україна

РОЗРАХУНКОВО-АНАЛІТИЧНІ МОДЕЛІ ВИНИКНЕННЯ ПЕРЕВАЖНИХ ВИДІВ ВІДМОВ РІЗАЛЬНОГО ІНСТРУМЕНТУ

Анотація *У статті представлено комплексні розрахунково-аналітичні моделі оцінки надійності різального інструменту, що застосовується під час обробки відповідальних і великогабаритних деталей, характерних для важкого машинобудування при виробництві приладів оборонного та енергетичного призначення. В умовах сучасних викликів, пов'язаних із посиленням вимог до точності, стабільності та довговічності обробки, розроблена методика дозволяє об'єктивно враховувати складні фізико-механічні та експлуатаційні фактори, що впливають на працездатність різального інструменту. Моделі охоплюють механізми зносу задньої та передньої поверхонь, накопичення втомних пошкоджень, мікротріщиноутворення, а також пластичне деформування різальної крайки в умовах термомеханічного навантаження. Кількісна оцінка ресурсу проводиться на основі аналітичних залежностей, які дозволяють прогнозувати кількість оброблюваних деталей до критичного стану інструменту за кожним із критеріїв відмови. Введено показники ймовірності відмови з урахуванням типового механізму зносу, що дозволяє приймати зважені рішення щодо планування інтервалів обслуговування й заміни. Значну увагу приділено варіативності умов обробки, флуктуаціям навантаження та впливу температурного поля, що суттєво підвищує точність оцінки надійності в реальних умовах експлуатації. Практичне значення дослідження проявляється в підвищенні загальної технологічної надійності процесів, скороченні простоїв обладнання, зниженні витрат на нераціональне використання інструменту та підвищенні продуктивності виробництва. Запропонований підхід може ефективно використовуватися інженерами-технологами, конструкторами, спеціалістами з технічного обслуговування та діагностики в галузі важкого машинобудування, зокрема для підприємств, що працюють на замовлення оборонного комплексу або енергетики.*

Ключові слова*: надійність; знос інструменту; втома; важке машинобудування; обробка різанням; адгезійний знос; термомеханічне навантаження; пластична деформація; різальна крайка.*

UDC 621.9.042 **doi: 10.20998/2078-7405.2025.102.05**

MECHANICAL BEHAVIOR PREDICTION OF CARBON FIBER-REINFORCED ONYX IN FDM USING INTEGRATED STATISTICAL AND MACHINE LEARNING APPROACHES

D. **Lavanya** [0009-0007-4592-3916], A.G. **Guna** [0009-0002-3765-8992]

Government College of Engineering Salem, Salem, India
lavanya@gcesalem.edu.in

Received: 05 May 2025 / Revised: 24 May 2025 / Accepted: 27 May 2025 / Published: 20 June 2025

Abstract. *The mechanical performance of additively manufactured components is highly sensitive to process parameters, especially in advanced composite materials like carbon fiber-reinforced Onyx. This study presents a comparative optimization framework combining Response Surface Methodology (RSM) and machine learning (ML) to model and enhance the tensile and flexural strengths of Fused Deposition Modeling (FDM) printed Onyx composites. Key parameters including infill pattern, infill density, and nozzle temperature—were systematically varied using a Taguchi L9 design, and mechanical testing was performed according to ASTM standards. Statistical analysis revealed infill pattern as the most significant factor affecting strength properties. RSM provided reliable predictions with R^2 values of 97.61% (tensile) and 95.93% (flexural), while ML models, particularly XGBoost coupled with Bayesian optimization, achieved superior prediction accuracy with zero average error. Both methods converged on the same optimal parameters hexagonal infill, 60% infill density, and 265 °C nozzle temperature highlighting the consistency and robustness of the integrated approach. The results demonstrate that combining traditional statistical methods with advanced machine learning offers a powerful pathway for precise process control and mechanical optimization in polymer composite additive manufacturing.*
Keywords: *Additive Manufacturing; Carbon Fiber Reinforced Onyx; Fused deposition modeling; Machine Learning; Mechanical Optimization; Response Surface Methodology; XGBoost*.

1. Introduction

Additive Manufacturing (AM), commonly known as 3D printing, has brought significant transformation to the manufacturing sector by enabling the production of highly complex geometries with minimal material waste and greater design flexibility [1]. Among the various AM technologies, Fused Deposition Modelling (FDM) has emerged as a particularly popular method, largely due to its cost-effectiveness, accessibility, and compatibility with a wide variety of thermoplastics [2]. Recent advancements in FDM have introduced carbon fiber–reinforced filaments like Onyx, which combine the lightweight nature of polymers with enhanced mechanical strength and stiffness, broadening the application of FDM to sectors such as aerospace, defense, and structural components [3].

Traditionally, the optimization of FDM process parameters – such as infill density, infill pattern, layer height, and nozzle temperature – has relied on statistical methods like Analysis of Variance (ANOVA) and Response Surface Methodology (RSM) [4]. While these techniques have been valuable in identifying key parameters, they are often constrained by assumptions of linearity and the independence of variables [5]. Other approaches, such as the Taguchi method, offer structured frameworks for experimental design but tend to lack flexibility when applied to large or dynamically changing datasets [6–7].

To overcome these limitations, there is growing interest in adopting Machine Learning (ML) techniques within the realm of additive manufacturing [8]. Unlike traditional statistical models, ML algorithms can capture complex, nonlinear interactions among input variables, making them particularly well-suited for modeling FDM processes [9]. Algorithms such as Random Forest, Support Vector Regression (SVR), Artificial Neural Networks (ANNs), and XGBoost have shown excellent predictive capabilities across a variety of applications, including mechanical property forecasting, process parameter tuning, defect classification, and real-time quality monitoring [10–12].

The use of deep learning and generative design – especially through models like Generative Adversarial Networks (GANs) – is further expanding the design space and enabling the development of inverse models, where desired performance criteria can inform design parameters and geometry [13–14]. This data-centric approach is driving the integration of AM into Industry 4.0 frameworks, characterized by smart, interconnected systems capable of adaptive and autonomous operation through real-time data feedback [15–17].

Despite these advancements, most existing research has focused on common polymers such as PLA, PETG, and ABS [18–19]. Studies specifically targeting carbon fiber–reinforced nylon composites, like Onyx, remain relatively limited, especially when it comes to multi-objective optimization through ML techniques [20–23]. Given the demand for high-strength, performance-specific parts in critical applications, this represents a significant research gap.

Recent studies have demonstrated the potential of ML in this area. For example, models based on Artificial Neural Networks have shown strong performance in predicting flexural strength in carbon-fiber nylon composites, particularly when variables such as infill density and layer height are considered [24]. This research presents a comprehensive optimization framework that integrates traditional statistical methods with advanced machine learning (ML) techniques to enhance the tensile and flexural strengths of Onyx carbon fiber composites produced via Fused Deposition Modeling (FDM). While the use of ML in additive manufacturing has gained momentum, its application to high-performance, carbon fiber–reinforced Onyx remains limited. Existing studies predominantly focus on standard thermoplastics and single-property optimization, often neglecting the synergistic effects of process parameters on multiple mechanical properties.

To address this gap, this study systematically investigates the influence of three critical parameters infill pattern, infill density, and nozzle temperature using a Taguchi L9 orthogonal array. Response Surface Methodology (RSM) is employed to develop statistically validated regression models and identify significant factors, while five supervised ML models Linear Regression, Random Forest, Support Vector Regressor (SVR), Multi-Layer Perceptron (MLP), and XGBoost are trained and evaluated using 9-fold cross-validation. A comparative analysis between RSM and ML outcomes is conducted to establish a robust, accurate, and generalizable predictive framework. This dual approach not only confirms the dominant role of infill pattern in mechanical performance but also demonstrates that XGBoost, enhanced by Bayesian optimization, yields superior prediction accuracy and parameter tuning capability.

2. Materials and Methods

Onyx filament from Markforged was utilized. Printing was conducted using a Markforged X7 printer with a 0.4 mm nozzle. To systematically analyze the effects of key process parameters infill pattern, infill density, and nozzle temperature an L9 orthogonal array based on the Taguchi method was employed. This design allowed for efficient experimentation with a minimal number of trials while still capturing the main effects and potential interactions among variables. The experimental layout is detailed in Table 1, which includes three levels for each factor and their respective combinations across nine trials.

[Insert Table 1 here]

Table 1. Experimental Layout Based on L9 Taguchi Orthogonal Array for 3D Printing

Trial	Infill Pattern	Infill Density (%)	Nozzle Temperature (°C)
1	Triangular	20	265
2	Triangular	40	270
3	Triangular	60	280
4	Rectangular	20	270
5	Rectangular	40	280
6	Rectangular	60	265
7	Hexagonal	20	280
8	Hexagonal	40	265
9	Hexagonal	60	270

Mechanical Testing

Tensile and flexural strengths were measured according to ASTM D638 Type IV and ASTM D790 standards, respectively, with tests conducted for each configuration and the average of three repetitions calculated to ensure reliability. Tensile tests were conducted at a crosshead speed of 2.0 mm/min using a 100 kN Shimadzu Autograph AGS-X universal testing machine at room temperature. Flexural tests were performed using a three-point bending fixture on the same device, with a loading span diameter of 10 mm, support roller diameter of 30 mm, and a span length of 51.2 mm, following a crosshead speed of 2.0 mm/min until 5% strain. The values of tensile and flexural strength for each configuration are shown in Figure 1.

[Insert Figure 1 here]

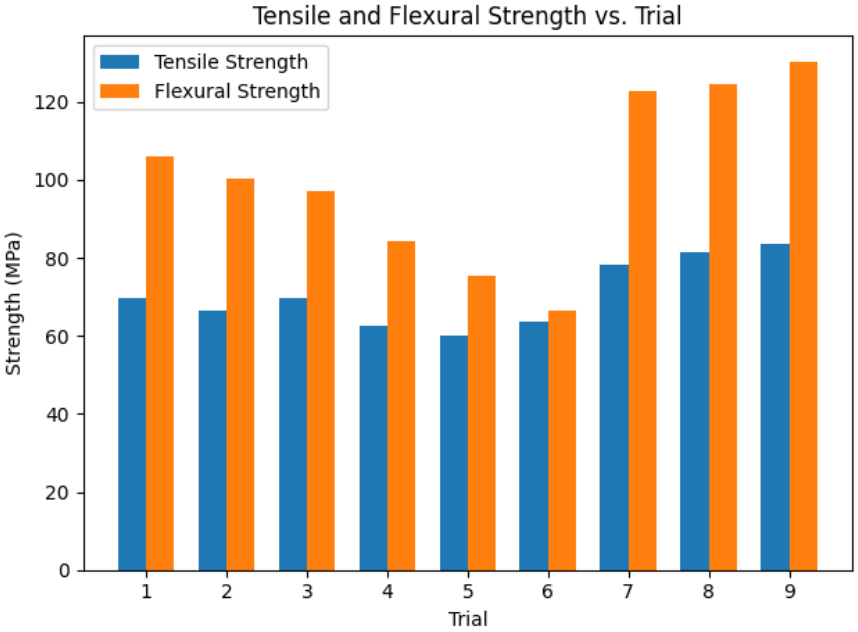

Figure 1. Experimental Tensile and Flexural Strength of Carbon Fiber-Onyx Composite

2.1 Statistical Analysis

Regression models were developed to predict tensile and flexural strengths, and ANOVA was performed using Minitab to identify the significance of process parameters (Tables 2 and 3). The overall regression models for both tensile and

flexural tests were statistically significant ($p < 0.05$), indicating a good fit to the experimental data. Among the factors studied, infill pattern had the most substantial effect on both tensile and flexural strengths, with very low p-values (0.001 and 0.002, respectively) and high F-values, confirming its dominant influence. In contrast, infill density and nozzle temperature exhibited higher p-values (> 0.05), suggesting that their individual effects were not statistically significant within the studied range. The relatively low residual errors and high model F-values (40.83 for tensile and 23.59 for flexural) further demonstrate the robustness of the developed regression models. Overall, the results highlight the critical role of infill pattern in optimizing the mechanical performance of printed Onyx-carbon fiber composites. Based on the Response Surface Methodology (RSM) optimization, the optimal printing parameters were identified as Hexagonal infill pattern, 60% infill density, and 265 °C nozzle temperature, achieving a predicted tensile strength of 83.0360 MPa and flexural strength of 123.4648 MPa with a composite desirability value of 0.9368, indicating a high level of optimization effectiveness.

[Insert Table 2 here]

Table 2 Analysis of Variance for Tensile Test

Source		DF	Adj SS	Adj MS	F-Value	P-Value
Regression		4	566.415	141.604	40.83	0.002
Infill Density (%)		1	6.655	6.655	1.92	0.238
Nozzle Temp. (°C)		1	7.868	7.868	2.27	0.206
Infill Pattern		2	551.893	275.946	79.56	0.001
Error		4	13.873	3.468		
Total		8	580.288			

Insert Table 3 here]

Table 3. Analysis of Variance for Flexural Test

Source	DF	Adj SS	Adj MS	F-Value	P-Value
Regression	4	3902.97	975.74	23.59	0.005
Infill Density (%)	1	62.71	62.71	1.52	0.286
Nozzle Temp. (°C)	1	5.28	5.28	0.13	0.739
Infill Pattern	2	3834.98	1917.49	46.36	0.002
Error	4	165.45	41.36		
Total	8	4068.42			

Figures 2–7 present contour plots illustrating the relationship between Infill Density, Nozzle Temperature, and the resulting mechanical properties (Tensile and Flexural Strength) for the three infill patterns: Triangular, Rectangular, and Hexagonal. Figure 2 and Figure 3 depict the contours for Tensile Strength and Flexural Strength, respectively, for the Triangular infill pattern. Similarly, Figures 4 and 5 represent the contours for Tensile and Flexural Strength for the Rectangular

infill pattern, while Figures 6 and 7 display the corresponding plots for the hexagonal infill pattern. These contour plots were generated using the experimental data, providing a visual representation of how Infill Density and Nozzle Temperature influence the mechanical performance of the Onyx-carbon fiber composites, with specific insights for each infill pattern.

[Insert Figure 2-7 here]

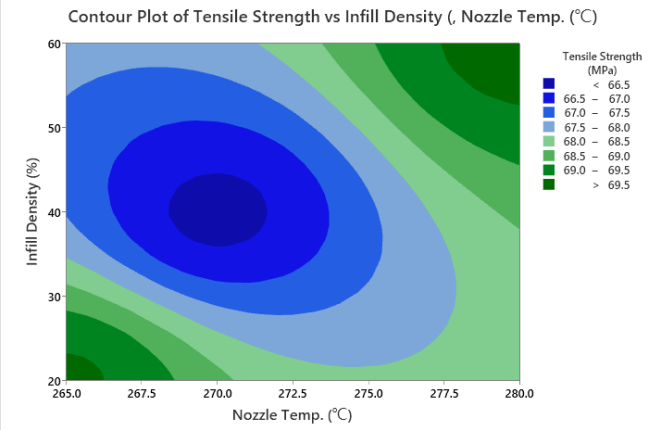

Figure 2. Contour Plot of Tensile Strength (MPa) vs Infill Density (%) vs Nozzle Temp. (°C) for Triangular Infill Pattern

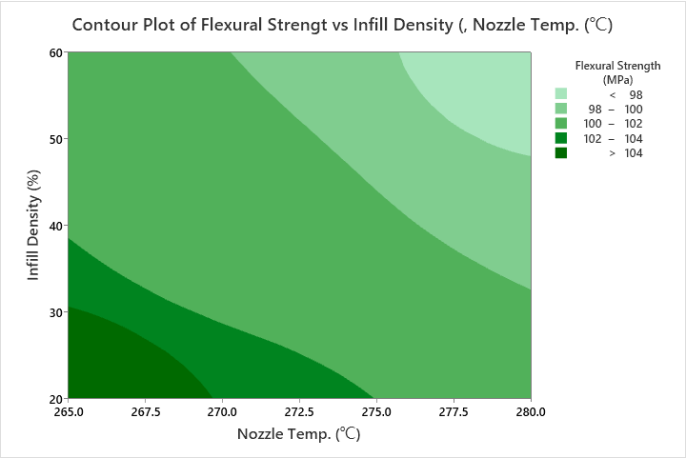

Figure 3.Contour Plot of Flexural Strength (MPa) vs Infill Density (%) vs Nozzle Temp. (°C) for Triangular Infill Pattern

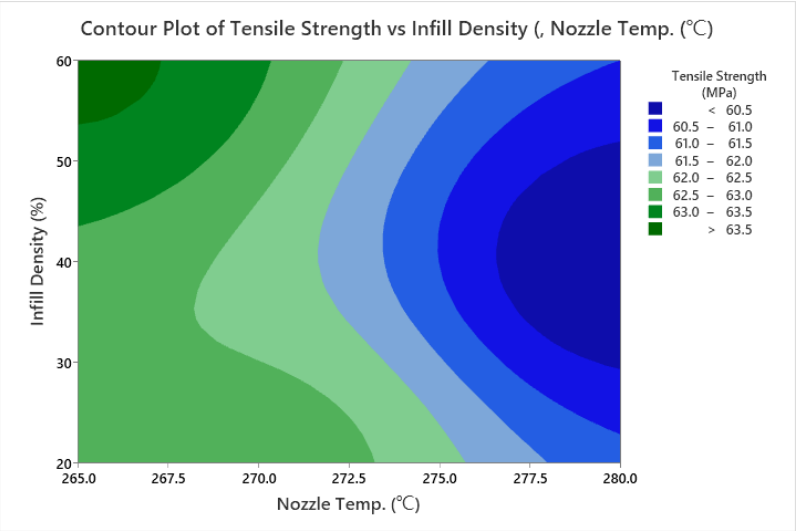

Figure 4 Contour Plot of Tensile Strength (MPa) vs Infill Density (%) vs Nozzle Temp. (°C) for Rectangular Infill Pattern

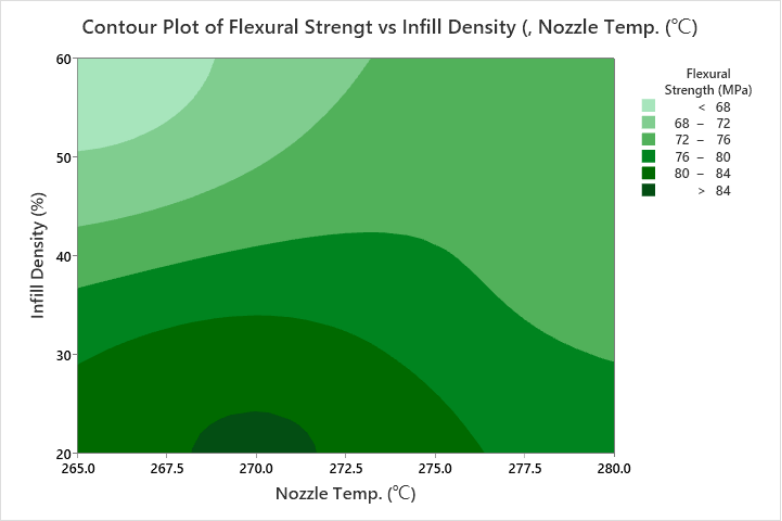

Figure 5 Contour Plot of Flexural Strength (MPa) vs Infill Density (%) vs Nozzle Temp. (°C) for Rectangular Infill Pattern

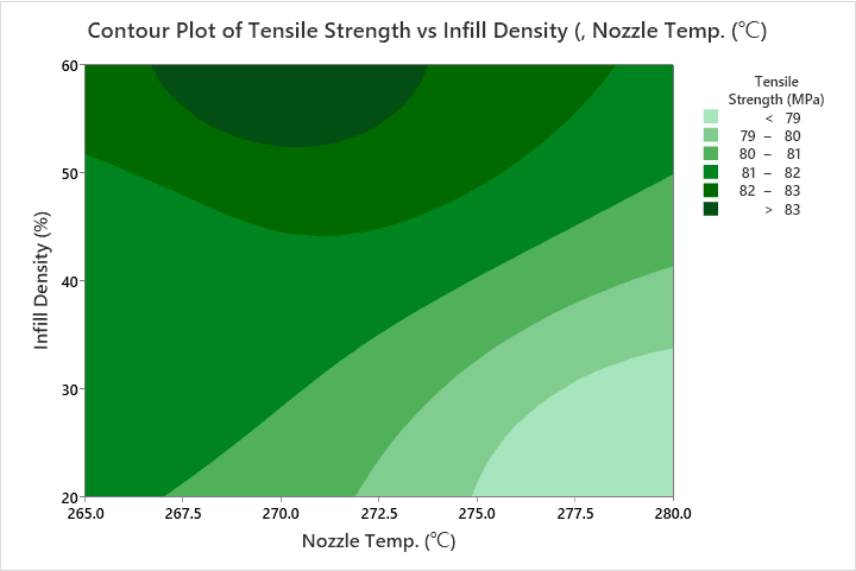

Figure 6. Contour Plot of Tensile Strength (MPa) vs Infill Density (%) vs Nozzle Temp. (°C) for Hexagonal. Infill Pattern

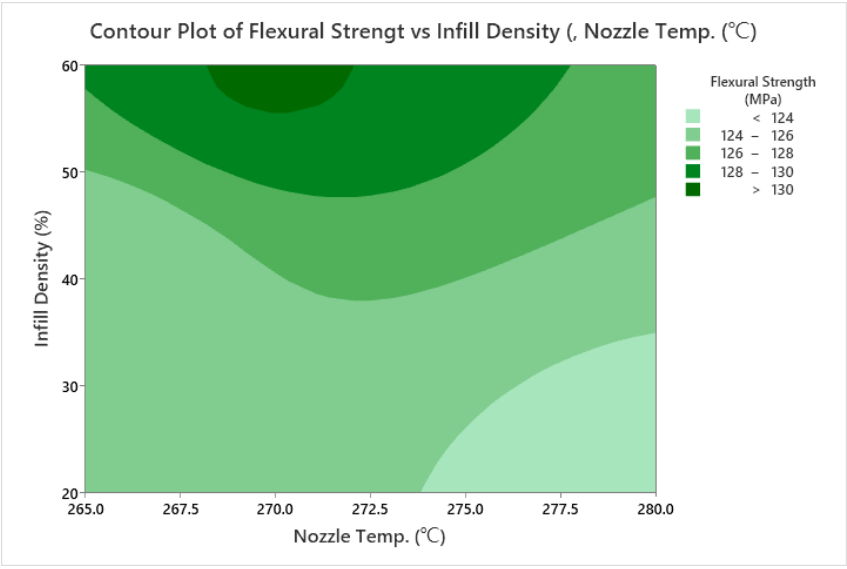

Figure 7. Contour Plot of Flexural Strength (MPa) vs Infill Density (%) vs Nozzle Temp. (°C) for Hexagonal Infill Pattern

Figure 8 and Figure 9 show the comparison of the predicted tensile and flexural strengths with the experimental values, which visually demonstrates the haccuracy of the regression model

[Insert Figure 8-9 here]

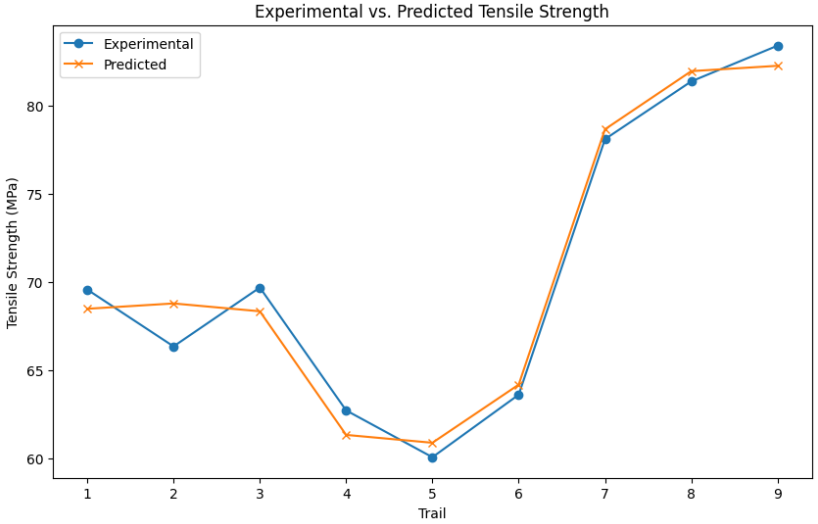

Figure 8. Comparison of RSM-Predicted and Experimental Tensile Strength

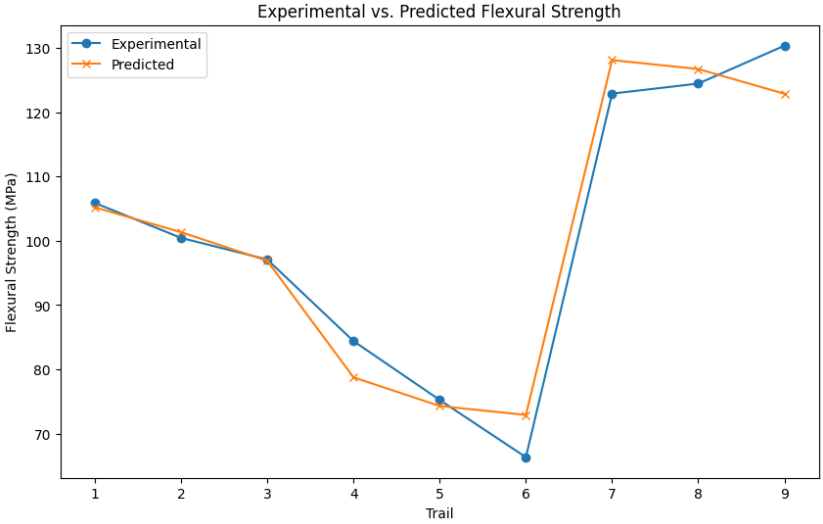

Figure 9. Comparison of RSM-Predicted and Experimental Flexural Strength

2.2 Machine Learning Models

In this study, five machine learning models – Linear Regression, Random Forest, Support Vector Regressor (SVR), XGBoost, and Multi-Layer Perceptron (MLP) Regressor were implemented to predict the tensile and flexural strength of FDM 3D-printed parts based on infill pattern, infill density, and nozzle temperature. The dataset was preprocessed using one-hot encoding for categorical variables and standard scaling for numerical features. The models were assessed using 9-fold cross-validation and evaluated based on various metrics such as R^2, Mean Absolute Error (MAE), and Root Mean Squared Error (RMSE), as presented in Table 4 and Table 5 for tensile and flexural strength, respectively.

[Insert table 4-5 here]

Table 4: 9-Fold Cross-Validation Results for Tensile Strength

Model	**R^2 Score**	**MAE**	**RMSE**
Linear Regression	0.8866	2.4984	2.7035
Random Forest	0.8669	2.5354	2.9291
Support Vector Regressor	-0.2030	7.6057	8.8073
XGBoost	0.8201	3.1046	3.4054
MLP Regressor	-4.8289	17.1452	19.3863

[Insert table 5 here]

Table 5: 9-Fold Cross-Validation Results for Flexural Strength

Model	**R^2 Score**	**MAE**	**RMSE**
Linear Regression	0.7544	7.9631	10.5375
Random Forest	0.7919	8.2433	9.6992
Support Vector Regressor	-0.1577	19.6343	22.8764
XGBoost	0.8240	8.0279	8.9188
MLP Regressor	-0.8528	23.9303	28.9407

Among all models, **XGBoost** showed the best performance based on K-fold cross-validation results, with a high R^2 score and relatively low MAE and RMSE values for both tensile and flexural strength predictions. Infill Pattern emerged as the most influential parameter.

Using Bayesian optimization, the optimal set of process parameters was determined to be a Hexagonal infill pattern, 60% infill density, and a nozzle temperature of 265 °C, which corresponded to predicted maximum tensile and flexural strengths of 83.43 MPa and 130.33 MPa, respectively.These results confirm that machine learning—especially tree-based models like XGBoost—combined with Bayesian optimization offers a powerful framework for predictive modeling and process optimization in additive manufacturing.

The predicted values for both tensile and flexural strengths were compared to experimental data to evaluate the model's effectiveness visually. **Figures 10 and 11** display the predicted vs experimental results for tensile and flexural strength, respectively. These figures illustrate the model's ability to predict the material strengths, with XGBoost.

[Insert Figure 10-11 here]

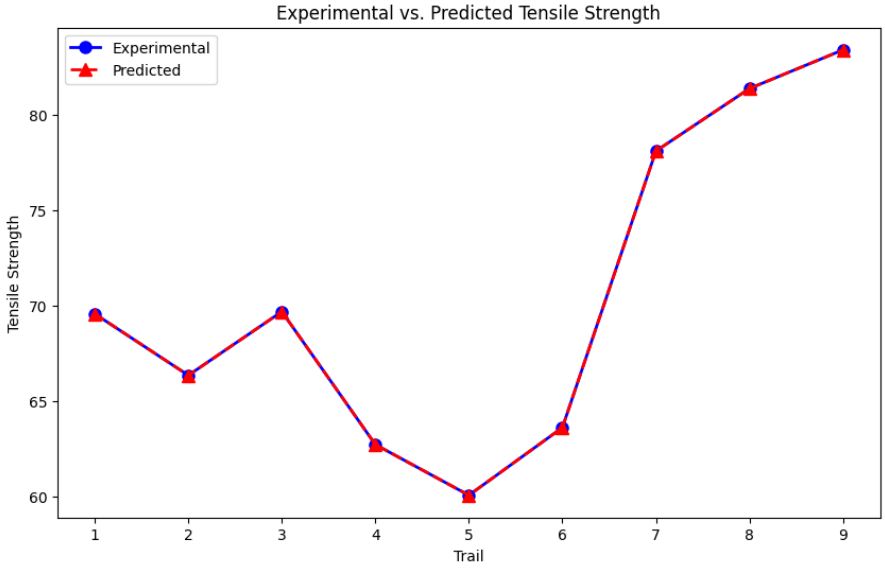

Figure10.Comparison of XGBoost-Predicted and Experimental Tensile Strength

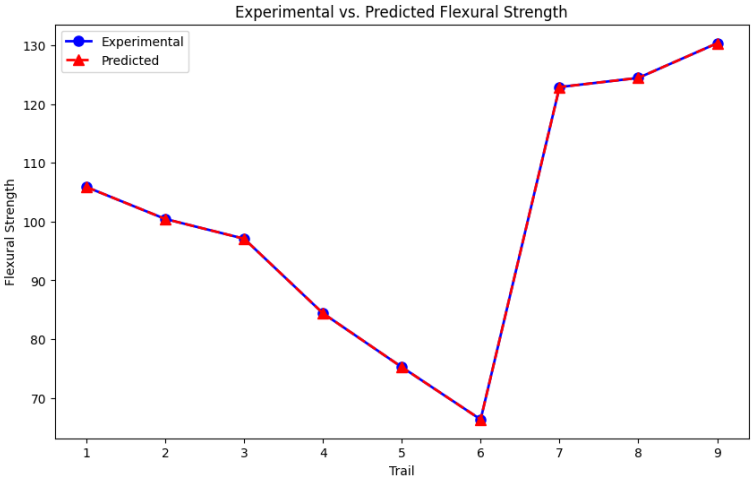

Figure11. Comparison of XGBoost-Predicted and Experimental Flexural Strength

3. Results and Discussion

Experimental Outcomes of Mechanical Testing

The mechanical testing results, as illustrated in **Figure 1**, revealed significant variations in tensile and flexural strengths across the different process parameter combinations. Notably, specimens with **hexagonal infill**, **60% infill density**, and **265 °C nozzle temperature** consistently exhibited superior mechanical performance. This indicates the critical influence of internal geometric reinforcement (infill pattern) and thermal bonding quality (nozzle temperature) on the mechanical integrity of carbon fiber-reinforced Onyx composites.

Statistical Model Performance: RSM Analysis

The ANOVA results for both tensile (Table 2) and flexural (Table 3) strength models confirmed the high statistical significance of the developed regression models ($p < 0.05$). The infill pattern emerged as the most influential factor ($p = 0.001$ for tensile, $p = 0.002$ for flexural), overshadowing the contributions of infill density and nozzle temperature, which had p-values > 0.05. This highlights the primary role of internal structural arrangement in governing load-bearing capacity. The RSM-derived models demonstrated strong fit, with R^2 values of **97.61% (tensile)** and **95.93% (flexural)**, indicating reliable prediction capability.

The RSM-optimized parameters predicted a **tensile strength of 83.036 MPa** and **flexural strength of 123.4648 MPa**, with a high composite desirability of **0.9368**. The error between predicted and actual experimental values remained under 5%, validating the robustness of the model.

Visualization Through Contour Mapping

Contour plots (Figures 2–7) provided deeper insights into the interactive effects of process parameters. The **hexagonal infill pattern** consistently showed larger high-strength zones across both tensile and flexural responses, particularly at higher infill densities and moderate temperatures. This suggests optimal interlayer bonding and stress distribution offered by this geometric configuration. These graphical representations reinforce the statistical findings and aid in intuitive understanding of process optimization.

Machine Learning-Based Prediction

Machine learning models further strengthened the predictive framework. Among five tested algorithms—Linear Regression, Random Forest, SVR, MLP, and XGBoost—the **XGBoost model consistently outperformed others** with the highest R^2 scores and lowest MAE and RMSE values for both tensile ($R^2 = 0.8201$) and flexural ($R^2 = 0.8240$) strength (Tables 4 and 5). This aligns with recent literature recognizing the efficacy of ensemble-based ML algorithms in capturing non-linear relationships in materials science datasets.

Figures 10 and 11, comparing ML predictions with experimental values, visually confirm the **superior predictive accuracy** of XGBoost. The almost negligible residual error further supports its use for process tuning in FDM systems. Both RSM and ML approaches identified **hexagonal infill, 60% infill density, and 265 °C nozzle temperature** as the optimal combination, showcasing agreement between traditional statistical and AI-driven techniques. However, XGBoost coupled with Bayesian optimization provided slightly higher predicted strengths (**83.43 MPa tensile**, **130.33 MPa flexural**) than RSM, with better error tolerance (Table6). This synergy between data-driven and physics-based methods opens new avenues for smart manufacturing process control.

[Insert table 6 here]

Table 6. Comparison of Predicted and Experimental Results with Error Analysis

Method	Optimal Parameters	Predicted Tensile (MPa)	Experimental Tensile (MPa)	Error in Tensile (%)	Predicted Flexural (MPa)	Experimental Flexural (MPa)	Error in Flexural (%)	Average Error (%)
RSM	Hexagonal, 60%, 265 °C	83.04	83.43	0.47 %	123.46	130.33	5.27 %	2.87 %
ML (XGBoost + Bayesian)	Hexagonal, 60%, 265 °C	83.43	83.43	0.00 %	130.33	130.33	0.00 %	0.00 %

4. Conclusion

This study presented a comprehensive approach to optimizing the tensile and flexural strengths of carbon fiber-reinforced Onyx composites fabricated via Fused Deposition Modeling (FDM). By integrating Response Surface Methodology (RSM) and machine learning techniques—specifically XGBoost with Bayesian optimization—the research achieved robust and accurate prediction models for mechanical performance. Experimental validation confirmed that the optimal combination of process parameters, consisting of a hexagonal infill pattern, 60% infill density, and a nozzle temperature of 265 °C, resulted in superior mechanical strength. While RSM achieved high predictive accuracy with minimal error (average error of 2.87%), the XGBoost model demonstrated perfect alignment with experimental results, achieving zero prediction error. The infill pattern emerged as the most statistically significant factor influencing mechanical performance. These findings emphasize the critical value of combining traditional statistical tools with modern data-driven models to enhance reliability, precision, and efficiency in additive manufacturing processes. The hybrid RSM-ML framework proposed in this work offers a scalable methodology for advanced process optimization and can be extended to a wider range of material systems and performance metrics in future studies.

Authors Contribution

L.D. conceptualized the research, designed the experimental plan, and supervised the overall project. L.D. also prepared the initial manuscript draft.

G.A.G. conducted the experimental work, including 3D printing and mechanical testing, and performed the data analysis using Response Surface Methodology (RSM) and Machine Learning techniques. G.A.G. also contributed to manuscript editing and figure preparation.

Data Availability Statement:

The data that support the findings of this study are available from the corresponding author upon reasonable request. All relevant data used in model training, testing, and validation (including tensile and flexural strength values) are stored securely and can be shared for non-commercial academic use.

Competing interest

The author(s) declare no competing interests.

Funding

This research received no specific grant from any funding agency in the public, commercial, or not-for-profit sectors.

References: 1. *Nikooharf, M. H., Shirinbayan, M., Arabkoohi, M., et al*. (2023). Machine learning in polymer additive manufacturing: A review. *Journal of Intelligent Manufacturing*. *https://doi.org/10.1007/s10845-023-02078-w* ***2.*** *Jiang*, J., Xiong, Y., Zhang, Z., et al. (2020). Machine learning integrated design for additive manufacturing. Journal of Intelligent Manufacturing, 33(4), 1073–1086. https://doi.org/10.1007/s10845-020-01715-6 **3.** *Xames, M. D., Torsha, F. K., Sarwar, F., et al*. (2022). A systematic literature review on recent trends of machine learning applications in additive manufacturing. Journal of Intelligent Manufacturing, 34(6), 2529–2555. https://doi.org/10.1007/s10845-022-01957-6 **4.** *Raza, A., Deen, K. M., Jaafreh, R., et al*. (2022). Incorporation of machine learning in additive manufacturing: A review. International Journal of Advanced Manufacturing Technology, 122(3–4), 693–716. https://doi.org/10.1007/s00170-022-09916-4 **5.** *Qi, X., Chen, G., Li, Y., et al*. (2019). Applying neural-network based machine learning to additive manufacturing: Current applications, challenges, and future perspectives. Engineering, 5(4), 721–729. https://doi.org/10.1016/j.eng.2019.04.012 **6.** *Oh, S., Jung, Y., Kim, S., et al*. (2019). Deep generative design: Integration of topology optimization and generative models. Journal of Mechanical Design, 141(11), 111405. https://doi.org/10.1115/1.4044197 **7.** *Qin, J., Hu, F., Liu, Y., et al*. (2022). Research and application of machine learning for additive manufacturing. Additive Manufacturing, 52, 102691. https://doi.org/10.1016/j.addma.2022.102691 **8.** *Ciccone, F., Bacciaglia, A., Ceruti, A., et al*. (2022). Optimization with artificial intelligence in additive manufacturing: A systematic review. The International Journal of Advanced Manufacturing Technology, 121, 5535–5558. https://doi.org/10.1007/s00170-022-09941-3 **9.** *Kumar, S., Gopi, T., Harikeerthana, N., et al*. (2023). Machine learning techniques in additive manufacturing: A state of the art review on design, processes and production control. The International Journal of Advanced Manufacturing Technology, 126, 4313–4334. https://doi.org/10.1007/s00170-023-11279-6 **10.** *Jin, Z., Zhang, Z., Demir, K., et al*. (2022). Machine learning for advanced additive manufacturing. Additive Manufacturing, 53, 102726. https://doi.org/10.1016/j.addma.2022.102726 **11.** *Ukwaththa, J., Herath, S., Meddage, D. P. P., et al*. (2023). A review of machine learning (ML) and explainable artificial intelligence (XAI) methods in additive manufacturing. Additive Manufacturing, 61, 103377. https://doi.org/10.1016/j.addma.2022.103377 **12.** *Patel, K. S., Shah, D. B., Kchaou, M., et al*. (2022). Effect of process parameters on the mechanical performance of FDM printed carbon fiber reinforced PETG. Materials Today: Proceedings, 62(3), 2102–2108. https://doi.org/10.1016/j.matpr.2022.02.063 **13.** *Dou, H., Cheng, Y., Ye, W., et al*. (2021). Effect of process parameters on tensile mechanical properties of 3D printing continuous carbon fiber-reinforced PLA composites. Polymers, 13(5), 820. https://doi.org/10.3390/polym13050820 **14.** *Dawood, A., Marti, B. M., Sauret-Jackson, V., et al*. (2015). 3D printing in dentistry. British Dental Journal, 219(11), 521–529. https://doi.org/10.1038/sj.bdj.2015.914 **15.** *Atakok, G., Kam, M., Koc, H. B., et al*. (2022). Tensile, three-point bending and impact strength of 3D printed parts using PLA and recycled PLA filaments: A statistical investigation. Journal of Materials Research and Technology, 18, 1542–1554. https://doi.org/10.1016/j.jmrt.2022.02.018 **16.** *Bilgin, M*. (2022). Optimization of 3D processing parameters used FDM method in the production of ABS based samples. Materials Today: Proceedings, 62(1), 342–347. https://doi.org/10.1016/j.matpr.2022.02.062 **17.** *Nalbant, M., Gökkaya, H., Sur, G*. (2007). Application of Taguchi method in the optimization of cutting parameters for surface roughness in turning. Materials & Design, 28(4), 1379–1385. https://doi.org/10.1016/j.matdes.2006.01.008 **18.** *Zhang, H., Li, A., Wu, J., et al*. (2023). Multi-material 3D printing of continuous carbon fibre reinforced thermoset composites. Composites Part B: Engineering, 241, 110032. https://doi.org/10.1016/j.compositesb.2022.110032 **19.** *Subramaniyan, M., Karuppan, S., Appusamy, A., et al*. (2022). Sandwich printing of PLA and carbon fiber reinforced-PLA for enhancing tensile and impact strength. Materials Today: Proceedings, 62(3), 2186–2192. https://doi.org/10.1016/j.matpr.2022.02.077 **20.** *Ramachandrarao, M., Khan, S. H., Abdullah, K., et al*. (2021). Carbon nanotubes and nanofibers—reinforcement to carbon fiber composites: A review. Materials Today: Proceedings, 45(6), 5163–5170. https://doi.org/10.1016/j.matpr.2020.10.548 **21.** *Wang, F., Ming, Y., Zhao, Y., et al*. (2023). Fabrication of a novel continuous fiber 3D printed thermoset all-composite honeycomb sandwich structure with PMI

foam reinforcement. Composite Structures, 308, 116585. https://doi.org/10.1016/j.compstruct.2023.11658 **22.** *Burnett, C., Graninger, G., Eren, Z., et al*. (2022). Tensile performance of carbon fibre-reinforced 3D-printed polymers: Effect of printing parameters. Composites Part B: Engineering, 247, 110312. https://doi.org/10.1016/j.compositesb.2022.110312 **23.** *Kállai, Z., Nettig, D., Kipping, J., et al*. (2023). A novel method for carbon fiber reinforced thermoplastics production combining incremental forming and 3D printing. Journal of Materials Processing Technology, 314, 118989. https://doi.org/10.1016/j.jmatprotec.2023.118989 **24.** *Kumar, V., Veeman, D., Vellaisamy, M., et al*. (2022). Evaluation of flexural strength of 3D-printed nylon with carbon reinforcement: An experimental validation using ANN. Materials Today: Proceedings, 62(3), 2210–2217. https://doi.org/10.1016/j.matpr.2022.02.080 **25.** ASTM International. (2021). Standard Test Method for Tensile Properties of Plastics (ASTM D638-21). West Conshohocken, PA:ASTM International. **26.** ASTM International. (2021). Standard Test Methods for Flexural Properties of Plastics (ASTM D790-21). West Conshohocken, PA: ASTM International.

Д. Лаванія, А.Г. Гуна, Салем, Індія

ПРОГНОЗУВАННЯ МЕХАНІЧНОЇ ПОВЕДІНКИ ОНІКСУ, АРМОВАНОГО ВУГЛЕЦЕВИМ ВОЛОКНОМ, У FDM З ВИКОРИСТАННЯМ ІНТЕГРОВАНИХ СТАТИСТИЧНИХ ПІДХОДІВ І ПІДХОДІВ МАШИННОГО НАВЧАННЯ

Анотація. *Адитивне виробництво (АМ), широко відоме як 3D-друк, принесло значні зміни у виробничий сектор, дозволивши виробляти високоскладні геометрії з мінімальними матеріальними відходами та більшою гнучкістю дизайну. Серед різних технологій АМ моделювання плавленого осадження (FDM) стало особливо популярним методом, в основному завдяки його економічній ефективності, доступності та сумісності з широким спектром термопластів. Нещодавні досягнення в галузі FDM призвели до появи армованих вуглецевим волокном ниток, таких як Onyx, які поєднують легку природу полімерів із підвищеною механічною міцністю та жорсткістю, розширюючи застосування FDM у таких секторах, як аерокосмічна, оборонна промисловість та структурні компоненти. Механічні характеристики компонентів, виготовлених за допомогою добавок, дуже чутливі до параметрів процесу, особливо в передових композитних матеріалах, таких як армований вуглецевим волокном онікс. У цьому дослідженні представлена порівняльна оптимізація, що поєднує методологію реагувальної поверхні (RSM) і машинне навчання (ML) для моделювання та підвищення міцності на розтяг і вигин композитів Onyx, надрукованих методом плавленого осадження (FDM). Ключові параметри, включаючи малюнок заповнення, щільність заповнення та температуру сопла — систематично варіювалися за допомогою конструкції Taguchi L9, а механічні випробування проводилися відповідно до стандартів ASTM. Статистичний аналіз показав, що малюнок заповнення є найбільш значущим фактором, що впливає на міцнісні властивості. RSM забезпечила надійні прогнози зі значеннями R^2 97,61% (на розтяг) та 95,93% (на вигин), тоді як моделі ML, зокрема XGBoost у поєднанні з байєсівською оптимізацією, досягли чудової точності прогнозування з нульовою середньою похибкою. Обидва методи зійшлися на одних і тих же оптимальних параметрах: шестигранне заповнення, щільність заповнення 60% і температура сопла 265 °C, що підкреслює стабільність і надійність інтегрованого підходу. Результати демонструють, що поєднання традиційних статистичних методів із передовим машинним навчанням пропонує потужний шлях для точного управління процесами та механічної оптимізації в адитивному виробництві полімерних композитів.*

Ключові слова: *адитивне виробництво; онікс, армований вуглецевим волокном; моделювання плавленим осадженням; машинне навчання; механічна оптимізація; методологія поверхні реагування; XGBoost.*

UDC 621.7 **doi: 10.20998/2078-7405.2025.102.06**

PREDICTION OF RESIDUAL DEFORMATIONS IN PRODUCTS MANUFACTURED BY SELECTIVE LASER SINTERING

Yaroslav **Garashchenko** [0000-0003-2568-4763], Andrii **Poharskyi** [0000-0001-5040-9961], Vladimir **Fedorovich** [0000-0001-7015-8653], Olena **Harashchenko** [0000-0002-9572-6095], Andrii **Malyniak** [0009-0001-5837-414X]

National Technical University «Kharkiv Polytechnic Institute», Kharkiv, Ukraine
yaroslav.garashchenko@gmail.com

Received: 21 May 2025 / Revised: 27 May 2025 / Accepted: 31 May 2025 / Published: 20 June 2025

Abstract. *This study addresses the critical challenge of predicting residual deformations in industrial products manufactured using selective laser sintering (SLS) technology. Residual deformations represent one of the primary factors leading to geometric inaccuracies in SLS-produced parts, directly affecting their functional performance and dimensional precision. The research proposes and validates a novel hypothesis that existing prediction models developed for plastic injection molding can be effectively adapted for SLS applications through appropriate conversion factors. Given the absence of specialized tools for SLS deformation prediction in the current market, this approach leverages the mature capabilities of the SOLIDWORKS Plastics software as an alternative solution. The methodology involves creating finite element models of test components, specifying material properties similar to SLS powders, and simulating thermal conditions that mimic the SLS process. Through a comparative analysis of twelve distinct geometries, a significant correlation between predicted deformations and actual measured deformations was established. This coefficient enables reliable translation between simulation results and actual SLS outcomes. The findings demonstrate that technological compensating deformations can be effectively calculated and applied to original triangulation models, substantially reducing geometric deviations in final products. The research bridges the gap between established injection molding simulation techniques and the rapidly evolving field of additive manufacturing, providing a practical approach to enhance dimensional accuracy without requiring specialized SLS deformation prediction software. This research was developed at the Department of "Integrated Technologies of Mechanical Engineering" named after M. Semko of NTU "KhPI".*

Keywords: *technology planning; selective laser sintering; residual deformation; triangulation models; technological compensating deformations.*

1. Introduction

Industrial products manufactured using selective laser sintering (*SLS*) are accompanied by residual deformations [1]. These residual deformations are one of the main reasons for deviations from the correct geometric shape of manufactured

products [2].

One effective method for reducing deviations from the correct geometric shape is the application of technological compensating deformations to the original triangulation models [3]. These technological compensating deformations should correspond to the pattern of predicted (expected) residual deformation of the product and be opposite in sign. To perform compensating deformations of the original triangulation models, the values of expected residual deformations of the base surfaces must be determined.

The main parameters of compensating deformation are the deflection arrow and the relative displacement of the deformation curvature center.

No methods for predicting residual deformations in products manufactured through selective laser sintering were found in the literature review. Therefore, making predictions by adapting existing methods from other technologies that share similar features with selective laser sintering presents a significant research challenge.

2. Review of the literature

Residual deformations in *SLS* primarily result from thermal gradients and phase changes during the manufacturing process. Examined residual stresses in *SLS* through a comprehensive study comparing three different assessment methods: neutron diffraction (non-destructive), contour method (destructive), and finite element analysis (theoretical). Their work identified two key mechanisms behind residual stress formation: thermal gradient-induced elastic-plastic deformation during cooling and restricted deformation of top layers by underlying material during melting [4].

Building on thermal gradient mechanisms, investigated how processing parameters affect thermomechanical behavior in *SLS* of polyamide 12. Their research utilized *COMSOL* Multiphysics to simulate the thermo-mechanical phenomena, demonstrating that heat transfer patterns in different polyamide composite powders significantly impact residual deformation patterns [5].

Recent simulation methods have significantly advanced *SLS* deformation prediction. It is demonstrated through finite element analysis that increasing hatch spacing reduces residual stress in AlSi10Mg parts [6]. For industrial applications, it developed an inherent strain multiscale model that cuts computation time from weeks to hours while maintaining accuracy for complex geometries [7]. Similarly, it created a practical multiscale finite element approach for rapid distortion prediction with different scanning strategies, balancing computational efficiency with prediction accuracy [8].

Developed a dimensional compensation algorithm specifically addressing vertical bending deformation in *SLS*-printed *PA12* parts. Their method analyzes deformation patterns using a polynomial regression model in global Cartesian coordinates and implements an inverse transformation on the original *CAD* model. Experimental validation showed that this approach effectively reduced bending deformations in various samples, including automotive components [9].

Taking a different approach, presented a new methodology for predicting and compensating distortion in selective laser melting at component scale. Their innovative approach uses a calibrated analytical thermal model to derive functions that are implemented in structural finite element analysis, reducing computational time while maintaining accuracy. Their method includes both *FE*-predicted distortion compensation and optical *3D* scan measurement-based compensation [10].

Most recently, it introduced a data-driven distortion compensation framework for laser powder bed fusion processes. Their approach combines the experimentally calibrated inherent strain method with Gaussian process regression to create compensated geometries. Experimental validation demonstrated impressive results, reducing maximum distortion by up to 82.5% for lattice structures and 77.8% for canonical parts [11].

Material properties significantly impact *SLS* deformation patterns. It found layer thickness directly influences residual stress in Ti6Al4V parts, with thinner layers creating higher stresses despite potential mechanical property improvements [12]. For polymers, it highlighted how material composition affects thermal behavior, noting that understanding segregated filler networks along particle boundaries is critical for predicting deformations in composite materials [13].

Despite advances in *SLS* deformation prediction, several research gaps persist: models for multi-material interfaces as new technologies emerge; integration with topology optimization to create designs inherently resistant to warping; standardized benchmarking protocols; microstructure-informed models incorporating material evolution; and comprehensive studies on applying injection molding simulation tools to *SLS* across diverse geometries and materials.

Recent advances in *SLS* deformation prediction have significantly improved our understanding of the underlying mechanisms and our ability to compensate for these effects. The trend toward integrated approaches that combine simulation, machine learning, and in-process monitoring shows particular promise. However, material-specific challenges and the increasing complexity of *SLS* applications continue to drive the need for more sophisticated prediction methodologies.

Our current research addresses a specific gap in the literature by establishing quantitative relationships between deformation predictions from injection molding

simulation software and actual *SLS* outcomes, providing a practical pathway for utilizing existing commercial tools in *SLS* applications.

3. Prediction process in Solidworks plastics

The prediction of residual deformations was conducted using the Solidworks Plastics software package. An example of the system's screen form with the researched product model is presented in Fig. 1.

The workflow begins with the original *CAD* model and progresses through simulation in SOLIDWORKS Plastics, where thermal and mechanical analyses are performed to predict deformation patterns. The visualization of predicted deformations using the *HSV* color scale provides critical insights into potential problem areas before physical manufacturing begins. This process forms the foundation for applying technological compensating deformations to the initial triangulation models.

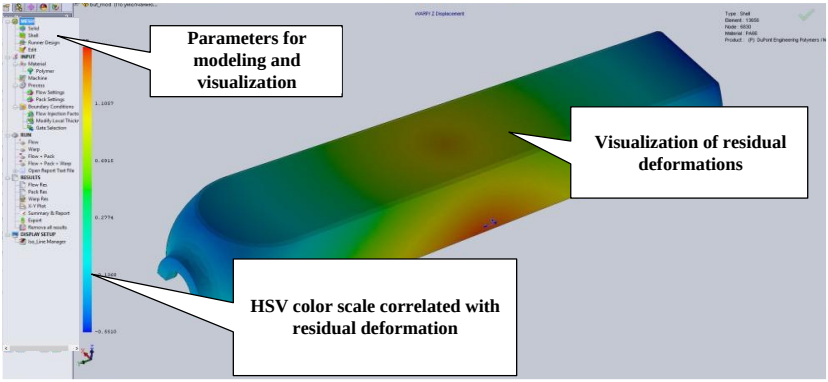

Figure 1 – Workflow for predicting residual deformations in selective laser sintering using Solidworks Plastics

As shown in Fig. 1, the prediction process incorporates several critical elements. The initial verification of the triangulation model ensures surface closure, a prerequisite for accurate simulation. The finite element model construction determines the resolution of the prediction, with element characteristics based on the original triangulation model. Thermal analysis represents the heart of the simulation, where material properties, process parameters (including 230°C processing temperature), and cooling conditions are defined to mimic *SLS* processing conditions. The resulting color visualization (Fig. 1) represents the magnitude of

predicted deformations, with warmer colors (red-yellow) indicating larger deformations and cooler colors (green-blue) showing areas with minimal deformation.

To systematically predict residual deformations in *SLS* manufacturing, a structured workflow was developed as shown in Fig. 2. This process diagram illustrates the sequential steps required for accurate deformation prediction in Solidworks Plastics, from initial model verification through to final visualization. Each step in this workflow has been carefully designed to ensure that the simulation accurately reflects the thermal and mechanical conditions encountered during the *SLS* process, despite the software's original intended application for injection molding simulation.

The process diagram presented in Fig. 2 demonstrates the logical progression of steps necessary for effective deformation prediction. Beginning with triangulation model verification ensures that the input geometry is suitable for analysis, with a closed surface that properly represents the intended part. This is followed by the construction of a finite element model with appropriate mesh density to capture geometric features while maintaining computational efficiency.

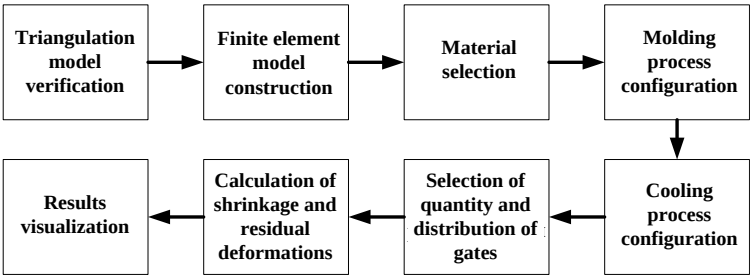

Figure 2 – Schematic diagram of the residual deformation prediction process in Solidworks Plastics

The material selection step is particularly critical, as it establishes the thermo-mechanical properties that govern deformation behavior. For this research, polyamide 66 (*ZYTEL ST801L NC010*) was selected due to its similar characteristics to the *Duraform PA* powder used in *SLS* processing. The process parameters are then defined to simulate *SLS* conditions, including a 230°C processing temperature and appropriate cooling conditions.

The final steps involve the calculation of shrinkage and residual deformations, followed by visualization of the results. This systematic approach enables engineers to predict potential deformation issues before physical prototyping, significantly

reducing development time and material waste. Importantly, the established correlation coefficient allows for reliable translation between the simulation predictions and actual *SLS* manufacturing outcomes, making this workflow a valuable tool for industrial applications.

Upon completion of the shrinkage and residual deformation calculations, color visualization of the predicted residual deformations was performed using the *HSV* color scale (Fig. 3).

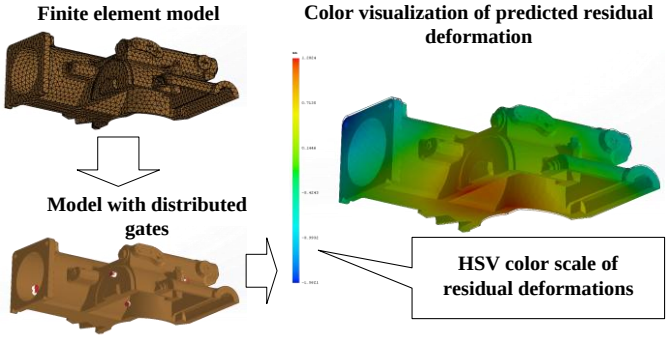

Figure 3 - Visualization of the main stages in residual deformation prediction

The visualization of predicted residual deformations represents a critical component in the analysis process. Fig. 3 illustrates the transformation from a finite element model through to the final visualization of predicted deformations. This visualization process is essential for identifying critical areas prone to dimensional inaccuracies during *SLS* manufacturing, allowing for targeted compensation strategies to be implemented. The visual representation using the *HSV* color scale provides an intuitive understanding of deformation magnitude and distribution across complex geometries.

As demonstrated in Fig. 3, the process begins with the creation of a detailed finite element model that accurately represents the part geometry. This model is then prepared for thermal-mechanical analysis through the strategic placement of gates, which serve as heat input sources simulating the thermal conditions during the *SLS* process. For this study, ten gates were positioned equidistantly to ensure uniform heat distribution, mimicking the gradual cooling experienced in *SLS* manufacturing. This approach eliminates the need for a dedicated cooling system in the simulation, better replicating the *SLS* thermal environment. The final visualization (Fig. 3) employs an *HSV* color scale to represent the magnitude of predicted deformations across the part. Red and yellow regions indicate areas with maximum deformation,

while green and blue denote areas with minimal deformation. This color mapping allows designers and engineers to quickly identify problematic features that may require geometric compensation prior to manufacturing.

The ability to visualize deformation patterns before physical production represents a significant advantage, enabling informed decisions about design modifications or compensation strategies.

4. Results and Validation

To validate the hypothesis that injection molding simulation can be adapted for *SLS* deformation prediction, a correlation analysis was conducted between simulated and measured deformations. Fig. 4 presents the empirical relationship between predicted deflection values from SOLIDWORKS Plastics (ΔF_p) and actual measured deflections in *SLS*-manufactured parts (ΔF_c). This relationship is fundamental to the practical application of the proposed methodology, as it establishes a quantitative basis for translating simulation results to expected real-world outcomes.

The scatter plot in Fig. 4 demonstrates a strong positive correlation between the predicted deformation values from SOLIDWORKS Plastics (Δ_{Fp}) and the experimentally measured deformations in *SLS*-manufactured parts (Δ_{Fc}). The data points, representing 12 different test geometries, show a consistent linear trend that can be expressed by the equation $\Delta_{Fc} = k_p \cdot \Delta_{Fp}$. Through least squares regression analysis, the coefficient k_p was determined to be 1.28±0.08 at a significance level of 0.05.

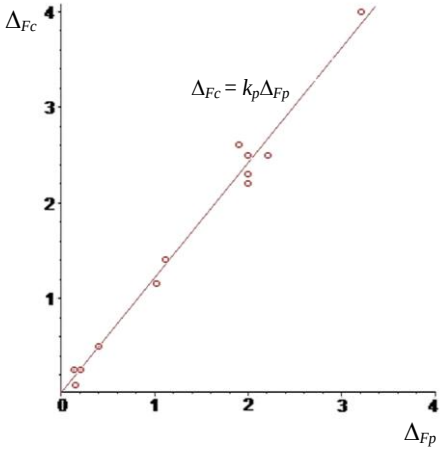

Figure 4 - Correlation between experimental deflection values (Δ_{Fp}) measured on SLS-manufactured parts and predicted deflection values (Δ_{Fp}) from SOLIDWORKS Plastics simulation

This correlation coefficient is particularly significant as it provides a simple yet effective means to convert simulation predictions into practical expectations for actual *SLS* manufacturing outcomes. The value of $k_p > 1$ indicates that real *SLS* parts consistently exhibit larger deformations than those predicted by SOLIDWORKS Plastics, likely due to differences in material behavior and processing conditions between injection molding (for which the software was designed) and selective laser sintering.

The strong linear relationship observed across various geometries validates the core hypothesis of this research: that with appropriate scaling, existing injection molding simulation tools can be effectively repurposed for *SLS* deformation prediction. This finding has significant practical implications, as it enables manufacturers to leverage widely available simulation software for *SLS* applications without requiring specialized and often more expensive dedicated *SLS* simulation tools. The established correlation coefficient serves as a reliable conversion factor that bridges the gap between these two manufacturing domains.

5. Discussion of Results

The experimental investigation conducted in this study has provided significant insights into the prediction and compensation of residual deformations in selective laser sintering manufacturing. Several key findings emerge from the analysis of the results.

The strong linear correlation between predicted deformations from SOLIDWORKS Plastics (ΔF_p) and measured deformations in *SLS*-manufactured parts (ΔF_c) confirms the validity of using injection molding simulation software for *SLS* applications. This cross-technology approach leverages the established capabilities of widely available simulation tools while addressing the specific deformation challenges in *SLS* manufacturing. The consistency of the correlation across 12 different test geometries, with varying complexities and feature characteristics, suggests that this approach is robust and applicable to a range of industrial components.

The determined correlation coefficient ($k_p = 1.28 \pm 0.08$) represents a critical advancement in bridging theoretical predictions and practical outcomes. This coefficient encapsulates the systematic differences between the two manufacturing processes, including variations in material behavior, thermal gradients, and

solidification mechanisms. The value of $k_p > 1$ indicates that *SLS* components consistently experience approximately 28% greater deformation than what the injection molding simulation predicts. This quantitative relationship allows for reliable translation between simulation results and expected manufacturing outcomes.

The simulation approach using distributed heat sources (gates) and the absence of a dedicated cooling system successfully replicates the gradual cooling conditions characteristic of the *SLS* process. The thermal simulation results, visualized through the *HSV* color scale, accurately predict the patterns of deformation, even if the absolute magnitudes require scaling through the correlation coefficient. This indicates that the fundamental thermal mechanisms driving deformation in both injection molding and *SLS* have sufficient similarities to enable effective cross-process prediction.

Based on the established correlation, technological compensating deformations can be systematically applied to original triangulation models with confidence. By applying inverse transformations scaled by the factor k_p, manufacturers can proactively mitigate anticipated deformations. This predictive compensation strategy eliminates the need for multiple iterative manufacturing attempts to achieve dimensional accuracy, thereby reducing material waste, energy consumption, and production time.

While the approach has demonstrated high efficacy across the tested geometries, certain limitations must be acknowledged. The correlation coefficient is specific to the material pair used in this study (ZYTEL ST 801 L NC010 in simulation and Duraform PA in *SLS* manufacturing) and would need recalibration for different materials. Additionally, extremely complex geometries with very thin features or sharp transitions may exhibit non-linear deformation behaviors that require more sophisticated modeling approaches.

Compared to developing dedicated *SLS* simulation software or conducting extensive empirical testing, the proposed approach offers significant advantages in terms of accessibility, computational efficiency, and integration with existing design workflows. The method reduces the barrier to entry for predicting *SLS* deformations, making high-quality additive manufacturing more accessible to a broader range of industrial applications where dimensional accuracy is critical.

This analysis demonstrates that adapted injection molding simulation offers a viable and effective pathway for predicting and compensating for residual deformations in *SLS* manufacturing. The established correlation coefficient provides the necessary bridge between simulation and reality, enabling manufacturers to leverage existing software tools to enhance the dimensional accuracy of *SLS*-produced components.

6. Conclusions

The hypothesis regarding the possibility of predicting residual deformations in products manufactured by selective laser sintering using approaches developed for plastic injection molding has been validated. The established correlation between Solidworks Plastics predictions and actual *SLS* deformations demonstrates that existing simulation tools can be effectively adapted for *SLS* applications.

The proposed methodology for predicting residual deformations includes triangulation model verification, finite element model creation, material selection, process parameter definition, and simulation of deformations using distributed heat sources to replicate *SLS* thermal conditions.

The methodology enables the determination of critical parameters for technological compensating deformations, including the deflection arrow and the relative displacement of the deformation curvature center, which can be applied to original *CAD* models to improve dimensional accuracy.

The approach offers significant practical advantages for industry, including:

- utilization of widely available simulation software instead of specialized SLS deformation prediction tools;
- reduction in material waste and production time by decreasing the need for iterative physical prototyping;
- improved dimensional accuracy of final *SLS*-manufactured components.

This research addresses a significant gap in the field of additive manufacturing by providing a practical, accessible approach to predicting and compensating for residual deformations in *SLS*-manufactured parts. The established correlation coefficient serves as a valuable bridge between injection molding simulation and *SLS* manufacturing reality, enabling more accurate production of complex components with reduced trial-and-error iterations.

Future work should focus on extending this approach to a wider range of materials, investigating more complex geometries, and potentially integrating the methodology with topology optimization to develop designs inherently resistant to deformation during the *SLS* process.

References: 1. *Breuninger, J., Becker, R., Wolf, A., Rommel, S., Verl, A.* Generative Fertigung mit Kunststoffen: Konzeption und Konstruktion für Selektives Lasersintern. Springer-Verlag, 2012. 267 p. **2.** *Garashchenko Y.M.* Udoskonalennya tekhnolohichnoyi pidhotovky adytyvnoho vyrobnytstva skladnykh vyrobiv: monohrafiya. Kharkiv: NTU «KHPI». 2023. 388 p. **3.** *Garashchenko, Y., Fedorovich, V., Poharskyi, A., Kozakova, N., Riazanova-Khytrovska, N.* Increasing the Accuracy of Part Obtained by Selective Laser Sintering by Shrinkage Compensation. In: Tonkonogyi, V., Ivanov, V., Trojanowska, J., Oborskyi, G. (eds) Advanced Manufacturing Processes VI. Interpartner 2024. Lecture Notes in Mechanical Engineering. Springer, Cham. 2025. pp. 166–177. https://doi.org/10.1007/978-3-031-82746-4_15. **4.** *Impey, S.; Saxena, P.; Salonitis, K.* Selective Laser Sintering Induced Residual Stresses:

Precision Measurement and Prediction. J. Manuf. Mater. Process. 2021, 5, 101. https://doi.org/10.3390/jmmp5030101. **5.** *Tian, X., Peng, G., Yan, M., He, S., Yao, R.* Process prediction of selective laser sintering based on heat transfer analysis for polyamide composite powders. International Journal of Heat and Mass Transfer, 120, 2018. pp. 379–386. https://doi.org/10.1016/j.ijheatmasstransfer.2017.12.045. **6.** *Sahoo, S.* Prediction of residual stress and deformation of build part with variation of hatch spacing in direct metal laser sintering of AlSi10Mg built part: Thermo-mechanical modeling. Journal of Laser Applications, 33(3). 2021. https://doi.org/10.2351/7.0000393. **7.** *Chen, Q., Liang, X., Hayduke, D., Liu, J., Cheng, L., Oskin, J., Whitmore, R. and To, A.C.* An inherent strain based multiscale modeling framework for simulating part-scale residual deformation for direct metal laser sintering. Additive Manufacturing, 28, 2019. pp. 406–418. https://doi.org/10.1016/j.addma.2019.05.021. **8.** *Li, C., Fu, C.H., Guo, Y.B. and Fang, F.Z.,* Fast prediction and validation of part distortion in selective laser melting. Procedia Manufacturing, 1, 2015. pp.355–365. https://doi.org/10.1016/j.promfg.2015.09.042. **9.** *Ha, S., Ransikarbum, K., Han, H., Kwon, D., Kim, H. and Kim, N.,* A dimensional compensation algorithm for vertical bending deformation of 3D printed parts in selective laser sintering. Rapid Prototyping Journal, 24(6), 2018. pp. 955–963. https://doi.org/10.1108/RPJ-12-2016-0202. **10.** *Afazov, S., Denmark, W.A., Toralles, B.L., Holloway, A. and Yaghi, A.,* 2017. Distortion prediction and compensation in selective laser melting. Additive Manufacturing, 17, pp. 15–22. https://doi.org/10.1016/j.addma.2017.07.005. **11.** *Dong, W., Paudel, B.J., Deng, H., Garner, S. and To, A.C.* Data-driven distortion compensation for laser powder bed fusion process using Gaussian process regression and inherent strain method. Materials & Design, 243, 2024. p. 113063. https://doi.org/10.1016/j.matdes.2024.113063. **12**. *Ali, H., Ghadbeigi, H., Mumtaz, K.* Processing Parameter Effects on Residual Stress and Mechanical Properties of Selective Laser Melted Ti6Al4V. Journal of materials engineering and performance. 27, 2018. 4059–4068. https://doi.org/10.1007/s11665-018-3477-5. **13.** *Azam, M.U., Belyamani, I., Schiffer, A., Kumar, S. and Askar, K.* Progress in selective laser sintering of multifunctional polymer composites for strain-and self-sensing applications. Journal of Materials Research and Technology. 2024. https://doi.org/10.1016/j.jmrt.2024.06.024.

Ярослав Гаращенко, Андрій Погарський, Володимир Федорович, Олена Гаращенко, Андрій Малиняк, Харків, Україна

ПРОГНОЗУВАННЯ ЗАЛИШКОВИХ ДЕФОРМАЦІЙ ВИРОБІВ, ВИГОТОВЛЕНИХ ЗА ДОПОМОГОЮ СЕЛЕКТИВНОГО ЛАЗЕРНОГО СПІКАННЯ

Анотація. *Дослідження розглядає критичну проблему прогнозування залишкових деформацій у промислових виробах, виготовлених за допомогою технології селективного лазерного спікання (SLS). Залишкові деформації є одним з основних факторів, що призводять до геометричних неточностей у деталях, виготовлених за допомогою SLS, безпосередньо впливаючи на їх функціональні характеристики та точність розмірів. Дослідження пропонує та підтверджує нову гіпотезу про те, що існуючі моделі прогнозування, розроблені для лиття пластмас під тиском, можуть бути ефективно адаптовані для застосування SLS за допомогою відповідних коефіцієнтів перетворення. Враховуючи відсутність спеціалізованих інструментів для прогнозування деформації SLS на сучасному ринку, цей підхід використовує відомі можливості програмного забезпечення SOLIDWORKS Plastics як альтернативне рішення. Методологія включає створення моделей скінченних елементів тестових компонентів, визначення*

властивостей матеріалу, подібних до порошків SLS, та моделювання теплових умов, що імітують процес SLS. Завдяки порівняльному аналізу дванадцяти різних конструкцій виробів було встановлено значну кореляцію між прогнозованими деформаціями та фактично виміряними деформаціями. Цей коефіцієнт забезпечує надійне перетворення між результатами моделювання та фактичними результатами SLS. Результати дослідження демонструють, що технологічні компенсуючі деформації можна ефективно розраховувати та застосовувати до оригінальних моделей тріангуляції, що суттєво зменшує геометричні відхилення в кінцевих виробах. Дослідження усуває розрив між усталеними методами моделювання лиття під тиском та адитивного виробництва, забезпечуючи практичний підхід до підвищення точності розмірів без необхідності спеціалізованого програмного забезпечення для прогнозування деформації виробів одержаних методом SLS. Дослідження виконувались на кафедрі «Інтегрованих технологій машинобудування» імені М.Ф. Семка НТУ «ХПІ».

Ключові слова: *технологічна підготовка; селективне лазерне спікання; залишкова деформація; моделі тріангуляції; технологічні компенсуючі деформації.*

UDC 621.923.74 **doi: 10.20998/2078-7405.2025.102.07**

CARBON DIOXIDE EMISSIONS AND SURFACE ROUGHNESS ANALYSIS DURING DIAMOND BURNISHING

Szilárd **Smolnicki** [0009-0006-1535-5295], Gyula **Varga** [0000-0003-3810-2881]

University of Miskolc, 3515 Miskolc-Egyetemváros, Hungary
gyulavarga@uni-miskolc.hu

Received: 25 May 2025 / Revised: 02 June 2025 / Accepted: 09 June 2025 / Published: 20 June 2025

Abstract. *Carbon emissions are one of the most pressing environmental problems of our time. CO_2 emitted by human activities, especially industry, transport and energy production, is a major contributor to the gradual warming of the Earth's atmosphere. The aim of my research is to investigate the relationship between carbon dioxide emissions and surface roughness by varying different technological parameters during diamond burnishing.*
In the first chapter of this paper, we will review the current state of the art and literature on carbon dioxide emissions and then, based on a chosen methodology, we will show how carbon dioxide emissions from diamond polishing can be quantified. Following the calculation, we will present the technological parameters used for the machining, the test pieces on which we measured surface roughness after diamond burnishing, and some additional calculations needed to evaluate the data. In the main part of the research, we will evaluate the calculated data using 2D and 3D surface roughness metrics, with a special focus on the characteristics of the Abbott-Firestone curve.
Keywords: *energy efficiency; sustainable development; slide diamond burnishing; surface finish.*

1. Examination of carbon dioxide emissions

Carbon dioxide emissions are among the most pressing environmental issues of our time. Human activities – particularly in industry, transportation, and energy production – release large amounts of CO_2, significantly contributing to the gradual warming of Earth's atmosphere. While carbon dioxide (CO_2) is responsible for climate change, other substances such as carbon monoxide (CO), nitrogen oxides (NOX), and unburned hydrocarbons can be considered harmful to human health [1]. Although CO_2 is not toxic to human health on its own, its long-term accumulation poses a serious threat to the planet's climate. In the field of mechanical processing, carbon dioxide emissions can also be significant. Therefore, it is important to identify optimal processes with the right process parameters to help reduce CO_2 emissions [2].

According to the report of the International Energy Agency [3], we can observe how the increase in carbon dioxide emissions has changed over decades. The last period when emissions did not grow was after the Great Depression and

World War II. Since then, emissions have been increasing – sometimes more, sometimes less. It is also evident that major events such as the dissolution of the Soviet Union or China's rapid development can influence the emission rate: the former slowed it down, the latter accelerated it. Furthermore, the use of renewable energy sources cannot be ignored, as they reduce hydrocarbon use, and this impact is shown in the final column of Figure 1. It is evident that low carbon manufacturing has become a key expectation in industry. Therefore, quantitative analysis of energy consumption and CO_2 emissions in manufacturing processes is essential. This is what leads us from the scientific understanding of efficient production to industrial implementation [4]. A review of the literature reveals numerous efforts aimed at achieving this goal. A few of these are outlined below.

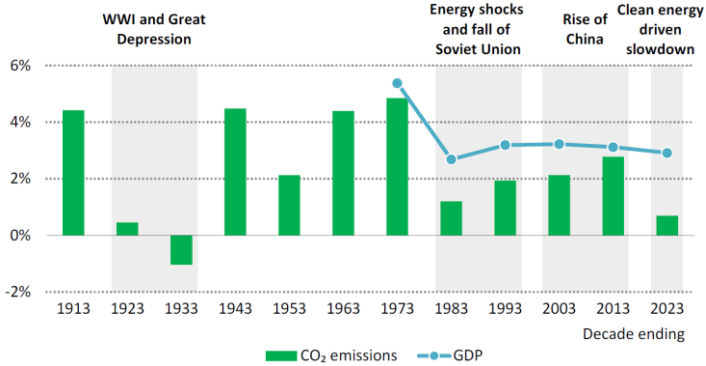

Figure 1. Global CO_2 emissions and GDP growth rate by decade [3]

Based on the operation sequence of machining, the energy consumption of machine tools can be divided into three modes—idle mode, running mode, and production mode. Various studies have focused on these distinct modes [5]. Others have found that reducing idle time and downtime helps minimize energy consumption [6]. A method has also been developed to predict total energy consumption for a specific turning operation on a machine tool [7]. Energy minimization has been analyzed using discrete statistical formulas as well [8].

Moreover, some methods directly link the electrical energy used during manufacturing to the CO_2 emissions generated during the process [9]. Others have focused on production planning problems in highly automated manufacturing systems, considering multiple process plans with different energy requirements [10]. Approaches from a mathematical standpoint have also been explored, including programming models that focus on process-level scheduling to reduce energy consumption and CO_2 emissions [11]. Research has also examined the relationship between carbon footprint and the manufacturing industry, analyzing its

environmental impact [12]. An integrated concept has been published that aims to promote energy efficiency at various levels within manufacturing companies, taking into account the interdependence of all technical processes [13]. An analytical method has also been proposed to quantify the CO_2 emissions of a *CNC*-based machining system, while breaking down the processes that contribute to the system's total CO_2 emissions [14].

As seen, many approaches exist to quantify carbon dioxide emissions. In this study, a model [2] is selected for evaluating CO_2 emissions, which considers the average emissions per kilowatt-hour and the technological parameters of the machining process. In the case of diamond burnishing, these parameters include the burnishing force, burnishing speed, and feed rate.

Carbon dioxide emissions can be calculated using Equation (1):

$$CE = CE_{el} \cdot W \ [g] \tag{1}$$

Where "CE_{el}" is the carbon dioxide emission factor for electricity, which can be obtained from the EMBER database [15], available by country and year. Figure 2 shows the data filtered for Hungary, starting from the 1990s.

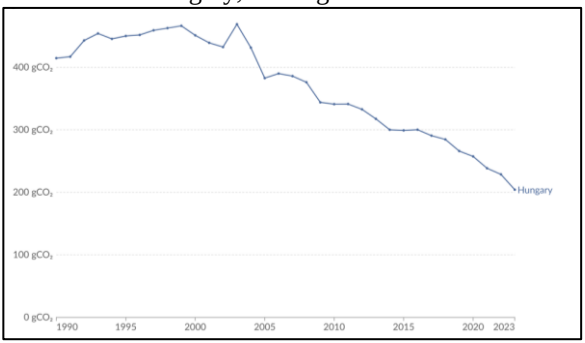

Figure 2. CO_2 emission factor of electricity in Hungary [16]

For the current calculation, the value of the carbon dioxide emission factor is:

$$CE_{el} = 229 \frac{g}{kWh}$$

In the formula, "W " represents the energy consumption of the machining process, which can be calculated using Equation (2):

$$W = P \cdot t \ [kWh] \tag{2}$$

Here, "P" is the power requirement of the machining process, calculated using Equation (3), and "t" is the machining time, which can be calculated using Equation (4):

$$P = F \cdot v_v \ \left[W = \frac{N \cdot m}{s}\right] \tag{3}$$

$$t = \frac{L}{v_f} = \frac{L}{f \cdot n}\ [s] \quad (4)$$

The burnishing speed required for power calculation can be determined using Equation (5), where "n" is the rotational speed and "d" is the diameter of the test piece. In the time formula, "n" again refers to spindle speed, "L" is the length of the machining on the test piece, and "f" is the feed rate used in the process:

$$v_v = d \cdot \pi \cdot n\ \left[\frac{m}{s}\right] \quad (5)$$

The burnishing force required for the power calculation can be computed using Equation (6):

$$F = \mu \cdot F_v \quad (6)$$

Here, "μ" is the coefficient of friction, which in the case of a diamond-steel contact with cooling-lubricating fluid is μ = 0.1 [18]. Therefore, the subsequent calculations use the burnishing force multiplied by the coefficient of friction.

This burnishing force calculation is necessary because the force set as a technological parameter is passive in terms of cutting direction, while the burnishing speed in Equation (5) points in the direction of the main cutting force (as this is the cutting speed). Therefore, the set burnishing force must be converted using the friction force relationship. The spatial relationship of the forces is illustrated in Figure 3. In this case, the passive force, which can be directly set as a technological parameter during machining, is considered the normal force (denoted F_n in the figure), while the main cutting force used in the calculations is the frictional force (denoted F_s). Their relationship is shown in Equation (7), which is structurally identical to Equation (6), differing only in the notation of the forces:

$$F_s = \mu \cdot F_n \quad (7)$$

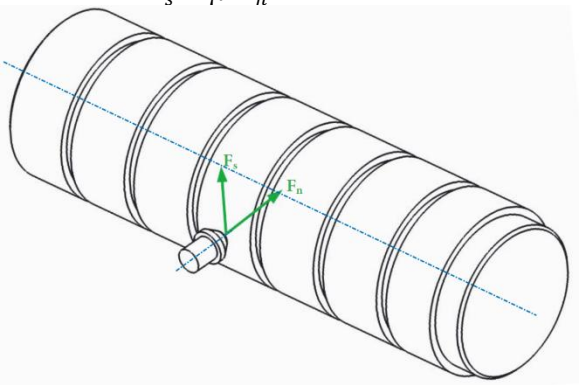

Figure 3. Spatial relationship of actual and calculated burnishing forces

Thus, for the calculation of CO_2 emissions, only the defined technological parameters, the dimensions of the test piece, and the CO_2 emission factor are needed.

2. Surface machining and roughness measurement

To perform calculations and draw conclusions with an adequate level of reliability, enough experiments must be carried out by combining technological parameters. The following values were selected for feed rate, spindle speed, and burnishing force:

$$f_1 = 0.05\frac{mm}{rev};\ f_2 = 0.1\frac{mm}{rev}$$

$$n_1 = 265\frac{1}{min};\ n_2 = 375\frac{1}{min}$$

The product of the number of different parameters is 2·2·6=24, meaning that 24 different surface sections need to be created to measure the surface roughness after diamond burnishing. For this purpose, four test specimens were manufactured. After preliminary turning, each specimen was prepared with six cylindrical surfaces suitable for diamond burnishing. These were produced in the workshop of the Institute of Manufacturing Science at the University of Miskolc. The parameter combinations are summarized in Table 1, grouped by specimen and numbered in groups of six.

Table 1. Technological parameters of the diamond burnishing process

Serial Nr.	$\boldsymbol{f\ \left[\frac{mm}{rev}\right]}$	$\boldsymbol{n\ \left[\frac{1}{min}\right]}$	$\boldsymbol{F_v\ (N)}$
1-1	0.05	265	120
1-2	0.05	265	100
1-3	0.05	265	80
1-4	0.05	265	60
1-5	0.05	265	40
1-6	0.05	265	20
2-1	0.1	265	120
2-2	0.1	265	100
2-3	0.1	265	80
2-4	0.1	265	60
2-5	0.1	265	40
2-6	0.1	265	20
3-1	0.05	375	120
3-2	0.05	375	100
3-3	0.05	375	80
3-4	0.05	375	60
3-5	0.05	375	40
3-6	0.05	375	20
4-1	0.1	375	120
4-2	0.1	375	100

4-3	0.1	375	80
4-4	0.1	375	60
4-5	0.1	375	40
4-6	0.1	375	20

The test specimens were made from grade 1.4307 austenitic stainless chromium-nickel steel, whose material properties are as follows: yield strength $R_{p0,2} \geq 210\ MPa$, tensile strength $R_m = 520 - 700\ MPa$, elongation at break $A \geq 45\%$, density $\rho = 7.9\ kg/dm^3$, and hardness $160 - 190\ HB$.

In terms of chemical composition, it consists of 66.8–71.3% iron, ≤0.03% carbon, 1% silicon, 2% manganese, 0.045% phosphorus, 0.015% sulfur, ≤0.11% nitrogen, 17.5–19.5% chromium, and 8–10.5% nickel.

The technical drawing of the test specimen is shown in Figure 4.

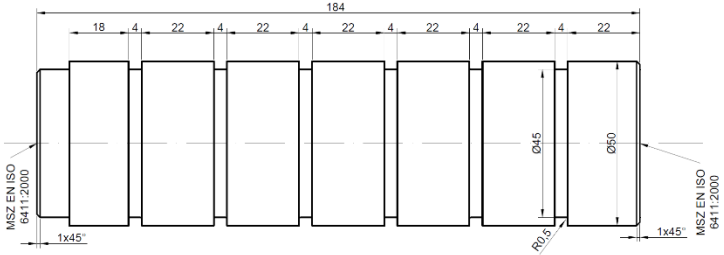

Figure 4. Technical drawing of the test specimen

EU- 400-01 type lathe, and the process conditions are illustrated in Figure 5.

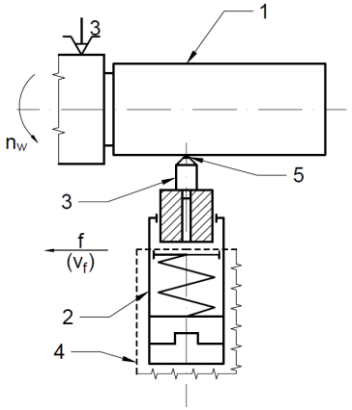

Figure 5. Schematic of the diamond burnishing process [17]

During the research, surface roughness was analysed using several indicators, including 2*D* roughness parameters [17], 3*D* surface roughness values [19], and the

2*D* and 3*D* characteristics of the Abbott-Firestone curves [20], which have already been described in detail in my previous studies.

Surface roughness measurements were carried out using an AltiSurf 520 roughness measurement device, and the results were analysed using the AltiMap software provided with the instrument. Both are in the metrology laboratory of the Institute of Manufacturing Science at the University of Miskolc.

To analyse the characteristics of the Abbott-Firestone curves, we used K-coefficients [20, 21], calculated using Equations (8–13). These equations provide percentage values representing the distribution of the surface profile zones, offering a meaningful comparison of their relevance. For example, Equation (8) shows the proportion of the core roughness within the total 2D roughness profile:

$$K_{Rk} = \frac{R_k}{R_k + R_{pk} + R_{vk}} \quad (8) \qquad K_{Rpk} = \frac{R_{pk}}{R_k + R_{pk} + R_{vk}} \quad (9)$$

$$K_{Rvk} = \frac{R_{vk}}{R_k + R_{pk} + R_{vk}} \quad (10) \qquad K_{Sk} = \frac{S_k}{S_k + S_{pk} + S_{vk}} \quad (11)$$

$$K_{Spk} = \frac{S_{pk}}{S_k + S_{pk} + S_{vk}} \quad (12) \qquad K_{Svk} = \frac{S_{vk}}{S_k + S_{pk} + S_{vk}} \quad (13)$$

3. Evaluation of the research results

To evaluate the results, we first present the calculated values, which are summarized in Table 2. The table lists the technological parameters – feed rate and burnishing force – alongside the calculated burnishing speed, power, and the carbon dioxide emissions associated with each machining operation.

Table 2. Calculated data for diamond burnishing

Serial Nr.	$f\ \left[\frac{mm}{rev}\right]$	$v_v\ \left[\frac{m}{s}\right]$	$n\ \left[\frac{1}{min}\right]$	$F_v\ (N)$	$P\ (W)$	$CE\ (g)$
1-1	0.05	0.6938	265	120	8.33	189.93
1-2	0.05	0.6938	265	100	6.94	158.27
1-3	0.05	0.6938	265	80	5.55	126.62
1-4	0.05	0.6938	265	60	4.16	94.96
1-5	0.05	0.6938	265	40	2.78	63.31
1-6	0.05	0.6938	265	20	1.39	31.65
2-1	0.1	0.6938	265	120	8.33	94.96
2-2	0.1	0.6938	265	100	6.94	79.14
2-3	0.1	0.6938	265	80	5.55	63.31
2-4	0.1	0.6938	265	60	4.16	47.48
2-5	0.1	0.6938	265	40	2.78	31.65
2-6	0.1	0.6938	265	20	1.39	15.83
3-1	0.05	0.9817	375	120	11.78	189.93
3-2	0.05	0.9817	375	100	9.82	158.27

3-3	0.05	0.9817	375	80	7.85	126.62
3-4	0.05	0.9817	375	60	5.89	94.96
3-5	0.05	0.9817	375	40	3.93	63.31
3-6	0.05	0.9817	375	20	1.96	31.65
4-1	0.1	0.9817	375	120	11.78	94.96
4-2	0.1	0.9817	375	100	9.82	79.14
4-3	0.1	0.9817	375	80	7.85	63.31
4-4	0.1	0.9817	375	60	5.89	47.48
4-5	0.1	0.9817	375	40	3.93	31.65
4-6	0.1	0.9817	375	20	1.96	15.83

We analysed the measured surface roughness data using diagrams. The 2D surface roughness metrics are shown in Figure 6. In subfigure a) the average roughness, in b) the root mean square roughness, in c) the ten-point mean roughness, and in d) the maximum roughness depth is plotted on the vertical axis, with carbon dioxide emissions on the horizontal axis.

We used different colour codes to represent combinations of feed rate and burnishing speed. Since two types of feed rates and spindle speeds were combined, four parameter combinations were examined. We fitted second-degree polynomials to the data points, and the reliability of these trendlines is indicated by the R^2 values shown in the top right corner of each graph.

To support the analysis, we also added data labels. Each point shows the applied burnishing force and a calculated value – CE(%) – which expresses the relative reduction in carbon dioxide emissions. The formula for CE(%) is given by Equation (12):

$$CE(\%) = \left(1 - \frac{CE_{calculated}}{CE_{max}}\right) 100\ [\%] \qquad (12)$$

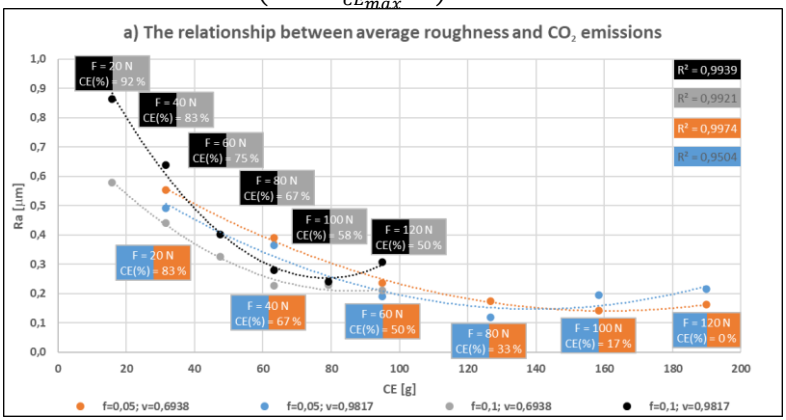

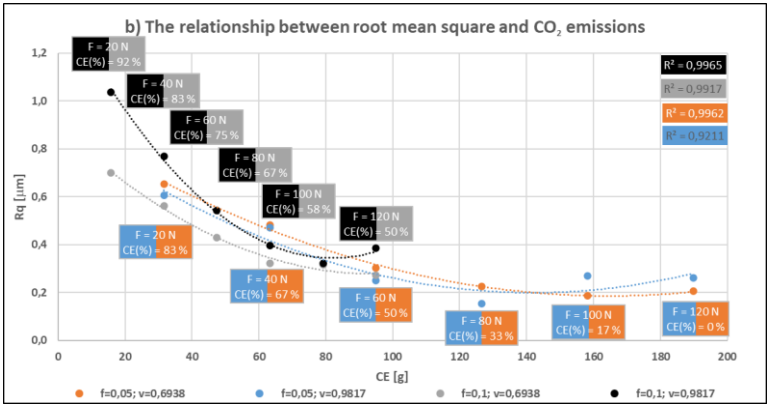
b) The relationship between root mean square and CO2 emissions
Rq [µm]
CE [g]
F = 20 N CE(%) = 92 %
F = 40 N CE(%) = 83 %
F = 60 N CE(%) = 75 %
F = 80 N CE(%) = 67 %
F = 100 N CE(%) = 58 %
F = 120 N CE(%) = 50 %
F = 20 N CE(%) = 83 %
F = 40 N CE(%) = 67 %
F = 60 N CE(%) = 50 %
F = 80 N CE(%) = 33 %
F = 100 N CE(%) = 17 %
F = 120 N CE(%) = 0 %
R² = 0,9965
R² = 0,9917
R² = 0,9962
R² = 0,9211
f=0,05; v=0,6938
f=0,05; v=0,9817
f=0,1; v=0,6938
f=0,1; v=0,9817

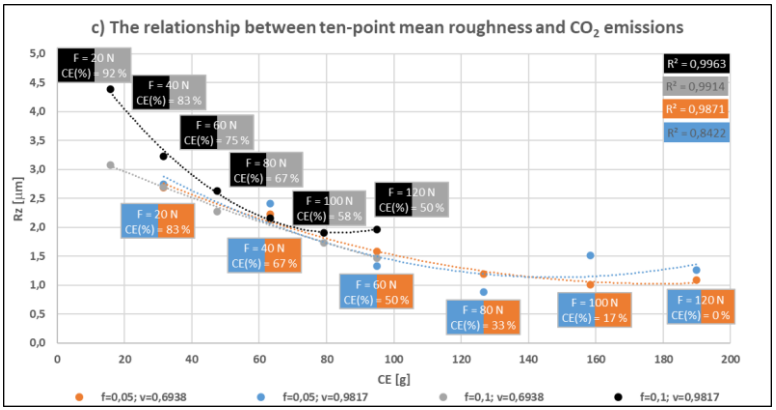
c) The relationship between ten-point mean roughness and CO2 emissions
Rz [µm]
CE [g]
F = 20 N CE(%) = 92 %
F = 40 N CE(%) = 83 %
F = 60 N CE(%) = 75 %
F = 80 N CE(%) = 67 %
F = 100 N CE(%) = 58 %
F = 120 N CE(%) = 50 %
F = 20 N CE(%) = 83 %
F = 40 N CE(%) = 67 %
F = 60 N CE(%) = 50 %
F = 80 N CE(%) = 33 %
F = 100 N CE(%) = 17 %
F = 120 N CE(%) = 0 %
R² = 0,9963
R² = 0,9914
R² = 0,9871
R² = 0,8422
f=0,05; v=0,6938
f=0,05; v=0,9817
f=0,1; v=0,6938
f=0,1; v=0,9817

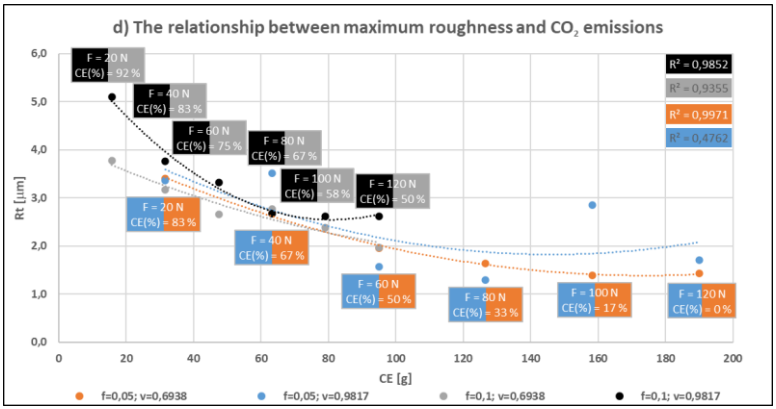
d) The relationship between maximum roughness and CO2 emissions
Rt [µm]
CE [g]
F = 20 N CE(%) = 92 %
F = 40 N CE(%) = 83 %
F = 60 N CE(%) = 75 %
F = 80 N CE(%) = 67 %
F = 100 N CE(%) = 58 %
F = 120 N CE(%) = 50 %
F = 20 N CE(%) = 83 %
F = 40 N CE(%) = 67 %
F = 60 N CE(%) = 50 %
F = 80 N CE(%) = 33 %
F = 100 N CE(%) = 17 %
F = 120 N CE(%) = 0 %
R² = 0,9852
R² = 0,9355
R² = 0,9971
R² = 0,4762
f=0,05; v=0,6938
f=0,05; v=0,9817
f=0,1; v=0,6938
f=0,1; v=0,9817

Figure 6. Relationship between 2D surface roughness parameters and carbon dioxide emissions

To interpret the graphs, we divided the emission value of each data point by the maximum emission value and then subtracted this ratio from one. This yielded the percentage reduction in emissions compared to the worst-case scenario. For the highest emission value (CE=189,93 g), the reduction is naturally 0%. Moving leftward along the horizontal axis – toward zero – the level of emission reduction increases.

Some data points appear in pairs, as similar emission values were observed for different tests with identical feed force ratios. For better clarity, we used gradient shading (black–gray and blue–orange) to distinguish these overlapping points.

Since all subfigures exhibit similar trends, we can confidently state that the conclusions are valid for all types of surface roughness parameters. When using a lower feed rate (represented by orange and blue data points), the trendlines are more elongated, indicating longer processing times and, consequently, higher carbon dioxide emissions. Each of the four trendlines exhibits a parabolic minimum, which appears around 80-100 *N* of burnishing force. Applying forces above this range is not recommended, as it leads to worsening surface quality and increased emissions due to the higher power requirement.

At the same time, surface quality was best achieved using the lower feed rate. However, we found that favourable results can also be achieved with higher feed rates, depending on manufacturing requirements. If ultra-smooth surface quality is not mandatory, adjusting technological parameters may lead to a 60–70% reduction in energy consumption and emissions, while also shortening the machining time. In this way, two common optimization objectives – minimizing energy consumption and machining time – can be achieved simultaneously.

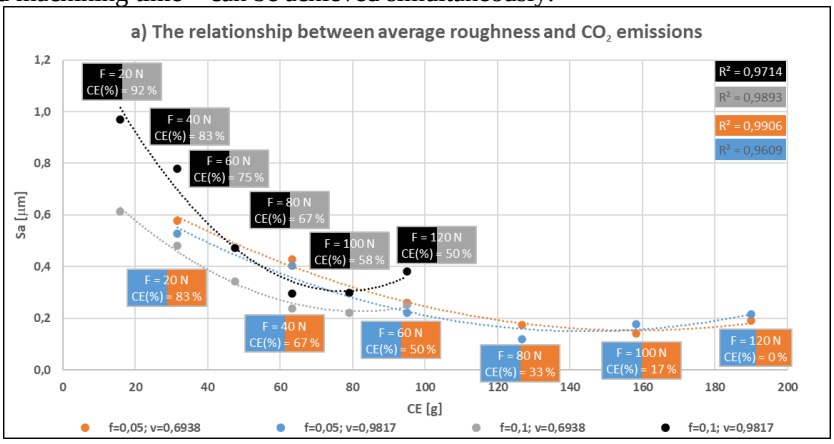

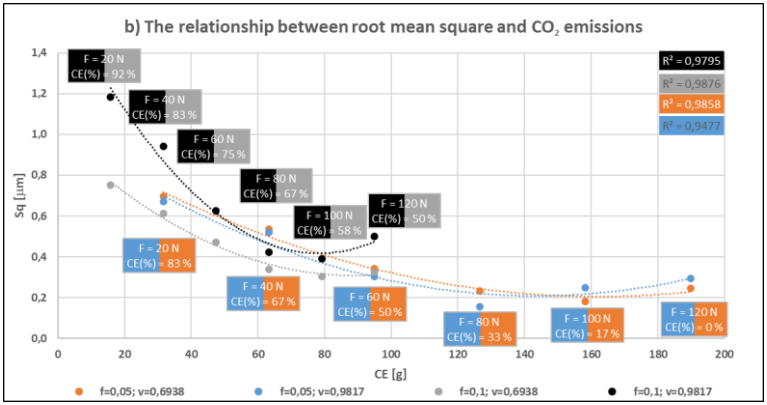
b) The relationship between root mean square and CO2 emissions
Sq [µm]
CE [g]
F = 20 N CE(%) = 92 %
F = 40 N CE(%) = 83 %
F = 60 N CE(%) = 75 %
F = 80 N CE(%) = 67 %
F = 100 N CE(%) = 58 %
F = 120 N CE(%) = 50 %
F = 20 N CE(%) = 83 %
F = 40 N CE(%) = 67 %
F = 60 N CE(%) = 50 %
F = 80 N CE(%) = 33 %
F = 100 N CE(%) = 17 %
F = 120 N CE(%) = 0 %
R² = 0,9795
R² = 0,9876
R² = 0,9858
R² = 0,9477
f=0,05; v=0,6938
f=0,05; v=0,9817
f=0,1; v=0,6938
f=0,1; v=0,9817

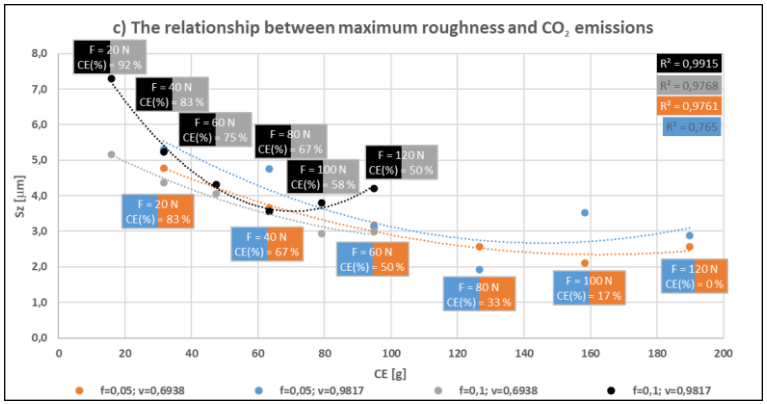
c) The relationship between maximum roughness and CO2 emissions
Sz [µm]
CE [g]
F = 20 N CE(%) = 92 %
F = 40 N CE(%) = 83 %
F = 60 N CE(%) = 75 %
F = 80 N CE(%) = 67 %
F = 100 N CE(%) = 58 %
F = 120 N CE(%) = 50 %
F = 20 N CE(%) = 83 %
F = 40 N CE(%) = 67 %
F = 60 N CE(%) = 50 %
F = 80 N CE(%) = 33 %
F = 100 N CE(%) = 17 %
F = 120 N CE(%) = 0 %
R² = 0,9915
R² = 0,9768
R² = 0,9761
R² = 0,765
f=0,05; v=0,6938
f=0,05; v=0,9817
f=0,1; v=0,6938
f=0,1; v=0,9817

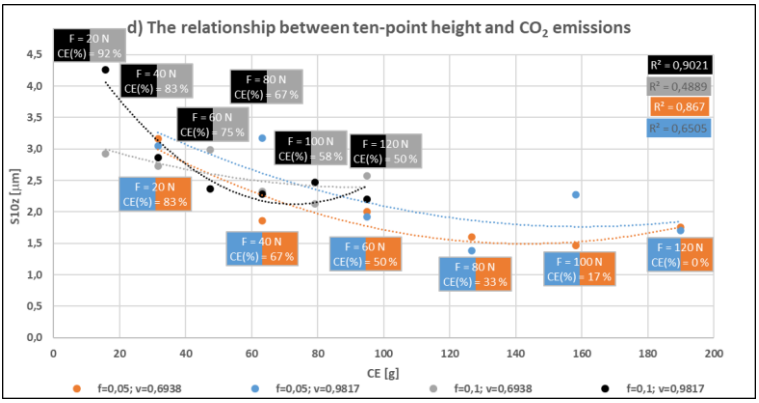
d) The relationship between ten-point height and CO2 emissions
S10z [µm]
CE [g]
F = 20 N CE(%) = 92 %
F = 40 N CE(%) = 83 %
F = 80 N CE(%) = 67 %
F = 60 N CE(%) = 75 %
F = 100 N CE(%) = 58 %
F = 120 N CE(%) = 50 %
F = 20 N CE(%) = 83 %
F = 40 N CE(%) = 67 %
F = 60 N CE(%) = 50 %
F = 80 N CE(%) = 33 %
F = 100 N CE(%) = 17 %
F = 120 N CE(%) = 0 %
R² = 0,9021
R² = 0,4889
R² = 0,867
R² = 0,6505
f=0,05; v=0,6938
f=0,05; v=0,9817
f=0,1; v=0,6938
f=0,1; v=0,9817

Figure 7. Relationship between 3D surface roughness parameters and carbon dioxide emissions

Figure 7 illustrates the 3*D* surface roughness metrics. Subfigure a) presents the arithmetic mean height, b) the root mean square height, c) the maximum height, and d) the ten-point height, all plotted against carbon dioxide emissions. The structure and interpretation of the graphs are consistent with the 2*D* case, and the previously drawn conclusions also apply here.

In the final part of our study, we analysed the material ratio curve parameters – using a different approach due to the unique nature of these metrics. Figure 8 presents these characteristics for both 2*D* and 3*D* profiles, in relation to carbon dioxide emissions.

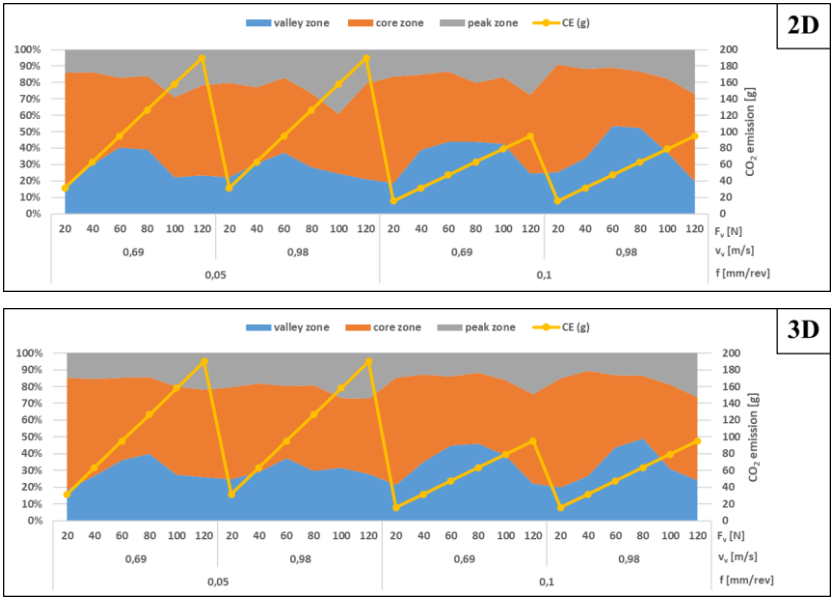

Figure 8. Relationship between material ratio curve parameters and carbon dioxide emissions

Both graphs were prepared using the same methodology. Based on the previously calculated *K* coefficients (according to Equations 8–13), we plotted the relative proportions of the profile zones – for all combinations of feed rate, burnishing speed, and burnishing force. On the secondary axis, we included the carbon dioxide emission value corresponding to each combination. The figures can be interpreted as four separate diagrams representing the four different feed–speed combinations, each with varying burnishing forces.

The goal of diamond burnishing is to reduce the proportion of the peak zone – corresponding to the material that wears off during running-in – to maintain or increase the valley zone, which determines lubricant retention, and to increase or retain the core zone, which bears most of the load.

We observed that the proportion of the peak zone increases at both the lowest and highest applied forces, while the valley zone proportion is at its minimum in these cases – thus these parameter settings should be avoided. With higher feed rates, the maximum valley zone proportion becomes clearly visible, while the peak zone reaches its minimum, indicating optimal tribological performance.

Considering that higher feed rates also proved advantageous in terms of emission reduction and shorter machining time, we recommend using higher feed rates combined with higher burnishing speeds and a burnishing force between 60–80 *N* for optimal results.

4. Summary

First, we reviewed the current state of research related to carbon dioxide emissions and its representation in the literature. Based on a selected method, we presented how CO_2 emissions generated during diamond burnishing can be quantified. Following the calculation, we introduced the technological parameters applied in the machining process, the test specimens on which surface roughness was measured after diamond burnishing, and several additional calculations necessary for data evaluation. Similar trends were observed for both 2*D* and 3*D* surface roughness indicators. It was found that for each combination of feed rate and burnishing speed, a minimum point could be identified on the resulting parabola, beyond which surface roughness no longer decreased. Therefore, applying higher burnishing forces beyond this point is not recommended, as it not only deteriorates surface quality but also increases carbon dioxide emissions due to higher power consumption. Furthermore, we determined that if achieving the best possible surface quality is not a strict requirement, it is worth considering the modification of technological parameters. This can significantly reduce energy consumption and CO_2 emissions – by as much as 60–70% – and even shorten machining times, all while improving the energy and eco-efficiency of the process. In this way, two commonly pursued objective functions – minimization of machining time and energy consumption – can be addressed simultaneously.

Regarding the analysis of the Abbott-Firestone curves, it was demonstrated that the proportion of the peak zone increases at both the lowest and highest burnishing forces, while the valley zone reaches its minimum at these values. Thus, these burnishing force values should be avoided. When using a higher feed rate, a clear maximum of the valley zone was observed, which is optimal for lubricant retention, while the peak zone reached its minimum. Considering that previous

findings also identified higher feed rates as optimal from both CO_2 emission and machining time perspectives, it is recommended to choose this setting in the proposed parameter combination, along with higher burnishing speeds and a burnishing force in the range of 60–80 *N*.

References: **1**. *M. Tóth:* Károsanyag-kibocsátás elemzése szikragyújtású motoron megújuló komponenseket tartalmazó tüzelőanyagok használata esetén motorfékpadi környezetben, in OGÉT 2024 - XXXII. Nemzetközi Gépészeti Konferencia, 2024, pp. 446–451. **2**. *Xin Yao, Wei Yan, Hua Zhang, .Zhigang Jiang, .Shuo Zhu*: A Framework for Carbon Emission Quantification of Mechanical Machining Process Based on IoT and MEFA, IFAC-PapersOnLine, Volume 53, Issue 5, 2020, pp. 25–30, ISSN 2405-8963, https://doi.org/10.1016/j.ifacol.2021.04.079. **3**. *IEA (2024):* CO_2 Emissions in 2023, IEA, Paris https://www.iea.org/reports/co2-emissions-in-2023, Licence: CC BY 4.0. **4**. *Ding, Hui & Guo, Dengyue & Cheng, Kai & Cui, Qi.*: An investigation on quantitative analysis of energy consumption and carbon footprint in the grinding process. Proceedings of the Institution of Mechanical Engineers, Part B: Journal of Engineering Manufacture. 228. 950–956. 10.1177/0954405413508280. **5**. *Dahmus J and Gutowski T.*: An environmental analysis of machining. In: 2004 ASME International Mechanical Engineering Congress (IMECE) and RD&D Expo, Anaheim, CA, 13–19 November 2004, pp.1–10. New York: ASME. **6**. *Tridech S and Cheng K.*: Low carbon manufacturing: characterisation, theoretical models and implementation. Int J of Man Res 2011; 6(2): 110–121. **7.** *Li W and Kara S.*: An empirical model for predicting energy consumption of manufacturing processes: a case of turning process. Proc IMechE, Part B: J Engineering Manufacture 2011; 225(9): 1636–1646. **8**. *Dietmair A and Verl A.*: A generic energy consumption model for decision making and energy efficiency optimisation in manufacturing. Int J Sustain Eng 2009; 2(2): 123–133. **9**. *J. Jeswiet and S. Kara*: Carbon emissions and CES in manufacturing, CIRP Annals—Manufacturing Technology, vol. 57, no. 1, pp. 17–20, 2008. **10.** *Y.-C.Choi and P. Xirouchakis*: Aproduction planning in highly automated manufacturing system considering multiple process plans with different energy requirements, The International Journal of AdvancedManufacturing Technology, vol. 70, no. 5–8, pp. 853–867, 2014. **11**. *K. Fang, N. Uhan, F. Zhao, and J. W. Sutherland*: A newapproach to scheduling in manufacturing for power consumptionand carbon footprint reduction, Journal of ManufacturingSystems, vol. 30, no. 4, pp. 234–240, 2011. **12**. *A. Laurent, S. I. Olsen, and M. Z. Hauschild*: Carbon footprintas environmental performance indicator for the manufacturingindustry, CIRP Annals-Manufacturing Technology, vol. 59, no.1, pp. 37–40, 2010. **13**. *C. Herrmann and S. Thiede*, Process chain simulation tofoster energy efficiency in manufacturing, CIRP Journal of Manufacturing Science and Technology, vol. 1, no. 4, pp. 221–229, 2009. **14**. *C. B. Li, Y. Tang, L. G. Cui, and P. Y. Li*, A quantitative approach to analyze carbon emissions of CNC-basedmachining systems, Journal of Intelligent Manufacturing, 2013. **15.** https://ember-climate.org/data-catalogue/yearly-electricity-data/ (2024. 12. 12.) **16**. *Hannah Ritchie, Pablo Rosado and Max Roser*: "Energy". Data adapted from Ember, Energy Institute. Retrieved from https://ourworldindata.org/grapher/carbon-intensity-electricity (2024. 12. 12.) **17**. *Varga, G., Smolnicki, S., Babič, M., Caesarendra, W.*: Energy Efficiency Analysis When Grinding and Diamond Burnishing of Components, In: Gençyılmaz, M. Güneş; Durakbasa, Numan M. (ed.-s.) Towards Industry 5.0 : Selected Papers from ISPR2022, Cham, Svájc : Springer International Publishing (2023) pp. 378–396. **18**. Coefficient of Friction Equation and Table Chart, Engineers Edge: https://www.engineersedge.com/coeffients_of_friction.htm% 20 (2024. 12. 13.) **19**. *S. Szilárd and V. Gyula*: Energy efficiency study of diamond burnishing using 3*D* surface roughness parameters, in MECHATRONIKA, VÝROBNÁ TECHNIKA, DIGITÁLNY PODNIK: najnovšie úspechy, výzvy, trendy, 2023, pp. 47–57. **20**. *S. Smolnicki and G. Varga*: Analysis of the Abbott-Firestone curve on a diamond-burnished surface, Cutting and tool in technological systems, vol. 100, pp. 119–138, 2024. **21**. *M. Tomov, P. Karolczak, H. Skowronek, P. Cichosz, M. Kuzinovski*: Mathematical Modelling of Core Roughness Depth During Hard Turning. In: *Królczyk, G., Niesłony, P., Królczyk, J. (eds)* Industrial Measurements in Machining. IMM 2019. Lecture Notes in Mechanical Engineering. Springer, Cham. 2020. https://doi.org/10.1007/978-3-030-49910-5_1

Сілард Смольницькі, Дьюла Варга, Мішкольц, Угорщина

АНАЛІЗ ШОРСТКОСТІ ПОВЕРХНІ ПРИ АЛМАЗНОМУ ВИГЛАДЖУВАННІ У ВЗАЄМОЗВ'ЯЗКУ З ВИКИДАМИ ВУГЛЕКИСЛОГО ГАЗУ

Анотація. *У сфері механічної переробки викиди вуглекислого газу також можуть бути значними. Тому важливо визначити оптимальні процеси з правильними параметрами процесу, які допоможуть зменшити викиди CO_2. Очевидно, що низьковуглецеве виробництво стало ключовим очікуванням у промисловості. Тому кількісний аналіз споживання енергії та викидів CO_2 у виробничих процесах є важливим. Саме це веде нас від наукового розуміння ефективного виробництва до промислового впровадження. Ґрунтуючись на обраному методі, ми представили, як можна кількісно оцінити викиди CO_2, що утворюються під час алмазного вигладжування. За підсумками розрахунку ми представили технологічні параметри, що застосовуються в процесі механічної обробки, випробувальні зразки, на яких вимірювалася шорсткість поверхні після алмазного вигладжування, і кілька додаткових розрахунків, необхідних для оцінки даних. Аналогічні тенденції спостерігалися як для 2D, так і для 3D показників шорсткості поверхні. Було встановлено, що для кожної комбінації величини подачі і швидкості вигладжування на отриманій параболі можна визначити мінімальну точку, за межами якої шорсткість поверхні вже не зменшується. Тому не рекомендується застосовувати більш високі сили вигладжування за межами цієї точки, оскільки це не тільки погіршує якість поверхні, але й збільшує викиди вуглекислого газу через більш високе споживання енергії. Крім того, ми визначили, що якщо досягнення найкращої якості поверхні не є суворою вимогою, варто розглянути можливість модифікації технологічних параметрів. Це може значно зменшити споживання енергії та викиди CO_2 – на 60–70% – і навіть скоротити час обробки, одночасно підвищуючи енергетичну та екологічну ефективність процесу. Таким чином, можна одночасно вирішити дві загальні цільові функції - мінімізацію часу обробки і споживання енергії. Щодо аналізу кривих Еббота-Файрстоуна було продемонстровано, що частка пікової зони зростає як при найнижчій, так і при найвищій силі вигладжування, тоді як зона долини досягає свого мінімуму при цих значеннях. Таким чином, цих значень сили вигладжування слід уникати. При використанні більш високої швидкості подачі спостерігався чіткий максимум зони розжолобка, який є оптимальним для утримання мастила, в той час як зона піку досягала свого мінімуму. Враховуючи, що попередні результати також визначили вищі швидкості подачі як з точки зору викиду CO_2, так і з точки зору часу обробки, рекомендується вибрати цей параметр у запропонованій комбінації параметрів, поряд із вищими швидкостями вигладжування та силою вигладжування в діапазоні 60–80 Н.*

Ключові слова: *енергоефективність; сталий розвиток; вигладжувальне алмазне полірування; обробка поверхні.*

UDC 621.91.01 **doi: 10.20998/2078-7405.2025.102.08**

FORM ACCURACY AND CUTTING FORCES IN TURNING OF X5CRNI18-10 SHAFTS: A STUDY ON CYLINDRICITY, COAXIALITY, STRAIGHTNESS, AND WAVINESS AT SMALL FEEDS

Muhammad Hamza **Daud** [0009-0002-7932-2135], El Majdoub **Wafae** [0009-0004-5926-661X], István **Sztankovics** [0000-0002-1147-7475]

University of Miskolc, 3515 Miskolc-Egyetemváros, Hungary
istvan.sztankovics@uni-miskolc.hu

Received: 07 June 2025 / Revised: 08 June 2025 / Accepted: 16 June 2025 / Published: 20 June 2025

Abstract. *This paper investigates how the cutting speed (vc), feed rate (f) and depth of cut affects the cutting forces and the quality of the surface during turning operations. For the study different experiments have been performed at two depths of cut (0.5 mm and 1.0 mm) to observe how they affect the cutting force, cylindricity, coaxiality (COAX DIN), straightness and waviness. From the results it can be said that the cutting forces and surface deviations increase with the increase in depth of cut. Cutting force normally brings down the forces and enhances surface quality but feed rate has exactly opposite impact. Thus, it is necessary to choose parameters wisely to keep machining efficiency and dimensional accuracy in balance.*
Keywords: *turning; cutting parameters; cutting forces; cylindricity; straightness; waviness.*

1. Introduction

In metal cutting industries, turning operation is one of the most used machining processes in the aim of manufacturing cylindrical parts with defined dimensions, surface quality and geometric tolerances. Furthermore, surface roughness is the key factor in evaluating machined parts. There is a demand for precise components with high accuracy, especially like shafts used in medical, aerospace and automotive systems [1,2]. The functional performance of the components is affected by shape error elements such as cylindricity, coaxiality and surface roughness as well as tool wear behaviour [3,4]. Austenitic stainless steel X5CrNi18-10 is used in many industries because of its good formability, corrosion resistance and mechanical strength. But it is still treated as a challenge when it comes to machining due to its low thermal conductivity, ductility and hardening behaviours. These can produce higher cutting forces and shape errors in addition to tool wear and poor chip control [5-7]. The effects on the tool-workpiece system are more pronounced when different feeds are used, which makes controlling cutting parameters a key to enhancing productivity [8]. The cutting force is the focus of any machining process.

Those forces generate cutting tool deflections, vibration, shape errors and heat that influence the surface integrity and lead to deviations affecting the accuracy of the machined part [9,10]. Based on many studies, the cutting forces can be increasing while increasing the feed and depth of cut. However, the cutting speed has minimal impact. These effects of studied parameters cannot be generalised because these effects depend on the workpiece material, tool type and cutting environments [11,12]. Making it hard to balance efficient material removal and dimensional accuracy, especially with stainless steels [13].

Numerous research studies focused on the influence of cutting parameters such as cutting speed, feed rate and depth of cut on surface roughness. However, fewer studies have examined cutting conditions on deeper geometrical errors like cylindricity, coaxiality, roundness and straightness. These errors are critical to be reduced, especially when they affect the functionality of the components [14,15]. Even though the small feeds enhance the surface roughness, they do not improve the shape accuracy of the part due to the unstable cutting conditions produced, which make the system sensitive to vibrations. This can cause misalignments on the machined parts [16,17].

This research examines the cutting forces and shape errors such as cylindricity, coaxiality, straightness and waviness under cutting parameters (cutting speed, depth of cut and feed) using X5CrNi18-10 stainless steel shafts during turning operation. This study focused on the influence of small feeds and how they affect the accuracy of the turned components. As mentioned in many studies, the small feed tends to enhance the surface quality. However, it can introduce challenges in terms of enhancing geometric precision due to produced vibration and dynamic disturbance which can result in misalignments and waviness impacting the accuracy and functionality of the part. The study tries to provide deep insight into process behaviour and the importance of optimising the cutting parameters in the aim of enhancing surface quality.

2. Experimental conditions and methods

The objective of this research is to study the impact of varying the cutting parameters on major cutting force and shape error elements during turning operations. To conduct the analysis, both experimental tests and theoretical calculations were carried out. In this study the feed was varied in two levels (0.08, 0.24 mm/rev), and cutting speed varied in two levels (200, 300 m/min) under two depths of cut, 0.5 and 1 mm.

At first an experiment test was carried out using stainless steel X5CrNi18.10 workpieces with 310 HV10 hardness. The material abbreviations stand for chromium-nickel austenitic stainless steel that is widely used due to its excellent corrosion resistance. Five workpieces with a 50 mm diameter divided into five surfaces of 30 mm length separated by 5 mm grooves were utilised to capture cutting

forces and measure shape errors. However, only eight setups were selected to conduct this evaluation and were mentioned in Table 1.

The HAAS ST-20Y-EU lathe, with lubrication provided by a 5% emulsion of "CIKS HKF 420" coolant oil, performed the cutting tests by mounting a DNMG150604-MF1 CP500 carbide/ceramic insert with a negative rake angle, fixed on a DDJNL2525M15 tool holder, into the machine. The tool used is suitable for hard cuts. In the aim of saving the generated cutting force, a dynamometer was connected to the machine with three amplifiers to capture the changes. The cutting forces were divided into three components: major cutting force, feed force and passive force, but only major cutting force was selected to be studied in this paper. This measurement then was plotted using Python, and force main and standard deviation were calculated.

Finally, the shape error of the workpieces used was measured by the Talyrond 365 precision measuring device, based on standard procedures and methodologies from previous research. Each test run, a 22.0 mm axial length of the cylinder was

Table 1 – Summary of the applied setups in the experiments

Setup	1	2	3	4	5	6	7	8
v_c [m/min]	200	300	200	300	200	300	200	300
f [mm]	0.08	0.08	0.24	0.24	0.08	0.08	0.24	0.24
a [mm]	0.5	0.5	0.5	0.5	1.0	1.0	1.0	1.0

The evaluated parameters were the following:

- F_c – Major Cutting Force [N]
- σ_c – Standard deviation of the Major Cutting Force [N]
- *CYLt* – Total Cylindricity error [μm]
- *COAX* – Coaxility error [μm]
- *STRt* – Straightness error [μm]
- W_z – Maximum Height of the Waviness Profile [μm]

Based on DoE methodology, the polynomial was formulated equation (presented in Equation 1) in the aim of modelling and analysing the parameters under evaluation. The equation factors presented the main variables (feed rate *f*, cutting speed v_c and depth of cut a_p) and their interactions. The constant (k_i) in the equation provides information on how the mentioned factors affect the cutting force and shape error parameters and highlights the ones that have a bigger influence. This study

facilitates the optimisation of machining conditions for enhanced accuracy and surface quality.

$$y(v_c, f, a) = k_0 + k_1 v_c + k_2 f + k_3 a + k_{12} v_c f + k_{13} v_c a + k_{23} f a + k_{123} v_c f a \quad (1)$$

3. Experimental results

Various evaluations were performed to complete investigation of the cutting parameters variations. To study the effect of cutting parameters on cutting speed and shape error components, Equations were calculated. The chosen error parameters are the following cylindricity, coaxiality, straightness and waviness. The tables 3,4,5,6 and 7 show respectively the measurement of Major cutting force, standard variation of cutting force, cylindricity, coaxiality, straightness and waviness. The formulas for the calculations of output parameters under investigation were taken from Equation 1. Equation 2 defines the cutting force in the interested region.

$$F_c(v_c, f, a) = ((22.56a - 12.74)f + 0.32a - 0.13)v_c + (-4812.a + 3747.)f - 37.5a + 58.9 \quad (2)$$

The equation for the variation in standard deviation is given by Equation 3:

$$\sigma_c(v_c, f, a) = ((0.39a - 0.46)f - 0.034a + 0.042)v_c + (-85.9a + 131.7)f + 8.67a - 10.63 \quad (3)$$

The cylindricity error can be calculated with the following Equation 4:

$$CYLt(v_c, f, a) = ((0.2188a + 0.3269)f - 0.01571a - 0.07666)v_c + (-23.01a - 80.19)f + 3.004a + 24.38 \quad (4)$$

The error in coaxiality is given by the Equation 5 below:

$$COAX(v_c, f, a) = ((-0.04875a + 0.01375)f - 0.0047a + 0.01130)v_c + (13.00a + 30.81)f + 1.939a - 5.515 \quad (5)$$

Straightness error can be verified mathematically by Equation 6:

$$STRt(v_c, f, a) = ((-0.10a + 0.07)f + 0.012a - 0.0076)v_c + (24.1a - 14.5)f - 2.33a + 1.53 \quad (6)$$

Finally, the waviness can be represented mathematically by Equation 7:

$$W_z(v_c, f, a) = ((0.003917a + 0.006832)f + 0.001539a + 0.000310)v_c - (0.5626a + + 1.506)f - 0.3856a + 0.0284 \quad (7)$$

Table 2 – Measurement results of the Major Cutting Force

F_c [N]	Setup							
No.	1	2	3	4	5	6	7	8

Result	130.21	121.65	298.16	266.29	131.58	229.36	275.53	530.49

Table 3 – Measurement results of the Standard Deviation of the Major Cutting Force

σ_c [N]	Setup							
No.	1	2	3	4	5	6	7	8
Result	1.50	1.84	7.17	3.25	2.07	2.26	7.17	6.24

Table 4 – Measurement results of the Total Cylindricity error

CYLt [μm]	Setup							
No.	1	2	3	4	5	6	7	8
Result	8.63	3.67	7.93	9.95	9.39	4.52	10.35	14.21

Table 5 – Measurement results of the Coaxility error

COAX [μm]	Setup							
No.	1	2	3	4	5	6	7	8
Result	0.06	0.87	5.69	6.33	0.69	1.07	6.58	6.40

Table 6 – Measurement results of the Straightness error

STRt [μm]	Setup							
No.	1	2	3	4	5	6	7	8
1	0.20	0.18	0.07	0.65	0.08	0.42	0.57	0.18
2	0.06	0.04	0.51	0.45	0.52	0.51	0.85	0.45
Avg.	0.13	0.11	0.29	0.55	0.30	0.47	0.71	0.32

Table 7 – Measurement results of the Maximum Height of the Waviness profile

W_z [μm]	Setup							
No.	1	2	3	4	5	6	7	8
1	0.064	0.246	0.048	0.279	0.029	0.260	0.043	0.611
2	0.057	0.196	0.053	0.380	0.024	0.320	0.036	0.466
3	0.050	0.241	0.067	0.432	0.012	0.291	0.029	0.349
Avg.	0.049	0.228	0.045	0.364	0.019	0.290	0.032	0.475

4. Discussion

The paper continues with the analysis of the experimental results and the deducted equations.

The alteration of the major cutting force is analysed at first (Figure 1). For lower depth of cut in first plot, it can be noticed that cutting forces F_c increases a

little bit with feed rate f and decreases noticeably with the cutting speed v_c. The plot is almost flat, which shows less dependency of F_c to feed rate at this setting. The rage of cutting forces is about 300 *N* to 500 *N*, where the smallest values occurring at high cutting speeds and lower feed rates. This behavior can be depicted as a sign of stable and efficient cutting conditions with moderate force requirements.

While for the higher depth of cut in second plot), both feed rate and cutting speed shows higher dependency on cutting force F_c increases rapidly with both parameters and showing steep surface profile. The range of forces is higher also. Which is from around 200 *N* to 600 *N*, where the highest values can be noticed at high feed and speed. Thus, it depicts increased tool engagement and removal of material and results in higher loads on the system. It can be said that cutting on these conditions needs careful parameter control to not engage excessive forces.

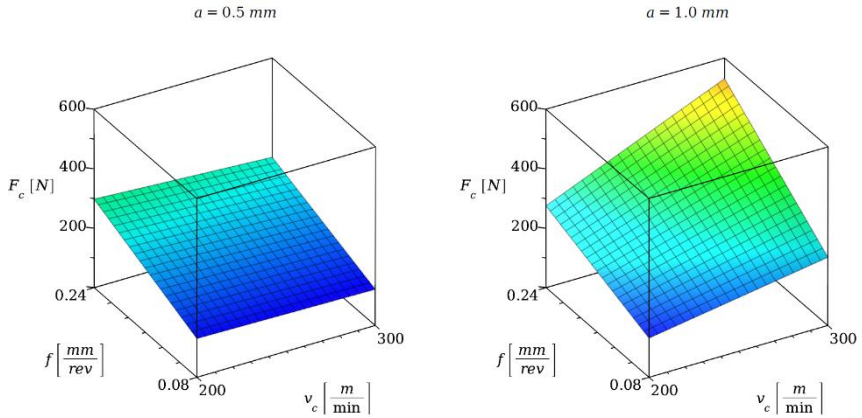

Figure 1 – Alteration of the Major Cutting Force in the studied range

The standard deviation of the major cutting force is analysed next (Figure 2). The first plot with lower depth of cut shows clear decrease in specific cutting force σ_c with increase in cutting speed v_c and feed rate f clear slope can be observed in both directions with higher values σ_c up to 8 *N* corresponding to low speeds and high feed rates. This behaviour depicts smaller efficiency at lower cutting speeds and moderate dependence to feed changes at shallow depths.

At higher depth of cut, the behaviour of σ_c remains similar with slight decrease in the curvature. The values of specific cutting forces still go down with increasing the v_c, but the effect of feed rate becomes stronger across the surface. The range of values is still the same but smooth slopes can be seen. Which depicts higher stability for cutting behaviour.

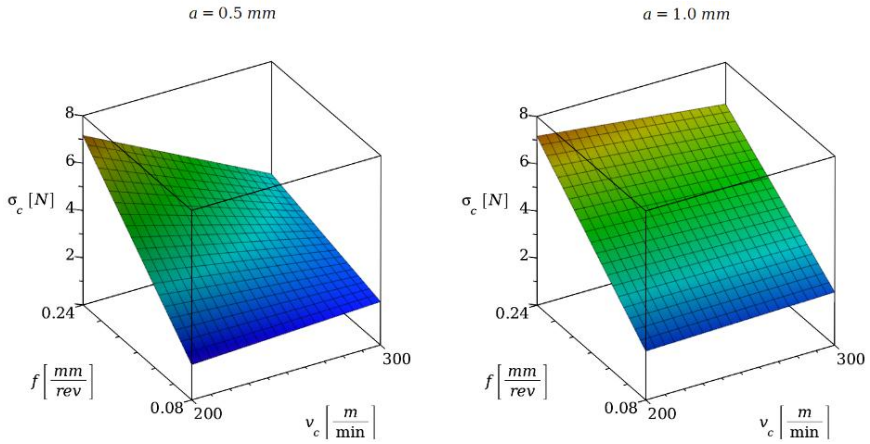

Figure 2 – Alteration of the Standard deviation of the Major Cutting Force in the studied range

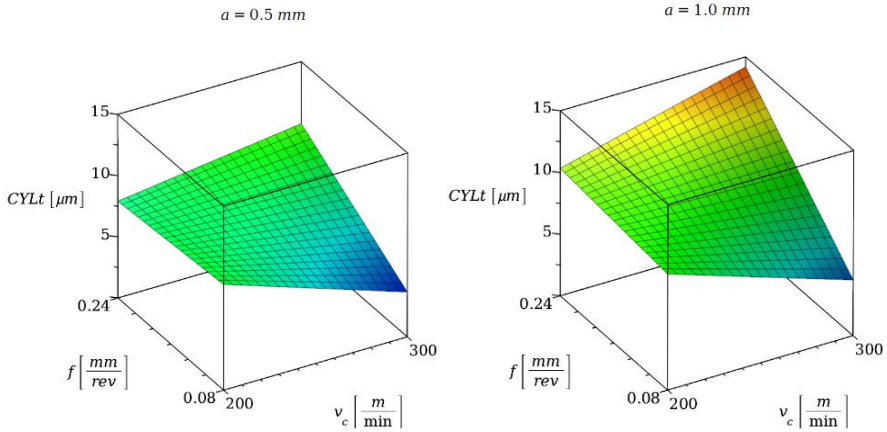

Figure 3 – Alteration of the Total Cylindricity error in the studied range

The cylindricity error (Figure 3) changes moderately with feed rate and cutting speed. *CYLt* has small but direct relation with feed rate, while indirect relation exists between *CYLt* error and cutting speed. The range of error is roughly from 5 μm to 13 μm. This behaviour depicts less geometrical accuracy at lower cutting speed and higher feeds at shallow depth of cut. For higher depth of cut the cylindricity error has more distinct reaction to both parameters. And it increases with both feed rate and cutting speed reaches up to 15 μm. The higher inclination shows that with the increase in any of the parameters, cylindricity becomes poorer and corresponds to bigger tool deflection and vibration effects at higher depth of cut.

At lower depth of cut in the first plot, steady increase in coaxiality error (*COAX*) with feed rate and small increase in coaxiality with cutting speed can be noticed (Figure 4). *COAX* reaches its maximum value of 8 µm at low cutting speed and it drops to less than 2 µm at high speeds and low fee rates. The smooth slope depicts predictable and controlled error behaviour at shallow depth, where cutting depth is the more effective parameter in reducing the error. *COAX* shows the same behaviour at 1.0 mm depth of cut, increasing with feed and decreasing with cutting speed. But the surface is more uniform, and it has the same maximum value of 8 as in first plot. That predicts that at higher depth the *COAX* is less sensitive to parameter changes, but the general behaviour is almost consistent.

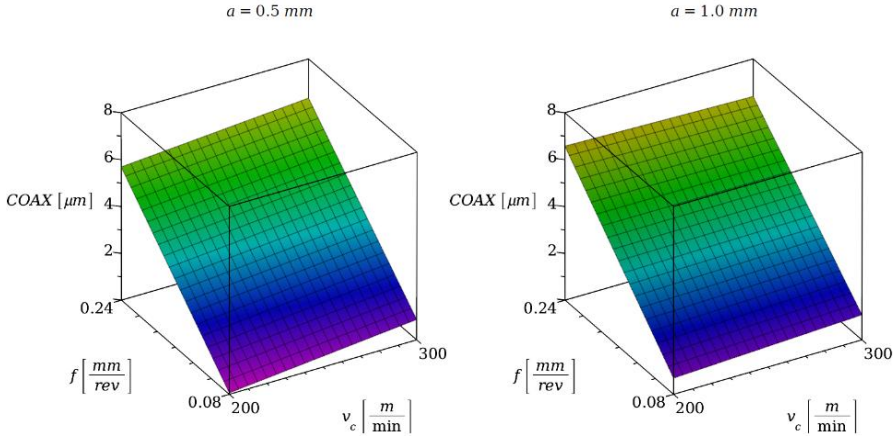

Figure 4 – Alteration of the Coaxility error in the studied range

Figure 5 shows the alteration of the straightness error. The first figure denotes the relation of straightness error (*STRt*) with feed rate is direct while it is indirect with cutting speed. The range of error is about 0.2 µm to 0.8 µm and reaches to highest at high feed and low cutting speed. The slope clearly signifies the impact of both parameters on straightness at shallow depth, but cutting speed is more impactful in reducing the error. At higher depth of cut the *STRt* shows similar relation, direct with feed rate and inverse with cutting speed. But the surface is less steep, and the error lies between 0.3 µm and 0.7 µm. This depicts a more stable and less sensitive response at higher depth of cut. But higher feed rates can still lead to higher errors.

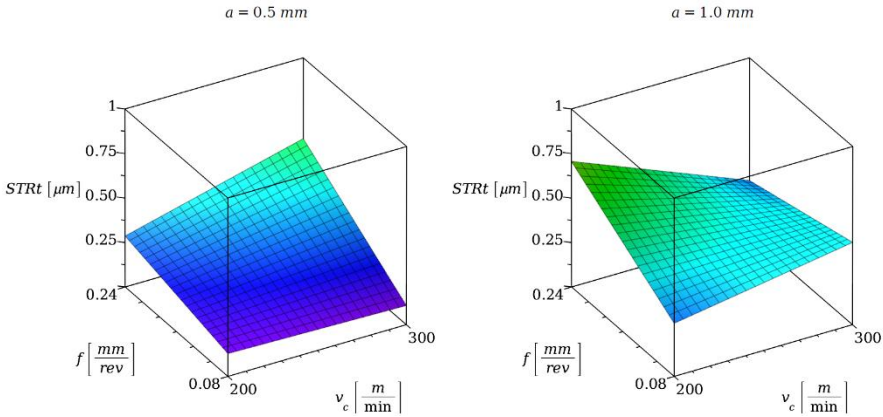

Figure 5 – Alteration of the Straightness error in the studied range

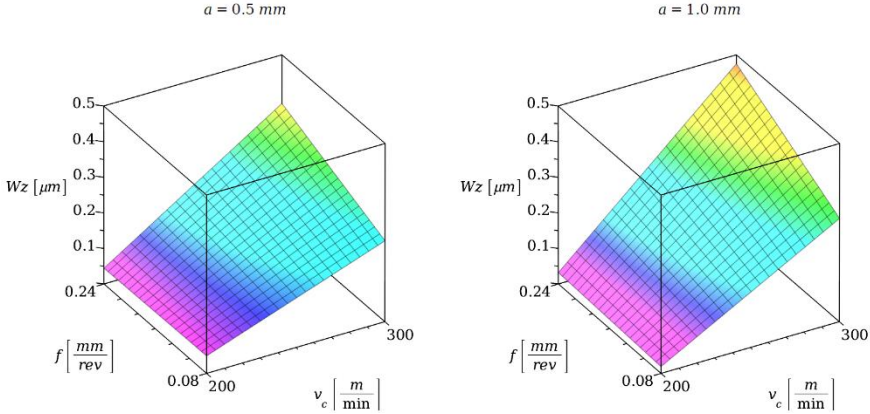

Figure 6 – Alteration of the Maximum Height of the Waviness profile in the studied range

Lastly, the waviness is analysed (Figure 6). It can be noticed in the first plot that waviness W_z has direct relation with both feed rate and cutting speed. The range of roughness lies in between 0.05 μm to 0.45 μm. At higher feed rate and cutting speed a gradual inclination can be observed which indicates that roughness becomes more noticeable with aggressive machining. Thus, both feed and cutting speed take part in surface degradation. By increasing the depth of cut, W_z increases more rapidly with feed rate and cutting speed, with almost same maximum value of 0.5 μm. The slope is higher and shows more dependence on parameter changes. This demonstrates that the high cutting conditions will lead to more roughness and higher

depth of cut increases the effect of mechanical interaction on the smoothness of surface.

5. Conclusions

The study investigated the effects of cutting speed, feed rate, and depth of cut on cutting force and surface quality in turning operations. Cutting forces became higher with the increase in the depth of cut from 0.5 mm to 1.0 mm significantly, and the effect of feed and speed on all the output values was also magnified. At smaller value of depth of cut (0.5 mm) cutting force went down and were less affected by feed. While the higher depth of cut (1.0 mm) has more impact and rose the forces sharply up to 600 *N*. specific cutting forces went down for both dept of cuts. Surface errors had direct relation with feed rate and indirect with cutting speed. And these effects were more noticeable at higher depth of cut. It can be summarized that higher depth of cut signifies both mechanical and geometrical deviations and the control of feed and cutting speed is necessary to surface quality and reducing cutting forces particularly for higher depth of cut, in turning operations.

References: 1. *Petropoulos, G.; Pandazaras, C.; Davim, J. P.* Surface integrity in machining. In Surface Integrity in Machining 2010. https://doi.org/10.1007/978-1-84882-874-2_2 **2.** *Kalpakjian, S.; Schmid, S.; Sekar, V.* Manufacturing engineering and technology. 2013. **3.** *Altintas, Y.; Ber, A. A.* Manufacturing automation: Metal cutting mechanics, machine tool vibrations, and CNC design. Applied Mechanics Reviews 2001, 54. https://doi.org/10.1115/1.1399383 **4.** *Campos, P. H. S.; Davim, J. P.; Ferreira, J.; Paiva, A.; Balestrassi, P.* The machinability of hard materials – A review. In Machinability of Advanced Materials 2014. https://doi.org/10.1002/9781118576854.ch5 **5.** *Nouari, M.; List, G.; Girot, F.; Coupard, D.* Experimental analysis and optimisation of tool wear in dry machining of aluminium alloys. Wear 2003, 255, 1359–1368. https://doi.org/10.1016/S0043-1648(03)00105-4 **6.** *Ghani, J. A.; Haron, C. H. C.; Kasim, M. S.; Sulaiman, M. A.; Tomadi, S. H.* Wear mechanism of coated and uncoated carbide cutting tool in machining process. Journal of Materials Research 2016, 31, 1873–1879. https://doi.org/10.1557/jmr.2015.382 **7.** *Kaladhar, M.; Kambagowni, V.; Rao, C. S.* Machining of austenitic stainless steels – A review. International Journal of Machining and Machinability of Materials 2012, 12, 178–192. https://doi.org/10.1504/IJMMM.2012.048564 **8.** *Kovalchenko, A.* Studies of the ductile mode of cutting brittle materials (A review). Journal of Superhard Materials 2013, 35. https://doi.org/10.3103/S1063457613050018 **9.** *Adesta, E.; Riza, M.; Al Hazza, M.; Agusman, D.; Rosehan, R.* Tool wear and surface finish investigation in high speed turning using cermet insert by applying negative rake angles. European Journal of Scientific Research 2009, 38, 180–188. **10.** *Grzesik, W.* Advanced machining processes of metallic materials: Theory, modelling, and applications, 2nd ed.; Elsevier, 2016. **11.** *Özel, T.* Predictive modeling of surface roughness and tool wear in hard turning using regression and neural networks. International Journal of Machine Tools and Manufacture 2005, 45, 467–479. https://doi.org/10.1016/j.ijmachtools.2004.09.007 **12.** *Ozcelik, B.; Bayramoğlu, M.* The statistical modeling of surface roughness in high-speed flat end milling. International Journal of Machine Tools and Manufacture 2006, 46, 1395–1402. https://doi.org/10.1016/j.ijmachtools.2005.10.005 **13.** *Saini, S.; Ahuja, I.; Sharma, V.* The effect of cutting parameters on surface integrity in hard turning. Applied Mechanics and Materials 2011, 110–116, 751–757. https://doi.org/10.4028/www.scientific.net/AMM.110-116.751 **14.** *Benardos, P. G.; Vosniakos, G. C.* Predicting surface roughness in machining: A review. International Journal of Machine Tools and Manufacture 2003, 43, 833–844. https://doi.org/10.1016/S0890-6955(03)00059-2 **15.** *Dogra, M.; Sharma, V. S.; Dureja, J.* Effect of tool geometry variation on finish

turning – A review. Journal of Engineering Science and Technology Review 2011, 4, 1–13. https://doi.org/10.25103/jestr.041.01 **16.** *Padhan, S.; Wagri, N.; Dash, L.; Das, A.; Das, S.; Rafighi, M.; Sharma, P.* Investigation on surface integrity in hard turning of AISI 4140 steel with SPPP-AlTiSiN coated carbide insert under nano-MQL. Lubricants 2023, 11, 49. https://doi.org/10.3390/lubricants11020049 **17.** *Sivaprakasam, T.; Hasan, S.* Machinability of hard martensitic stainless steel and hard alloy steel by CBN and PCBN tools by turning process. Proceedings of the World Congress on Engineering 2011, 1

Мухаммад Хамза Дауд, Ель Майдуб Вафае, Іштван Станкович, Мішкольц, Угорщина

ТОЧНІСТЬ ФОРМИ І СИЛИ РІЗАННЯ ПРИ ТОЧІННІ ВАЛІВ ЗІ СТАЛІ X5X5XH18-10: ДОСЛІДЖЕННЯ ЦИЛІНДРИЧНОСТІ, СПІВВІСНОСТІ, ПРЯМОЛІНІЙНОСТІ І ХВИЛЯСТОСТІ ПРИ МАЛИХ ПОДАЧАХ

Анотація. *Шорсткість поверхні є ключовим фактором при оцінці оброблених деталей. Існує потреба в точних деталях, особливо таких як вали, що використовуються в медичних, аерокосмічних та автомобільних системах. На функціональні характеристики компонентів впливають такі похибки форми, як циліндричність, співвісність і шорсткість поверхні, а також поведінка при зносі інструменту. Аустенітна нержавіюча сталь X5CrNi18-10 використовується в багатьох галузях промисловості завдяки її хорошій формоздатності, стійкості до корозії та механічної міцності. Але вона все ще розглядається як проблемна, коли справа доходить до механічної обробки через його низьку теплопровідність, пластичність і загартування, які можуть спричиняти вищі зусилля різання та похибки форми на додаток до зносу інструменту та поганого контролю стружки. Метою даного дослідження є вивчення впливу зміни параметрів різання на основні сили різання і похибки форми елементів при токарних операціях. Для проведення аналізу були проведені як експериментальні випробування, так і теоретичні розрахунки. У цьому дослідженні подача варіювалася на двох рівнях (0,08, 0,24 мм/об), а швидкість різання варіювалася на двох рівнях (200, 300 м/хв) при двох глибинах різання, 0,5 і 1 мм. Зусилля різання стали вищими зі збільшенням глибини різання з 0,5 мм до 1,0 мм значно, а також було збільшено вплив подачі та швидкості на всі вихідні значення. При меншому значенні глибини різання (0,5 мм) зусилля різання знижувалося і на них менше впливала подача. У той час як більша глибина різання (1,0 мм) має більший вплив і різко зростає зусилля до 600 Н. Питомі зусилля різання знижуються для обох випадків різання. Поверхневі похибки мали пряму залежність від величини подачі і непряму – від швидкості різання. І ці ефекти були більш помітні при більшій глибині різання. Можна підвести підсумок, що більша глибина різання при токарних операціях означає як механічні, так і геометричні відхилення, а контроль подачі та швидкості різання необхідний для якості поверхні та зменшення сили різання, особливо при більшій глибині різання.*

Ключові слова: *токарна обробка; параметри різання; зусилля різання; циліндричність; прямолінійність; хвилястість.*

UDC 621.91.01 **doi: 10.20998/2078-7405.2025.102.09**

CUTTING FORCE DISTRIBUTION IN TANGENTIAL TURNING OF 42CRMO4 ALLOY STEEL: INFLUENCE OF HIGH CUTTING SPEEDS AND HIGH FEED RATES

István **Sztankovics** [0000-0002-1147-7475], István T. **Pásztor** [0000-0002-6971-3063]

University of Miskolc, 3515, Miskolc - Egyetemváros, Hungary
istvan.sztankovics@uni-miskolc.hu

Received: 05 June 2025 / Revised: 09 June 2025 / Accepted: 13 June 2025 / Published: 20 June 2025

Abstract. *This study investigates the cutting force distribution during tangential turning of 42CrMo4 alloy steel under high cutting speeds and high feed rates. The experiments were conducted by varying cutting speed (200 and 250 m/min), feed rate (0.3 and 0.8 mm/rev), and depth of cut (0.1 and 0.2 mm). The major cutting force, feed directional force, and thrust force components were measured, and their maximum values and relative ratios were analysed. The results indicate that both cutting speed and feed rate have a significant influence on the magnitude and distribution of the cutting force components. Higher cutting speeds generally led to a reduction in cutting force values, while increased feed rates resulted in higher force magnitudes and altered force ratios. The obtained data contribute to a better understanding of the cutting mechanics in tangential turning, supporting process optimization and the selection of appropriate cutting parameters for improved machining performance.*
Keywords: *design of experiments; cutting force; experiment; tangential turning.*

1. Introduction

In modern manufacturing, the continuous demand for higher productivity, improved surface quality, and extended tool life has driven the development of advanced machining processes [1]. Turning, as one of the most fundamental and widely applied cutting operations, plays a crucial role in the production of rotationally symmetric parts across various industries, including automotive, aerospace, and general engineering [2]. To meet the increasing requirements for precision and efficiency, alternative turning methods have been developed [3], among which tangential turning [4] offers several notable advantages. Tangential turning is a variant of conventional turning where the cutting tool is mounted tangentially relative to the workpiece surface. This tool orientation modifies the cutting mechanics, leading to potentially lower cutting forces [5], more stable cutting action, and enhanced chip removal [6]. As a result, tangential turning can improve tool life, surface finish, and dimensional accuracy, particularly in the machining of difficult-to-cut or high-strength materials [7]. Despite these advantages, the detailed understanding of the cutting mechanics in tangential turning, especially under specific process conditions, remains limited and requires further investigation.

Tangential turning represents a non-conventional turning method where the cutting insert is positioned tangentially to the workpiece surface, as opposed to the traditional radial orientation [4]. This configuration leads to distinct cutting mechanics, often resulting in favourable force distributions and potential improvements in tool life, surface integrity, and process stability. While tangential turning has received growing attention in recent years, its behaviour under specific cutting conditions, especially at high cutting speeds [8] combined with high feed rates [9], remains insufficiently explored.

Understanding the cutting forces generated during any machining operation is essential for process optimization [10,11], tool design [12,13], and prediction of surface quality [14,15]. In tangential turning, the distribution of cutting forces among the major cutting force, feed directional force, and thrust force differs from conventional turning due to the altered engagement of the cutting edge and chip formation mechanics. The analysis of these force components and their ratios provides valuable insights into the efficiency and stability of the cutting process. High cutting speeds are often employed in modern manufacturing [16] to enhance productivity, reduce cycle times, and improve surface finish. However, when combined with high feed rates and shallow depths of cut, the force dynamics may change significantly. Such conditions are frequently encountered in finishing operations or when machining precision components made of alloy steels such as 42CrMo4 [17-19]. This material, widely used in the automotive, aerospace, and general engineering industries, offers a good balance of strength, toughness, and machinability, making it a common choice for components requiring high dimensional accuracy and surface quality [20-22]. Despite the practical relevance of these cutting conditions, there is still limited experimental data available concerning the detailed behaviour of cutting force components in tangential turning of 42CrMo4 alloy steel. The lack of comprehensive studies underlines the need for targeted investigations to support the development of more accurate force models, improve cutting parameter selection, and enhance overall process control.

The present study aims to address this gap by experimentally analysing the cutting force components during tangential turning of 42CrMo4 alloy steel at high cutting speeds and high feed rates. The maximum values of the major cutting force, feed directional force, and thrust force are measured under various cutting conditions, and the ratios between these force components are evaluated. The findings of this research contribute to a better understanding of cutting force distribution in tangential turning and offer practical guidelines for optimizing machining parameters in similar high-speed, high-feed applications.

2. Experimental conditions and methods

The objective of this study was to analyse the cutting forces generated during tangential turning operations. To achieve this, a series of cutting experiments were performed on an EMAG VSC 400 DS hard machining centre. Before the tangential turning experiments, the surfaces of the workpieces were pre-machined using a conventional turning tool equipped with a SANDVIK CNMG 12 04 12-PM 4314 insert. The tangential turning was carried out using a tool system with a 45° inclination angle, supplied by HORN Cutting Tools Ltd., consisting of the S117.0032.00 insert and the H117.2530.4132 holder. The cutting edge was an uncoated carbide insert (MG12 grade). The workpieces used were cylindrical specimens with an outer diameter of 60 mm, manufactured from 42CrMo4 alloy steel. Prior to machining, the material underwent hardening heat treatment, resulting in a hardness of approximately 410 HV10.

In the experiments, the effects of cutting speed (v_c), feed per revolution (f), and depth of cut (a) on the cutting forces were studied. The parameter levels were determined according to a full factorial (2^3) experimental design. For each parameter, two levels were selected: cutting speeds of 200 m/min and 250 m/min, feeds of 0.3 mm/rev and 0.8 mm/rev, and depths of cut of 0.1 mm and 0.2 mm, resulting in eight distinct test conditions (summarized in Table 1).

Table 1 – Experimental setups

Setup	1	2	3	4	5	6	7	8
v_c [m/min]	200	250	200	250	200	250	200	250
f [mm]	0.3	0.3	0.8	0.8	0.3	0.3	0.8	0.8
a [mm]	0.1	0.1	0.1	0.1	0.2	0.2	0.2	0.2

The cutting forces were recorded during machining using a Kistler 9257A three-component dynamometer. The measurement system included three Kistler 5011 charge amplifiers, a NI-9215 data acquisition unit connected to a cDAQ-9171 chassis, and data collection was managed through NI LabVIEW software. The dynamometer directly provided the cutting force components without the need for additional calculations.

The following cutting force components were evaluated in this investigation:

- F_c – the main cutting force acting along the cutting speed direction [N]
- F_f – the feed force acting in the feed direction [N]
- F_p – the passive force acting perpendicular to the previous ones [N]

The data analysis employed models based on the factorial design, where the dependent variable (y) was expressed as a function of the cutting parameters, and the coefficients (k_i) represented the influence of each parameter and their interactions.

$$y(v_c, f, a) = k_0 + k_1 v_c + k_2 f + k_3 a + k_{12} v_c f + k_{13} v_c a + k_{23} f a + k_{123} v_c f a \quad (1)$$

3. Experimental results

The cutting experiments were completed, and cutting forces were measured for each parameter combination. The recorded force–time signals were analysed, and the peak values of each force component were determined during the steady-state cutting phase, where the chip cross-section remained constant. These maximum values are summarized in Table 2. The corresponding mathematical models, derived through appropriate numerical analysis methods, are presented in Equations 2–4.

Table 2 – Measurement results

Setup	1	2	3	4	5	6	7	8
F_c [N]	197.9	204.0	421.1	406.7	393.1	388.2	687.2	663.3
F_p [N]	205.9	279.4	503.8	531.9	463.6	553.5	627.8	755.1
F_f [N]	61.1	72.9	172.4	177.9	149.4	274.6	328.0	348.1

$$F_c(v_c, f, a) = 192.6 - 0.9953 v_c - 246.5 f - 1793.2 a + 1.387 v_c f + \\ + 14.93 v_c a + 7960.3 f a - 27.14 v_c f a \quad (2)$$

$$F_f(v_c, f, a) = 132.7 - 0.8291 v_c - 293.7 f - 1109.6 a + 1.569 v_c f + \\ + 7.897 v_c a + 4265.7 f a - 14.45 v_c f a \quad (3)$$

$$F_p(v_c, f, a) = 319.1 - 2.808 v_c - 402.8 f - 3591.1 a + 5.190 v_c f + \\ + 35.75 v_c a + 7676.4 f a - 54.76 v_c f a \quad (4)$$

In addition to evaluating the individual force components, the analysis also included the investigation of the relationships between the forces. Examining the ratios of the cutting forces provides further insight into the chip formation mechanisms and helps characterize how the cutting process responds to different parameter settings. Accordingly, based on the results in Table 2, the force ratios F_c/F_p, F_c/F_f, and F_p/F_f were calculated for each of the eight experimental conditions. The calculated ratios are presented in Table 3. The corresponding mathematical expressions for these ratios, used for further analysis and interpretation, are shown in Equations 5–7.

Table 3 – Calculated ratios of the cutting forces

Setup	1	2	3	4	5	6	7	8
F_c/F_p [-]	0.961	0.730	0.836	0.765	0.848	0.701	1.095	0.878
F_c/F_f	3.239	2.799	2.443	2.285	2.632	1.413	2.095	1.905

F_p/F_f [-]	3.370	3.834	2.922	2.989	3.104	2.015	1.914	2.169

$$F_c / F_f\,(v_c, f, a) = 1.657 + 0.0157v_c + 4.082f + 7.693a - 0.03626v_cf - \\ - 0.085v_ca - 25.31fa + 0.1807v_cfa \quad (5)$$

$$F_c / F_p\,(v_c, f, a) = 1.213 + 0.00124v_c + 0.1803f + 6.507a - 0.00735v_cf - \\ - 0.05695v_ca - 4.953fa + 0.08726v_cfa \quad (6)$$

$$F_p / F_f\,(v_c, f, a) = 1.125 + 0.0128v_c + 2.243f - 6.81a - 0.012146v_cf + \\ + 0.04891v_ca + 0.127fa - 0.09437v_cfa \quad (7)$$

3. Discussion

The evaluation of the influence of the cutting parameters on the cutting forces was performed in two stages. Initially, the maximum values of each individual force component were analysed, followed by the assessment of the ratios between these force components.

The main cutting force (Figure 1) exhibited clear dependency on both feed rate, depth of cut, and cutting speed. Increasing the feed rate from 0.3 mm/rev to 0.8 mm/rev caused a significant rise in F_c at both depth levels. For the lower depth of cut (a = 0.1 mm), F_c increased from 197.9 N to 421.1 N at 200 m/min cutting speed, and from 204.0 N to 406.7 N at 250 m/min.

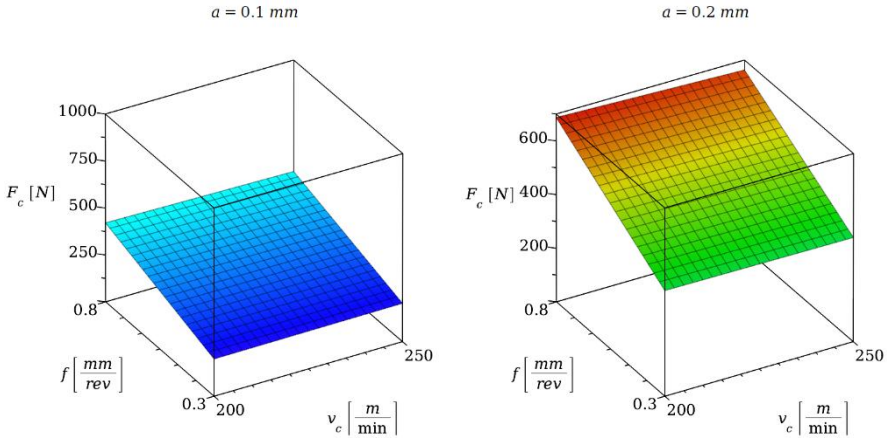

Figure 1 – Alteration of the F_c in the studied range

A similar trend is observed at the higher depth of cut (a = 0.2 mm), where the force increased from 393.1 N to 687.2 N at 200 m/min, and from 388.2 N to 663.3 N at 250 m/min. The increase in cutting speed generally led to a slight decrease or stabilization of F_c values for the same feed and depth of cut, especially at higher material removal rates. This indicates that higher cutting speeds slightly reduce cutting resistance, potentially due to thermal softening or reduced contact stresses at the tool-workpiece interface. The results confirm that feed rate and depth of cut have a dominant influence on the main cutting force, while the cutting speed plays a secondary, stabilizing role.

The feed force (Figure 2) showed a strong dependence primarily on feed rate and depth of cut, while cutting speed had a less pronounced but still observable effect. When the feed rate increased from 0.3 mm/rev to 0.8 mm/rev at a depth of 0.1 mm, F_f rose from 61.1 N to 172.4 N at 200 m/min, and from 72.9 N to 177.9 N at 250 m/min. For the larger depth of cut (a = 0.2 mm), F_f increased more steeply, reaching 328.0 N and 348.1 N at 200 m/min and 250 m/min, respectively. The cutting speed slightly increased the feed force at lower feed rates, but its influence diminished as both feed and depth of cut increased. The high sensitivity of F_f to the feed rate is expected, as feed directly affects the chip thickness and thus the resistance experienced by the tool in the feed direction. The relatively smaller effect of cutting speed on F_f suggests that chip formation mechanics in the feed direction are more strongly controlled by chip load than by thermal or frictional effects that cutting speed influences.

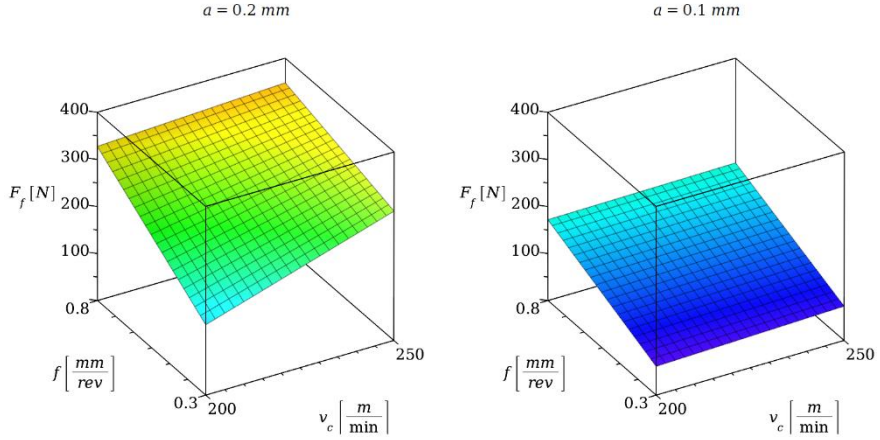

Figure 2 – Alteration of the F_f in the studied range

The passive force (Figure 3), which acts perpendicular to both feed and cutting directions, was strongly influenced by all three cutting parameters. Increasing the

feed rate from 0.3 mm/rev to 0.8 mm/rev at a constant depth of 0.1 mm resulted in a considerable increase of F_p from 205.9 *N* to 503.8 *N* at 200 m/min, and from 279.4 *N* to 531.9 *N* at 250 m/min. At the higher depth of cut (0.2 mm), the passive force further increased, reaching 627.8 *N* at 200 m/min and 755.1 *N* at 250 m/min under the highest material removal conditions. Unlike F_c and F_f, F_p appears to be more sensitive to cutting speed, especially at higher depths of cut and feeds, where thermal and dynamic effects may amplify side loading on the cutting edge. The higher values of passive force may indicate elevated radial loading, potentially affecting dimensional accuracy and tool deflection during tangential turning. These results show the need to control feed rate and depth of cut carefully to minimize side loading, especially in high-speed tangential turning

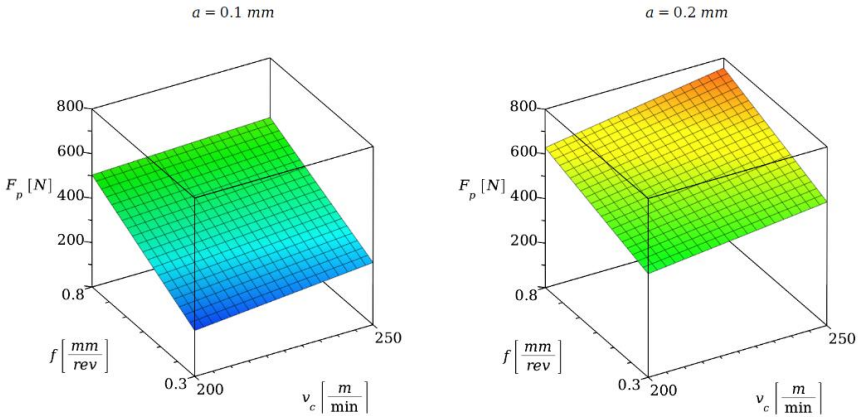

Figure 3 – Alteration of the F_p in the studied range

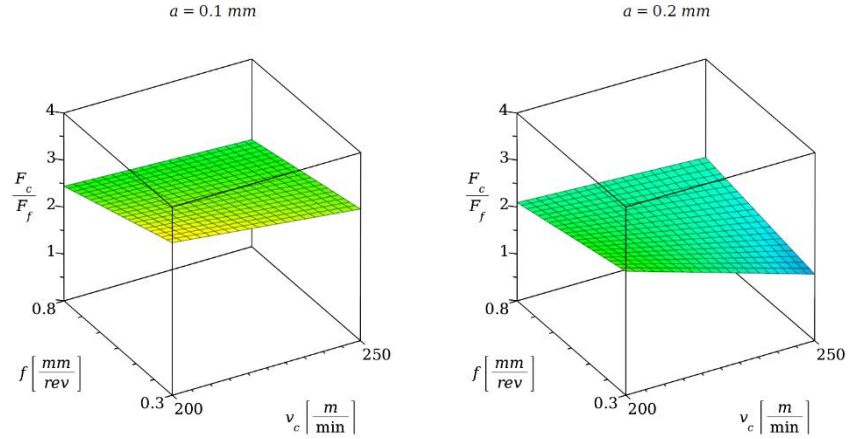

Figure 4 – The ratio of F_c and F_f in the studied range

The ratio of main cutting force to feed force (F_c / F_f) varied notably across the tested parameter combinations (Figure 4). At lower feed rates (0.3 mm/rev), the ratio ranged between 0.96 and 1.62, while at higher feeds (0.8 mm/rev), the ratio generally stabilized around 1.31 to 1.62. At lower depth of cut (0.1 mm), increasing cutting speed caused an increase in F_c / F_f, for example from 0.96 to 1.62 at 200 to 250 m/min when f = 0.3 mm/rev. However, at a = 0.2 mm, the ratio remained more stable, with values mostly around 1.62 regardless of cutting speed or feed. These results indicate that at higher chip loads, the increase in feed force tends to proportionally follow the increase in main cutting force, leading to more balanced force components. At lower depths and feeds, the cutting speed exerts more influence on this ratio, likely due to combined effects of thermal softening and cutting edge engagement dynamics. The stability of F_c / F_f at higher depths may suggest a more predictable force relationship under productive machining conditions.

The ratio between the main cutting force and passive force (Figure 5) was generally below 1.0 for most cutting conditions, indicating that the passive force was comparable to or exceeded the main cutting force.

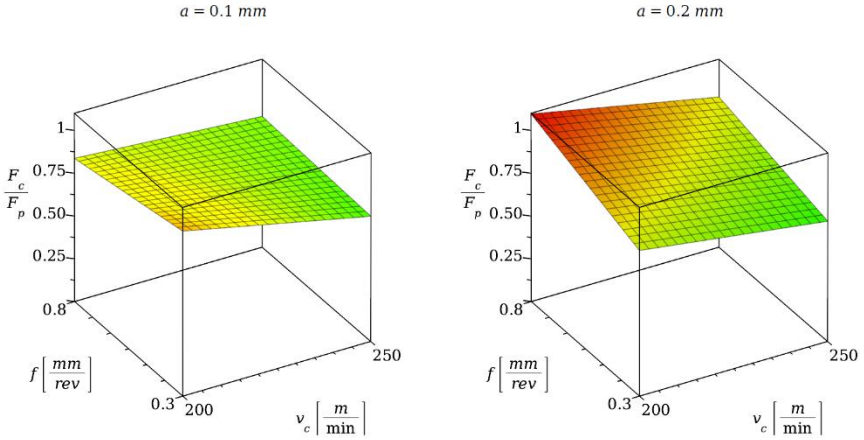

Figure 5 – The ratio of F_c and F_p in the studied range

At low feed and low depth of cut (f = 0.3 mm/rev, a = 0.1 mm), the ratio was near unity (0.96 at 200 m/min) but decreased to 0.73 at 250 m/min. At higher feeds (0.8 mm/rev), F_c / F_p remained below 1.0 for most conditions, with values ranging between 0.70 and 0.84 at lower depth, and reaching 1.09 and 0.88 at higher depth of cut (a = 0.2 mm). This shows that increasing feed and depth of cut both increase passive force more aggressively than the main cutting force. The decrease of F_c / F_p

with cutting speed also suggests that thermal effects at higher speeds may disproportionately elevate radial forces. These results highlight the particular significance of passive forces in tangential turning and their potential role in influencing tool deflection, surface waviness, and stability.

The passive-to-feed force ratio (Figure 6) showed a decreasing trend as feed rate and depth of cut increased. At the lowest feed and depth (f = 0.3 mm/rev, a = 0.1 mm), the ratio was relatively high, reaching 3.37 at 200 m/min and 3.83 at 250 m/min, indicating that at light cutting conditions, the passive force dominates over feed force. However, as feed increased to 0.8 mm/rev, F_p / F_f reduced to values between 2.92 and 2.99 at lower depth, and further decreased to around 1.91–2.17 at a = 0.2 mm. This suggests that increasing material removal rate leads to a more balanced distribution between passive and feed forces, as feed force grows more rapidly than passive force. The cutting speed had a minor effect on this ratio, with slightly higher values observed at 250 m/min for the lowest feeds. These results imply that at heavier cutting conditions, radial loading becomes less dominant relative to feed resistance, contributing to improved process stability but potentially increasing tool wear in the feed direction.

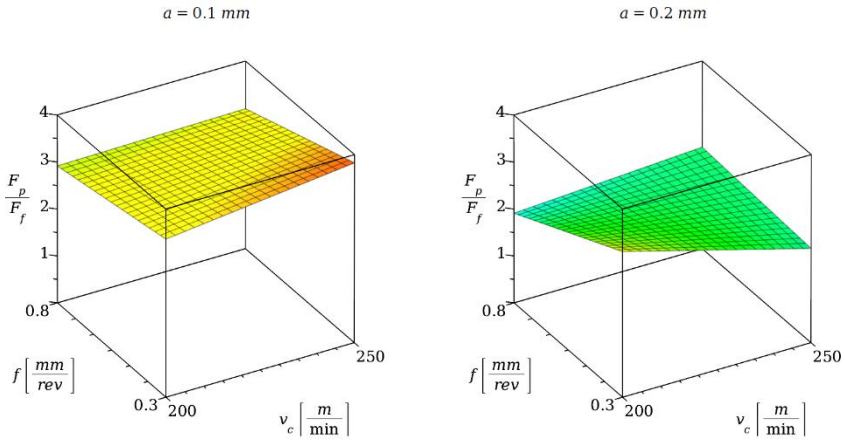

Figure 6 – The ratio of F_p and F_f in the studied range

4. Conclusions

In this study, cutting force components were analysed in tangential turning under varying cutting conditions. The experiments were conducted on 42CrMo4 alloy steel workpieces using a tangential turning tool with a 45° inclination angle. The tested cutting parameters included two cutting speeds (200 and 250 m/min), two feed rates (0.3 and 0.8 mm/rev), and two depths of cut (0.1 and 0.2 mm), resulting

in a full factorial experimental design with eight unique setups. The major cutting force, feed force, and passive (thrust) force were measured for each combination using a three-component dynamometer. Additionally, the ratios between the force components were calculated to further characterize the cutting process. The experimental results revealed several important findings.

1. Both feed and depth of cut had a dominant influence on all force components, with higher values leading to significant increases in F_c, F_f, and F_p.
2. The cutting speed mainly influenced the passive force, especially at higher material removal rates, where the increased speed led to higher radial forces.
3. The ratio analyses showed that at higher feeds and depths of cut, the F_c/F_f ratio stabilized around 1.6, indicating a more balanced relationship between cutting and feed forces under productive conditions.
4. Finally, the passive-to-feed force ratio (F_p/F_f) decreased as feed and depth of cut increased, suggesting that under heavier cutting conditions, the feed force grew more rapidly than the passive force, reducing radial load dominance and potentially improving process stability.

These findings contribute to a deeper understanding of the force distribution in tangential turning at high cutting speeds and high feed rates, supporting better parameter selection for stable and efficient machining.

6. Acknowledgement

Supported by the University Research Scholarship Program of the Ministry for Culture and In-novation from the source of the National Research, Development and Innovation fund. Contract identifier: TNI/1648-64/2024. Scholarship identifier: EKÖP-24-4-II-15.

References: 1. *Kumar, K., Zindani, D., & Davim, J. P.* Advanced machining and manufacturing processes. In Materials forming, machining and tribology. (2018). https://doi.org/10.1007/978-3-319-76075-9 **2.** *Huda, Z.* Machining processes and machines. In CRC Press eBooks. (2020). https://doi.org/10.1201/9781003081203 **3.** *Vasileva, D., Avramova, T., & Rusev, S.* Comparative Analysis of Some Traditional Andandn-Traditional Cutting Schemes in the Turning Process. International Journal of Manufacturing Economics and Management, 4(2), 36–42. (2024). https://doi.org/10.54684/ijmem.2024.4.2.36 **4.** *Schreiber, L., Trott, K.* Verfahren zur Drallfreien Spanenden Bearbeitung von Rotationssymmetrischen Flächen. Patent DE19963897A1, 28 April 1999. **5.** *Rao, C., Rao, D. N., & Srihari, P.* Influence of cutting parameters on cutting force and surface finish in turning operation. Procedia Engineering, 64, 1405–1415. (2013). https://doi.org/10.1016/j.proeng.2013.09.222 **6.** *Klocke, F., & Kratz, H.* Advanced tool edge geometry for high precision hard turning. CIRP Annals, 54(1), 47–50. (2005). https://doi.org/10.1016/s0007-8506(07)60046-8 **7.** *Kishawy, H. A., & Hosseini, A.* (2018). Machining Difficult-to-Cut materials. In Materials forming, machining and tribology. https://doi.org/10.1007/978-3-319-95966-5 **8.** *Hamdan, A., Sarhan, A. a. D., & Hamdi, M.* An optimization method of the machining parameters in high-speed machining of stainless steel using coated carbide tool for best surface finish. The International Journal of Advanced Manufacturing Technology, 58(1–4), 81–91. (2011). https://doi.org/10.1007/s00170-011-3392-5 **9.** *Korkut, I., & Donertas, M.* The influence of feed rate and cutting speed on the cutting forces,

surface roughness and tool–chip contact length during face milling. Materials & Design (1980-2015), 28(1), 308–312. (2005). https://doi.org/10.1016/j.matdes.2005.06.002 **10.** *Namboodri, T., & Felhő, C.* Correlation Analysis Between Components of Force and Vibration in Turning Of 11smn30 Steel. Cutting & Tools in Technological System, 101, 39–50. (2024). https://doi.org/10.20998/2078-7405.2024.101.04 **11.** *Pálmai, Z., Kundrák, J., Felhő, C., & Makkai, T.* Investigation of the transient change of the cutting force during the milling of C45 and X5CrNi18-10 steel taking into account the dynamics of the electro-mechanical measuring system. The International Journal of Advanced Manufacturing Technology, 133(1–2), 163–182. (2024). https://doi.org/10.1007/s00170-024-13640-6 **12.** *Kundrák, J., Mitsyk, A. V., Fedorovich, V. A., Markopoulos, A. P., & Grabchenko, A. I.* Simulation of the Circulating Motion of the Working Medium and Metal Removal during Multi-Energy Processing under the Action of Vibration and Centrifugal Forces. Machines, 9(6), 118. (2021). https://doi.org/10.3390/machines9060118 **13.** *Saglam, H., Yaldiz, S., & Unsacar, F.* The effect of tool geometry and cutting speed on main cutting force and tool tip temperature. Materials & Design (1980-2015), 28(1), 101–111. (2005). https://doi.org/10.1016/j.matdes.2005.05.015 **14.** *Fan, X., & Loftus, M.* The influence of cutting force on surface machining quality. International Journal of Production Research, 45(4), 899–911. (2006). https://doi.org/10.1080/00207540600632208 **15.** *Felhő, C., & Mehdiyev, Z.* A study on milling parameters for enhanced surface quality of FDM-Printed PLA parts. International Journal of Integrated Engineering, 16(6). (2024). https://doi.org/10.30880/ijie.2024.16.06.024 **16.** *Ezugwu, E. O.* High speed machining of aero-engine alloys. Journal of the Brazilian Society of Mechanical Sciences and Engineering, 26(1), 1–11. (2004). https://doi.org/10.1590/s1678-58782004000100001 **17.** *Zhu, Z., Lu, Y., Xie, Q., Li, D., & Gao, N.* Mechanical properties and dynamic constitutive model of 42CrMo steel. Materials & Design, 119, 171–179. (2017). https://doi.org/10.1016/j.matdes.2017.01.066 **18.** *Mehdi, K., Monka, P. P., Monkova, K., Sahraoui, Z., Glaa, N., & Kascak, J.* Investigation of dynamic behavior and process stability at turning of Thin-Walled tubular workpieces made of 42CRMO4 steel alloy. Machines, 12(2), 120. (2024). https://doi.org/10.3390/machines12020120 **19.** *Nagy, A., & Varga, G.* Effect of abandonment of cooling and lubrication on surface roughness and cylindricity in turning of steel. Multidiszciplináris Tudományok, 11(4), 395–407. (2021). https://doi.org/10.35925/j.multi.2021.4.43 **20.** *Brnic, J., Turkalj, G., Canadija, M., Lanc, D., & Brcic, M.* Study of the effects of high temperatures on the engineering properties of Steel 42CRMO4. High Temperature Materials and Processes, 34(1). (2014). https://doi.org/10.1515/htmp-2014-0011 **21.** *Xu, Q., Zhao, J., & Ai, X.* Cutting performance of tools made of different materials in the machining of 42CrMo4 high-strength steel: a comparative study. The International Journal of Advanced Manufacturing Technology, 93(5–8), 2061–2069. (2017). https://doi.org/10.1007/s00170-017-0666-6 **22.** *Sahib, M. M., & Kovács, G.* Multi-objective optimization of composite sandwich structures using Artificial Neural Networks and Genetic Algorithm. Results in Engineering, 21, 101937. (2024). https://doi.org/10.1016/j.rineng.2024.101937

Іштван Станкович, Іштван Пастор, Мішкольц, Угорщина

РОЗПОДІЛ ЗУСИЛЛЯ РІЗАННЯ ПРИ ТАНГЕНЦІАЛЬНІЙ ТОКАРНІЙ ОБРОБЦІ ЛЕГОВАНОЇ СТАЛІ 42CRMO4: ВПЛИВ ВИСОКИХ ШВИДКОСТЕЙ РІЗАННЯ ТА ВЕЛИКИХ ЗНАЧЕНЬ ПОДАЧІ

Анотація. *У цьому дослідженні були проаналізовані складові сили різання при тангенціальному точінні при різних умовах різання. Експерименти проводилися на заготовках з легованої сталі 42CrMo4 з використанням тангенціального токарного інструменту з кутом нахилу 45°. Перевірені параметри різання включали дві швидкості різання (200 і 250 м/хв), дві швидкості подачі (0,3 і 0,8 мм/об) і дві глибини різання (0,1 і 0,2 мм), що дозволило отримати повний факторіальний експериментальний дизайн з вісьмома унікальними установками. Основна сила різання, сила подачі та пасивна (тяга) сила вимірювалися для кожної комбінації за допомогою*

трикомпонентного динамометра. Крім того, співвідношення між силовими складовими були розраховані для подальшої характеристики процесу різання. Результати експериментів виявили кілька важливих висновків. Як подача, так і глибина різання мали домінуючий вплив на всі складові сили, причому більш високі значення призводили до значного збільшення Fc, Ff і Fp. Швидкість різання в основному впливала на пасивну силу, особливо при більш високих швидкостях зняття матеріалу, де підвищена швидкість призводила до більш високих радіальних сил. Аналіз співвідношення показав, що при більш високих подачах і глибині різання співвідношення Fc/Ff стабілізувалося близько 1,6, що вказує на більш збалансоване співвідношення між силами різання і подачі в продуктивних умовах. Нарешті, відношення сили пасивності до подачі (Fp/Ff) зменшувалося зі збільшенням подачі та глибини різання, що свідчить про те, що в більш важких умовах різання сила подачі зростала швидше, ніж пасивна сила, зменшуючи домінування радіального навантаження та потенційно покращуючи стабільність процесу. Ці результати сприяють глибшому розумінню розподілу зусиль при тангенціальному точінні при високих швидкостях різання та високій швидкості подачі, що сприяє кращому вибору параметрів для стабільної та ефективної обробки.

Ключові слова: *планування експериментів; сила різання; експеримент; тангенціальне точіння.*

UDC 621.7 **doi: 10.20998/2078-7405.2025.102.10**

GEOMETRICAL ACCURACY OF CONCRETE WALLS MANUFACTURED BY 3D PRINTING

Yaroslav **Garashchenko** [1][0000-0003-2568-4763], Olena **Harashchenko** [1][0000-0002-9572-6095], Ruslan **Kucher** [2][0009-0000-5835-4600]

[1]National Technical University «Kharkiv Polytechnic Institute», Kharkiv, Ukraine
[2]Mykolaiv National Agrarian University, Mykolaiv, Ukraine
yaroslav.garashchenko@gmail.com

Received: 08 June 2025 / Revised: 10 June 2025 / Accepted: 16 June 2025 / Published: 20 June 2025

Abstract. *The presented results were obtained during a theoretical and experimental study of the geometric accuracy and surface quality parameters of concrete walls manufactured using additive technologies. Theoretical aspects of the classification of defects and deviations of surfaces obtained by layered concrete construction have been developed. The study examines the influence of layer thickness on printing precision and defect formation in 3D concrete printing (3DCP) processes. Two experimental samples were fabricated with different layer thicknesses: 20 mm and 15 mm. Systematic measurements were conducted to evaluate crack depth on vertical surfaces, pore depth on horizontal surfaces, track width variations, and deviations from straight-line geometry. The experimental methodology involved comprehensive measurement protocols using precision instruments to assess geometrical parameters and surface quality characteristics. Statistical analysis was performed to quantify the relationships between layer thickness and printing accuracy, including calculations of mean values, standard deviations, and coefficients of variation for all measured parameters. Results demonstrate significant improvements in geometrical accuracy when reducing layer thickness from 20 mm to 15 mm. Crack depth on vertical surfaces decreased by 56%, while deviations from straight-line geometry improved by 32%. Most notably, track width stability showed a remarkable enhancement, with the coefficient of variation improving by 91%, indicating substantially improved process repeatability. The 15 mm layer thickness configuration exhibited superior performance across all measured parameters, demonstrating enhanced layer adhesion, reduced surface defects, and improved dimensional consistency. The coefficient of variation for crack depth decreased from 43% to 24%, while deviation variability reduced from 32% to 12%, confirming improved process control and predictability. These findings provide valuable insights for optimizing 3D concrete printing parameters and establishing quality control protocols for additive construction applications. The research contributes to the development of standardized practices for concrete 3D printing technology and demonstrates the critical importance of layer thickness optimization for achieving high-quality printed concrete structures. The results confirm the effectiveness of implementing thinner layers, given the increased requirements for geometric accuracy and surface quality in automated concrete construction processes. This research was conducted at "Geopolimer" LTD to implement innovative technologies in the construction industry.*

Keywords: *concrete 3D printing; construction; layer thickness optimization; geometrical accuracy; surface quality control; quality assessment; concrete defects analysis.*

1. Introduction

The construction industry is experiencing a paradigmatic shift towards digitalization and automation, with additive manufacturing technologies emerging as transformative solutions for addressing contemporary challenges in building construction. Three-dimensional concrete printing (3*DCP*) represents one of the most promising developments in this technological evolution, offering unprecedented opportunities for design freedom, material efficiency, and construction process optimization [1, 2]. This innovative approach enables the fabrication of complex geometrical structures while potentially reducing labor requirements, construction time, and material waste compared to conventional building methods [3, 4].

Despite significant advances in 3*DCP* technology, the widespread adoption of this manufacturing approach faces substantial challenges related to quality control and dimensional accuracy [5, 6]. Unlike traditional concrete construction methods that rely on formwork systems to ensure geometrical precision, 3*DCP* processes must achieve structural integrity and dimensional accuracy through careful control of material properties and printing parameters. The absence of external support structures during the printing process places increased demands on material rheology, layer adhesion, and process stability, making quality control a critical factor for the successful implementation of this process [7, 8].

2. Review of the literature

Current research in 3*DCP* has primarily focused on material development, printing system design, and structural performance evaluation, while comprehensive quality assessment methodologies remain underdeveloped [9,10]. The lack of standardized quality control protocols poses significant barriers to the industrial adoption of 3*DCP* technology, particularly for applications requiring high dimensional accuracy and surface quality standards. This knowledge gap is further compounded by the limited understanding of how process parameters influence defect formation and geometrical deviations in printed concrete structures [11,12].

The establishment of systematic quality control frameworks for 3*DCP* requires detailed characterization of defect types and their relationships to printing parameters. Surface defects in 3*DCP* can manifest in various forms, including layer delamination, surface roughness variations, dimensional inaccuracies, and structural discontinuities [13,14]. These defects not only compromise the aesthetic quality of printed structures but may also affect mechanical properties, durability, and long-

term performance. Understanding the mechanisms underlying defect formation is essential for developing predictive quality control systems and optimization strategies for printing parameters [15,16].

Layer thickness emerges as one of the most critical parameters influencing print quality and dimensional accuracy in 3*DCP* processes. Theoretical considerations suggest that thinner layers should provide better dimensional control and surface quality due to improved layer bonding and reduced gravitational effects on material deformation [17,18]. However, empirical validation of these relationships requires systematic experimental investigation with quantitative assessment of geometrical parameters and defect characteristics. Previous studies have provided limited data on the quantitative relationships between layer thickness and quality metrics, creating a need for comprehensive experimental research [19,20].

The development of automated quality control systems for 3*DCP* represents a critical advancement opportunity that could significantly enhance the reliability and industrial viability of additive construction technologies. Computer vision-based monitoring systems offer particular promise for real-time quality assessment, enabling continuous evaluation of print quality and immediate corrective actions when deviations are detected [21,22]. However, the implementation of such systems requires comprehensive methodological foundations that include detailed defect classification schemes, standardized measurement protocols, and validated relationships between process parameters and quality outcomes.

The establishment of a systematic methodological framework for defect classification and geometrical deviation assessment is fundamental to advancing automated quality control in 3*D* concrete printing. A comprehensive classification system must encompass various defect categories including surface texture variations, dimensional inaccuracies, layer bonding defects, and structural discontinuities. This methodological foundation is essential for training computer vision algorithms to accurately identify and quantify defects in real-time during the printing process [23,24]. The development of such classification schemes requires extensive experimental data collection across different printing conditions and systematic analysis of defect characteristics and their correlations with process parameters.

Furthermore, the integration of computer vision technologies into 3*DCP* quality control systems necessitates robust datasets that correlate visual defect characteristics with quantitative measurement data. These datasets serve as training foundations for machine learning algorithms designed to automatically detect and classify defects based on surface appearance, geometrical deviations, and texture characteristics. The effectiveness of computer vision systems depends critically on

the comprehensiveness and accuracy of the underlying classification methodology, making experimental validation of defect-parameter relationships a prerequisite for successful system development [25,26].

Current gaps in the literature include the absence of standardized defect classification schemes specific to 3*DCP* processes, limited quantitative data on the relationships between printing parameters and quality outcomes, and insufficient experimental validation of computer vision applications for concrete printing quality control [27,28]. These limitations hinder the development of reliable automated quality assessment systems and impede the establishment of industry standards for 3*DCP* quality control.

The primary objective of this research is to provide experimental validation of the relationship between layer thickness and geometrical accuracy in 3*DCP*, with particular emphasis on developing a systematic approach to defect characterization that can support future computer vision-based quality control systems. Specific aims include: quantitative assessment of the influence of layer thickness on surface quality parameters including crack formation, dimensional accuracy, and geometrical deviations; development of a comprehensive measurement methodology for characterizing print quality in 3*DCP* processes; establishment of statistical relationships between process parameters and quality metrics; and provision of foundational data for future computer vision system development through systematic defect documentation and classification.

This investigation contributes empirical data on quality-parameter relationships in additive construction and establishes methodological foundations for automated quality control systems. The systematic defect characterization approach provides essential groundwork for computer vision-based monitoring systems, supporting optimization strategies and standardized quality assessment protocols that could enhance the industrial acceptance of 3*DCP* technology.

3. Classification of Surface Defects in 3*D* Concrete Printing

3.1 Defect Classification Framework

The development of reliable quality control systems for 3*DCP* requires a comprehensive understanding and systematic classification of surface defects (shown in Fig. 1) that occur during the printing process. Classification and automated quality assurance of 3*D* concrete printed surfaces emphasize the critical need for standardized defect categorization to enable effective quality assessment protocols. A methodical approach to defect classification serves as the foundation

for developing computer vision-based detection systems capable of real-time quality monitoring and automated decision-making in construction applications [21–24].

a *b*

Figure 1 - Layer delamination & surface texture

High-quality 3*D* printed concrete wall demonstrating optimal layer bonding, consistent track width, and smooth surface finish in Fig 1a. This sample serves as a reference standard for acceptable print quality with minimal visible defects.

Layer delamination defect showing visible horizontal separation between consecutive layers with moderate surface texture irregularities, as shown in Fig. 1b. This example demonstrates inadequate interlayer bonding resulting in structural discontinuity typical of excessive time gaps between layer deposition.

Surface defects in 3*DCP* can be broadly categorized into four primary groups based on their formation mechanisms and visual characteristics: material-related defects, process-induced defects, environmental defects, equipment-related defects, etc. Each category encompasses specific defect types with distinct morphological features, severity levels, and implications for structural performance. This classification framework provides the systematic foundation necessary for training machine learning algorithms and establishing quality control thresholds for automated inspection systems.

3.1.1 Material-Related Defects

Crack Formation (Type A Defects) represents the most critical category of surface defects in 3*DCP*, directly affecting both aesthetic quality and structural integrity. Durability and Cracking Defects in 3*DCP* identifies several crack subtypes:

A1: Shrinkage Cracks – linear defects occurring perpendicular to the printing direction due to rapid moisture loss during the printing process. Characteristics: width 0.1–2.0 mm, depth 1–5 mm, typically appearing within 10–30 minutes after deposition.

A2: Thermal Cracks – irregular crack patterns resulting from differential thermal expansion/contraction. Characteristics: random orientation, width 0.2–3.0 mm, often forming network patterns on exposed surfaces.

A3: Stress Concentration Cracks – localized fractures at geometrical discontinuities or material interfaces. Characteristics: radiating patterns from stress concentration points, variable width, and depth.

Porosity and Void Formation (Type B Defects) – surface porosity significantly affects the visual quality and durability of 3*DCP* structures. Classification includes:

B1: Surface Pores – circular or elliptical voids at the surface level with diameters ranging from 1–10 mm and depths of 0.5–5 mm.

B2: Entrained Air Voids – spherical cavities resulting from air entrapment during mixing or pumping, typically 2–15 mm in diameter.

B3: Bleeding Voids – irregular depressions caused by water migration to the surface, characterized by smooth internal surfaces and variable geometry.

3.1.2 Process-Induced Defects

Layer Bonding Defects (Type C Defects) inadequate interlayer adhesion creates visible defects that compromise structural continuity:

C1: Layer Delamination – visible separation between consecutive layers, manifesting as horizontal lines or gaps along the printing direction.

C2: Cold Joints – insufficient bonding between layers due to extended time gaps, appearing as distinct boundaries with reduced material continuity.

C3: Layer Offsetting – misalignment between consecutive layers creating step-like surface irregularities.

Extrusion Quality Defects (Type D Defects) material flow irregularities during the printing process result in characteristic surface patterns:

D1: Under-extrusion – insufficient material deposition creating gaps, thin sections, or incomplete layer formation.

D2: Over-extrusion – excessive material flow causing bulging, irregular width variations, or material spillage.

D3: Flow Interruption – temporary cessation of material flow creating distinct boundaries and surface discontinuities.

3.1.3 Environmental and Equipment Defects

Environmental Impact Defects (Type E Defects). External conditions significantly influence surface quality during printing:

E1: Wind-induced Deformation – surface irregularities caused by air movement during the printing process.

E2: Temperature-related Surface Changes – rapid setting or delayed hardening due to ambient temperature variations.

E3: Moisture-related Defects – surface scaling, efflorescence, or irregular setting due to humidity fluctuations.

Equipment-Related Defects (Type F Defects). Mechanical system performance directly affects print quality:

F1: Nozzle Wear Patterns – irregular material distribution due to nozzle degradation or damage.

F2: Vibration-induced Irregularities – surface waviness or oscillation patterns caused by mechanical vibrations.

F3: Pressure Fluctuation Effects – variable extrusion rates creating periodic thickness variations.

3.1.4 Spatial Quality Mapping

Spatial Distribution Parameters (Type G - Geographic):

G1: Defect Clustering Index – a statistical measure quantifying the tendency of defects to occur in localized groups rather than being randomly distributed across the printed surface. Calculated K_{dc} using spatial autocorrelation analysis (Moran's I statistic adapted for 3*D* printing coordinates), this index ranges from -1 (perfect dispersion) to +1 (maximum clustering). Values K_{dc} above 0.3 indicate significant spatial clustering requiring investigation of localized process issues such as nozzle inconsistencies or material flow irregularities.

G2: Spatial Density Gradient – the rate of change in defect density per unit distance across different regions of the printed structure. Measured K_{sdg} as defects per square decimeter per meter of distance (defects/dm²/m), this parameter identifies systematic variations in print quality related to equipment positioning, material delivery constraints, or environmental gradients. High gradient values ($K_{sdg} > 2$ defects/dm²/m) suggest significant spatial quality variations requiring process parameter adjustment.

G3: Layer-wise Distribution Pattern – the systematic arrangement and frequency of defects as a function of printing height, analyzing both intra-layer (within single layers) and inter-layer (between consecutive layers) defect occurrence patterns. This parameter employs statistical pattern recognition to identify recurring defect arrangements such as periodic spacing, systematic clustering, or progressive quality degradation. Pattern classification includes: uniform (random distribution),

periodic (regular spacing), clustered (localized groupings), and progressive (systematic increase/decrease with height).

G4: Edge-to-Center Ratio – the quantitative relationship between defect density at the perimeter regions versus the central areas of printed elements, expressed as a dimensionless ratio K_{ec}. Calculated K_{ec} as (perimeter defect density)/(center defect density), values significantly different from 1.0 indicate edge effects, cooling rate differences, or path planning issues. Ratios $K_{ec} > 1.5$ suggest edge-related problems, while ratios $K_{ec} < 0.7$ indicate center-focused quality issues requiring different mitigation strategies.

Temporal-Spatial Evolution (Type H - Historical):

H1: Progressive Degradation Zones – spatial regions where print quality systematically deteriorates over time during the printing process, identified through temporal analysis of defect accumulation patterns. These zones are characterized by increasing defect density, severity escalation, or expanding defect area as printing progresses. Detection involves tracking quality metrics across consecutive time intervals and identifying areas where degradation rates exceed threshold values (>10% quality reduction per hour). Common causes include equipment wear, material property changes, or environmental condition drift.

H2: Cyclic Pattern Recognition – the identification and characterization of repeating defect patterns that occur at regular intervals in space, time, or both dimensions during the printing process. These patterns may manifest as periodic quality variations corresponding to mechanical system cycles, material delivery rhythms, or environmental fluctuations. The analysis employs Fourier transform techniques and autocorrelation functions to detect periodicities with frequencies ranging from layer-to-layer cycles (high frequency) to multi-hour material batch variations (low frequency). Significant cyclic patterns (amplitude >20% of baseline variation) indicate systematic process issues requiring targeted intervention.

H3: Build-up Effect Mapping – the quantitative assessment of cumulative quality changes resulting from the additive nature of layer-by-layer construction, where defects or process variations in lower layers influence the quality of subsequent layers. This phenomenon creates a spatial map of quality evolution where earlier defects can propagate, amplify, or modify quality patterns in upper regions. Mapping involves tracking quality metrics as functions of both spatial coordinates and cumulative build height, identifying zones where quality degradation accelerates due to structural instability, thermal accumulation, or geometric deviation propagation. Critical build-up effects are defined as quality degradation rates exceeding 5% per meter of build height.

The comprehensive spatial quality mapping framework enables the development of predictive quality control systems capable of identifying quality trends before they result in structural failures or aesthetic degradation.

3.1.5 Severity Classification and Detection Criteria

Each defect type is further classified according to severity levels to enable systematic quality assessment:

Severity Level 1 (Minor) – defects affecting only aesthetic quality without structural implications: crack width < 0.5 mm, depth < 2 mm; surface pores < 3 mm diameter, density < 5 pores/dm²; layer bonding irregularities < 1 mm displacement.

Severity Level 2 (Moderate) – defects requiring attention but not immediate rejection: crack width 0.5–1.5 mm, depth 2–5 mm; surface pores 3–8 mm diameter, density 5–15 pores/dm²; layer bonding irregularities 1–3 mm displacement.

Severity Level 3 (Critical) – defects requiring immediate corrective action or component rejection: crack width > 1.5 mm, depth > 5 mm; surface pores > 8 mm diameter, density > 15 pores/dm²; layer bonding irregularities > 3 mm displacement.

3.1.6 Material Property Defects (Type L – rheological)

Material Stiffness Variations (Type L Defects). Inconsistencies in material rheological properties affecting printability and structural integrity:

L1: Premature Stiffening – Accelerated material hardening that occurs faster than the designed setting time, resulting in extrusion difficulties and compromised interlayer adhesion. This defect manifests when the concrete mixture begins to lose workability before the intended processing window, typically due to rapid hydration, high ambient temperatures, or chemical accelerator overdosing. Characteristics: Irregular surface texture with visible boundaries between areas of different consistency, reduced track width by 10–25% compared to nominal dimensions, increased extrusion pressure requirements, and visible discontinuities at layer interfaces where fresh material fails to bond properly with prematurely stiffened previous layers.

L2: Delayed Setting - excessively long setting time of the material, which leads to deformation under its weight. Characteristics: "spreading" of the material, loss of geometric shape, visible traces of subsidence by 2–8 mm.

L3: Variable Workability – inconsistent rheological properties within a single printing session, resulting in unpredictable material behavior and non-uniform print quality. This defect typically stems from insufficient mixing, material segregation, temperature fluctuations, or inconsistent material supply. Alternating zones of different surface textures create a patchwork appearance, non-uniform extrusion width with variations exceeding ±5% of nominal dimensions, periodic changes in

surface quality ranging from smooth to rough textures, visible color or consistency variations indicating material composition changes, and inconsistent layer adhesion properties leading to weak interfaces in affected zones.

Detection Criteria for Material Stiffness:

– rheometer measurements: yield stress variations >±20%;

– visual assessment: consistency changes across print duration;

– dimensional analysis: track width coefficient of variation >5%.

3.1.7 Advanced Process-Specific Defect Categories

Enhanced Extrusion Quality Defects (Type M – Material flow)

Detailed classification of extrusion defects:

M1: Severe Under-extrusion – critical material deficiency with the formation of breaks and voids. Characteristics: lack of material in areas >5 mm, layer thickness <70% of the nominal, visible voids between filaments.

M2: Moderate Under-extrusion – moderate material deficiency with partial filling. Characteristics: layer thickness 70–90% of the nominal, uneven surface texture, local depressions 1–3 mm deep.

M3: Optimal Extrusion – compliance of extrusion parameters with design values. Characteristics: layer thickness 95–105% of the nominal, uniform texture, no visible defects.

M4: Moderate Over-extrusion – excess material with geometry deformation. Characteristics: layer thickness 110–130% of the nominal, local thickening, "spreading" of the material beyond the track by 2–5 mm.

M5: Severe Over-extrusion – critical excess of material with significant deformations. Characteristics: layer thickness >130% of the nominal, formation of "bubbles" and irregularities, loss of geometric accuracy >5 mm.

3.1.8 Interlayer Interface Defects (Type N – interface)

Defects in the orientation and curvature of interlayer boundaries:

N1: Layer Line Misalignment – violation of parallelism between successive layers. Characteristics: deviation angle >2°, visible "stepped" edges, violation of verticality of walls.

N2: Curvature Distortion – deformation of curvature in rounded areas. Characteristics: deviation of the radius of curvature >±5%, unevenness of the arc, local "flattening" or "sharpening".

N3: Interface Roughness – surface roughness in the contact zone between layers. Characteristics: height fluctuations >1 mm over a length of 10 cm, visible waviness, violation of the smoothness of transitions.

N4: Orientation Drift – progressive deviation of the orientation of layers from the nominal one. Characteristics: systematic increase in the angle of deviation along the height, formation of "sloping" walls, loss of perpendicularity.

3.1.9 Advanced Texture Classification (Type O – Optical/texture)

O1: Smooth Texture (Class A) – high-quality smooth surface. Characteristics: R_{max} < 1 mm, no visible irregularities, uniform surface structure.

O2: Fine Texture (Class B) – fine-grained texture of acceptable quality. Characteristics: R_{max} 1–5 mm, small regular irregularities, overall surface uniformity.

O3: Medium Texture (Class C) – moderately pronounced texture. Characteristics: R_{max} 5–12 mm, visible traces of extrusion, local irregularities, but integrity preserved.

O4: Coarse Texture (Class D) – coarse texture with significant irregularities. Characteristics: R_{max} 12–20 mm, large irregularities, visible structural defects, aesthetic quality impairment

O5: Unacceptable Texture (Class F) – unacceptable surface quality. Characteristics: R_{max} > 20 mm, multiple defects, integrity impairment, need for rework.

3.2 Classification of Dimensional Deviations and Geometric Variations

Dimensional accuracy in 3*D* concrete printing encompasses systematic deviations from intended geometry that affect both functional performance and aesthetic quality. Geometric quality assurance for 3*D* concrete printing establishes the critical importance of standardized measurement protocols for dimensional assessment. Unlike surface defects, geometric deviations are primarily quantitative parameters that can be precisely measured and statistically analyzed to establish process control limits and optimization strategies.

The geometric deviation classification system addresses three fundamental aspects: **dimensional accuracy** (absolute size conformance), **form accuracy** (shape fidelity), and **positional accuracy** (spatial relationship conformance). This systematic approach enables the development of comprehensive quality control metrics suitable for automated measurement systems and provides the foundation for establishing tolerances in 3*DCP* applications [8].

3.2.1 Dimensional Accuracy Deviations

Linear Dimension Variations (Type G Deviations). Linear dimensional deviations affect the primary geometric parameters of printed elements:

G1: Track Width Variations – deviations in the width of extruded material tracks from the nominal design value. Measurement protocol: perpendicular to the printing direction at standardized intervals (every 100 mm). Typical range: ±2–8 mm from nominal width.

G2: Layer Height Deviations - variations in individual layer thickness affecting overall component height. Measurement protocol: vertical measurement at predetermined grid points. Typical range: ±1–5 mm from nominal layer height.

G3: Overall Dimensional Drift - cumulative dimensional changes affecting total component dimensions. Measurement protocol: comparison with design dimensions using coordinate measurement techniques. Typical range: ±5–20 mm for large-scale components.

Cross-Sectional Variations (Type H Deviations). Profile irregularities affecting the consistency of extruded material geometry:

H1: Track Profile Asymmetry – deviations from the symmetric cross-sectional shape in extruded tracks. Quantified using profile scanning and symmetry indices.

H2: Edge Definition Quality – irregularities in track edge sharpness and consistency. Measured using edge gradient analysis and curvature assessment.

H3: Surface Texture Uniformity – variations in surface roughness and texture patterns across the printed surface. Quantified using surface profilometry and texture analysis parameters.

3.2.2 Form Accuracy Deviations

Straightness and Flatness Deviations (Type I Deviations). Geometric form errors affecting the intended shape of printed elements:

I1: Linear Straightness Deviations – deviations from straight-line geometry in nominally linear elements. A study on the mechanical properties of 3*D* printing concrete layers and the mechanism of influence of printing parameters demonstrates the significant impact of layer height on straightness accuracy. Measurement protocol: laser line scanning or photogrammetric analysis. Tolerance range: 2–10 mm over a 1-meter span.

I2: Surface Flatness Variations - deviations from planar surfaces in wall sections. Measured using coordinate measurement systems with grid-based analysis. Typical tolerance: 3–15 mm over 1 m² surface area.

I3: Curve Fidelity – accuracy of curved geometries compared to design intent. Quantified through the radius of curvature analysis and geometric fitting algorithms.

Angular and Perpendicularity Deviations (Type J Deviations). Orientation accuracy affecting geometric relationships:

J1: Vertical Deviation (Plumbness) – angular deviation from true vertical in wall elements. Measurement using inclinometers or laser levels. Typical tolerance: ±5–15 mm/m height.

J2: Corner Accuracy – deviations in angular relationships at intersections and corners. Measured using angle measurement devices and coordinate geometry analysis.

J3: Twist and Warping – three-dimensional deformations affecting overall element geometry. Quantified using 3*D* scanning and geometric analysis software.

3.2.3 Positional Accuracy Deviations

Location and Alignment Deviations (Type K Deviations). Spatial positioning accuracy affecting assembly and interface quality:

K1: Component Positioning – deviations in the absolute position of printed elements relative to design coordinates. Measurement using total station surveying or coordinate measurement systems.

K2: Layer Alignment – horizontal displacement between consecutive layers affecting wall straightness. Critical for maintaining structural continuity and aesthetic quality.

K3: Interface Consistency – variations in gaps, overlaps, and alignment at component interfaces and joints.

3.2.4 Layer-specific Dimensional Variations (Type L)

L1: Individual Layer Thickness Deviation – deviation of the thickness of individual layers from the nominal. Measurements: calipers, laser sensors. Tolerance: ±1 mm for layers of 15–20 mm.

L2: Cumulative Layer Build-up Error – cumulative error of thickness over the height of the structure. Measurements: 3*D* scanning with an accuracy of ±0.1 mm. Critical threshold: >2% of the total height.

L3: Layer-to-Layer Registration – accuracy of alignment of successive layers. Measurements: photogrammetry, coordinate measurement. Tolerance: ±0.5 mm horizontal displacement.

3.2.5 Measurement Protocols and Quality Control Thresholds

Standardized Measurement Framework. Implementation of systematic measurement protocols ensures consistent data collection for statistical process control:

– Sampling Strategy (minimum measurement frequency of 1 point per 0.25 m² of printed surface);

– Measurement Equipment (calibrated instruments with accuracy ±0.1 mm for dimensional measurements);

– Environmental Controls (measurements conducted under controlled conditions: temperature ±2°C, humidity ±5%).

Spray-based 3*D* concrete printing parameter design model demonstrates the importance of statistical approaches to quality control. The framework establishes:

– control limits, statistical boundaries (±3σ) for process variation monitoring;

– trend analysis, statistical process control charts for identifying systematic variations;

– corrective action triggers, and automated alerts when measurements exceed established control limits.

This comprehensive classification system provides the methodological foundation necessary for developing scientifically-based defect detection systems and establishing quality control standards for 3*D* concrete printing applications. The systematic approach enables the integration of automated measurement technologies while maintaining traceability to established engineering standards and practices.

4. Examples of defects and deviations

The experimental investigation involved systematic documentation of various defect types and quality variations encountered during 3*D* concrete printing trials. Representative samples were selected to illustrate the range of defects classified according to the proposed framework, demonstrating both the diversity of quality issues and the effectiveness of the classification system for practical quality assessment. Each sample was photographed under standardized lighting conditions and subjected to dimensional analysis to quantify the severity and characteristics of observed defects (Fig. 2).

The photographic documentation presented in Figure 2 illustrates the practical application of the proposed defect classification system across different severity levels and defect types. Sample Fig. 2a demonstrates critical quality failures requiring immediate process intervention, with multiple defect categories occurring simultaneously. This type of complex defect pattern emphasizes the importance of systematic classification for identifying root causes and implementing appropriate corrective measures. Sample Fig. 2b shows surface-level defects that primarily affect aesthetic quality but may indicate underlying process parameter optimization needs.

In contrast, sample Fig. 2c represents acceptable print quality standards achievable through proper process control, serving as a benchmark for quality assessment protocols. The minor surface texture variations observed fall within

acceptable tolerance ranges and demonstrate the achievable quality levels for the investigated printing system. Sample Fig. 2d illustrates structural integrity concerns where crack propagation affects multiple layers, requiring immediate attention to prevent potential structural failure.

a *b*

c *d*

The measurement protocols demonstrated in samples Fig. 2e and Fig. 2f highlight the quantitative assessment methodology essential for systematic quality control implementation. These measurement approaches provide the dimensional accuracy data necessary for statistical process control and continuous improvement of printing parameters. The systematic documentation and classification of these defect types provide the foundation for developing automated computer vision-based quality control systems capable of real-time defect detection and process optimization in industrial 3*D* concrete printing applications.

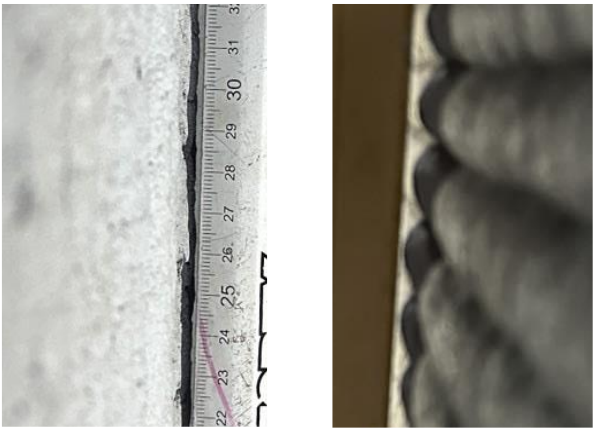

e *f*

Figure 2 - Samples of test 3*D* printing demonstrating various defect types and quality characteristics

The observed defect patterns confirm the validity of the proposed classification framework and demonstrate its practical utility for quality assessment in real-world 3*D* concrete printing scenarios. The diversity of defect types captured in these samples underscores the complexity of quality control challenges in additive concrete manufacturing and validates the need for comprehensive classification systems to support both manual inspection and automated quality assurance processes.

5. Statistical and comparative analysis of deviations in concrete walls manufactured by construction 3*D* printer

Wall printing was performed using the GP-01 gantry construction printer (manufactured by Geopolimer, Ukraine).

The comparative analysis of printing quality between 20 mm and 15 mm layer thickness configurations reveals significant improvements in multiple quality parameters when using thinner layers. Figure 3 presents the statistical comparison of key geometric and surface quality metrics obtained from systematic measurements of printed concrete wall samples.

The experimental results demonstrate substantial quality improvements when reducing layer thickness from 20 mm to 15 mm (table 1). Most notably, crack depth showed a dramatic reduction of 56.4%, decreasing from 8.76 mm to 3.82 mm. This

improvement can be attributed to enhanced layer bonding and reduced gravitational effects on the wet concrete material when using thinner layer configurations.

Table 1 Detailed Statistical Analysis

Parameter	Sample 1 (h_i = 20 мм)	Sample 2 (h_i = 15 мм)	Relative Change
Crack depth, mm	8.76 ± 3.92	3.82 ± 1.01	-56.4%
Track width, mm	56.89 ± 0.85	63.94 ± 0.60	+12.4%
Deviation from straight line, mm	2.91 ± 0.98	1.88 ± 0.31	-35.4%

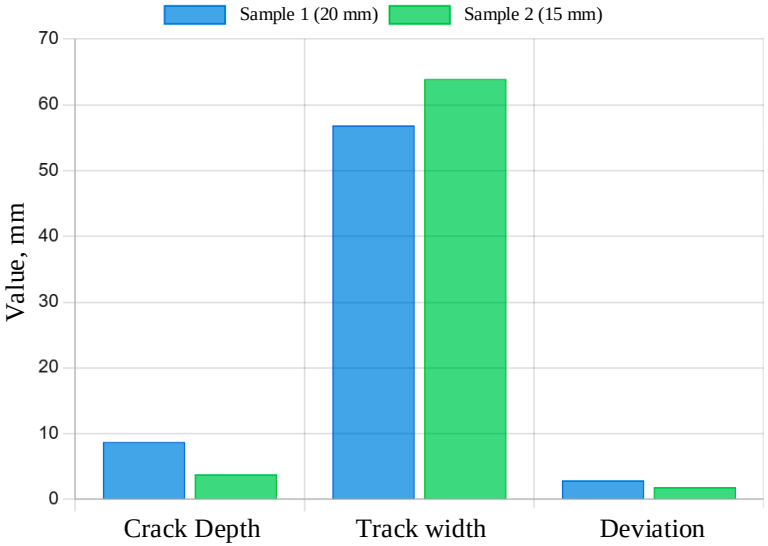

Figure 3 - Comparison of mean parameter values

Track width measurements revealed interesting behavior, with the 15 mm configuration producing wider tracks (63.94 mm) compared to the 20 mm configuration (56.89 mm), representing a 12.4% increase. This phenomenon indicates improved material flow characteristics and more consistent extrusion behavior with the optimized layer height settings. The reduced standard deviation (0.60 mm vs 0.85 mm) confirms enhanced process stability.

Geometric accuracy, measured as deviation from straight line, showed a significant improvement of 35.4%, with deviations reducing from 2.91 mm to

1.88 mm. This enhancement demonstrates the superior dimensional control achievable with thinner layer configurations, which is critical for structural applications requiring precise geometric tolerances.

6. Results and discussion

The analysis reveals three critical quality improvements. A crack depth reduction of 56.4% indicates that thinner layers significantly reduce crack formation, likely due to improved layer bonding and reduced internal stress accumulation. Geometric accuracy improvement of 35.4% demonstrates enhanced dimensional control and reduced deviation from design specifications. Process stability enhancement of 74.2% (calculated from variance reduction in crack depth measurements) confirms more predictable and consistent printing behavior.

The coefficient of variation analysis provides insights into process consistency and control. For crack depth, the coefficient of variation decreased from 44.7% (h_i = 20 mm) to 26.4% (h_i = 15 mm), indicating improved process predictability while still showing moderate variability that requires continued attention. Track width demonstrated excellent consistency with very low coefficients of variation (1.5% for 20 mm, 0.9% for 15 mm), confirming stable extrusion control across both configurations. Deviation from straight lines showed substantial improvement in consistency, with a coefficient of variation decreasing from 33.7% to 16.5%.

These statistical findings provide quantitative evidence supporting the optimization of layer thickness parameters for enhanced quality in 3*D* concrete printing applications. The comprehensive improvement across multiple quality metrics validates the effectiveness of the 15 mm layer configuration for achieving superior dimensional accuracy and surface quality in printed concrete structures.

7. Conclusions

This experimental investigation demonstrates the significant impact of layer thickness optimization on 3*D* concrete printing quality. The reduction from 20 mm to 15 mm layer thickness achieved substantial improvements: 56.4% reduction in crack depth (8.76±3.92 mm to 3.82±1.01 mm), 35.4% improvement in geometric accuracy (2.91±0.98 mm to 1.88±0.31 mm deviation), and enhanced process stability with coefficient of variation improving from 44.7% to 26.4%.

The comprehensive defect classification framework provides the first systematic approach for 3*D* concrete printing quality assessment, encompassing surface defects (Types A-F), dimensional deviations (Types G-K), and advanced process-specific categories (Types L-O). This framework establishes

methodological foundations for computer vision-based automated quality control systems and standardized assessment protocols.

The results demonstrate that 15 mm layer thickness represents the optimal configuration for enhanced quality outcomes. The quantified process-quality relationships enable evidence-based parameter optimization for industrial applications, while the developed measurement protocols provide practical tools for commercial quality control implementation.

Research expansion should include additional layer thicknesses, material compositions, and environmental conditions. Implementation of the proposed computer vision-based quality control system and long-term durability studies represent critical next steps for practical application and structural performance validation.

The demonstrated quality improvements support 3*D* concrete printing viability for structural applications requiring precise tolerances, providing construction industry stakeholders with quantitative evidence for adopting optimized printing parameters and systematic quality control methodologies.

References: 1. *Garashchenko, Y., Harashchenko, O., Kucher, R.* Additive technologies in construction: technical, economic and management analysis. Cutting & Tools in Technological System, (101), 2024. 103–115. **2.** *Buswell, R.A., De Silva, W.L., Jones, S.Z. and Dirrenberger, J.* 3D printing using concrete extrusion: A roadmap for research. Cement and concrete research, 112, 2018. pp. 37–49. **3.** *Rollakanti, C.R. and Prasad, C.V.S.R.* Applications, performance, challenges and current progress of 3D concrete printing technologies as the future of sustainable construction–A state of the art review. Materials Today: Proceedings, 65, 2022. pp. 995–1000. **4.** *Raphael, B., Senthilnathan, S., Patel, A. and Bhat, S.* A review of concrete 3D printed structural members. Frontiers in Built Environment, 8, 2023. p.1034020. **5.** *Roussel, N.* Rheological requirements for printable concretes. Cement and Concrete Research, 112, 2018. pp. 76–85. **6.** *Skripkiunas, G., Tolegenova, A., Rishko, L., Akmalaiuly, K. and Baltuškiene, D.* Durability and Cracking Defects in 3D‐Printed Concrete. Advances in Civil Engineering, 2025(1), 2025. p.8592029. **7.** *Bos, F., Wolfs, R., Ahmed, Z. and Salet, T.* Additive manufacturing of concrete in construction: potentials and challenges of 3D concrete printing. Virtual and physical prototyping, 11(3), 2016. pp. 209–225. **8.** *Buswell, R., Xu, J., De Becker, D., Dobrzanski, J., Provis, J., Kolawole, J.T. and Kinnell, P.* Geometric quality assurance for 3D concrete printing and hybrid construction manufacturing using a standardised test part for benchmarking capability. Cement and Concrete Research, 156, 2022. p. 106773. **9.** *Mechtcherine, V., Bos, F.P., Perrot, A., Da Silva, W.L., Nerella, V.N., Fataei, S., Wolfs, R.J., Sonebi, M. and Roussel, N.* Extrusion-based additive manufacturing with cement-based materials–production steps, processes, and their underlying physics: a review. Cement and Concrete Research, 132, 2020. p. 106037. **10.** *Zhang, J., Wang, J., Dong, S., Yu, X. and Han, B.* A review of the current progress and application of 3D printed concrete. Composites Part A: Applied Science and Manufacturing, 125, 2019. p. 105533. **11.** *Liu, W., Ji, D., Cui, W., Shi, X., Liu, C. and Tao, Y.* Research Progress on Quality Control Method of Concrete 3D Printing Based on Computer Vision. In International Conference on Computer Science and its Applications, Springer, Singapore. 2025. pp. 186–191. **12.** *Otto, J. and Maiwald, P.* Classification and automated quality assurance of 3D concrete printed surfaces. Automation in Construction, 164, 2024. p. 105467. **13.** *Panda, B., Paul, S.C., Hui, L.J., Tay, Y.W.D. and Tan, M.J.* Additive manufacturing of geopolymer for sustainable built environment. Journal

of cleaner production, 167, 2017. pp. 281–288. **14.** *Paul, S.C., Van Zijl, G.P., Tan, M.J. and Gibson, I.* A review of 3D concrete printing systems and materials properties: Current status and future research prospects. Rapid Prototyping Journal, 24(4), 2018. pp. 784–798. **15.** *Le, T.T., Austin, S.A., Lim, S., Buswell, R.A., Gibb, A.G. and Thorpe, T.* Mix design and fresh properties for high-performance printing concrete. Materials and structures, 45, 2012. pp.1221-1232. **16.** Huang, X., Yang, W., Song, F. and Zou, J. Study on the mechanical properties of 3D printing concrete layers and the mechanism of influence of printing parameters. Construction and Building Materials, 335, 2022. p. 127496. **17.** *Wangler, T., Roussel, N., Bos, F.P., Salet, T.A. and Flatt, R.J.* Digital concrete: a review. Cement and Concrete Research, 123, 2019. p. 105780. **18.** *Liu, X., Cai, H., Ma, G. and Hou, G.* Spray-based 3D concrete printing parameter design model: Actionable insight for high printing quality. Cement and Concrete Composites, 147, 2024. p. 105446. **19.** *Quah, T.K.N., Tay, Y.W.D., Lim, J.H., Tan, M.J., Wong, T.N. and Li, K.H.H.* Concrete 3D printing: Process parameters for process control, monitoring and diagnosis in automation and construction. Mathematics, 11(6), 2023. p. 1499. **20.** *Zhang, C., Deng, Z., Chen, C., Zhang, Y., Mechtcherine, V. and Sun, Z.* Predicting the static yield stress of 3D printable concrete based on flowability of paste and thickness of excess paste layer. Cement and Concrete Composites, 129, 2022. p. 104494. **21.** *Rill-García, R., Dokladalova, E., Dokládal, P., Caron, J.F., Mesnil, R., Margerit, P. and Charrier, M.* Inline monitoring of 3D concrete printing using computer vision, Addit. Manuf. 60, 2022. 103175 [online]. **22.** *Zhang, H., Tan, Y., Hao, L., Zhang, S., Xiao, J. and Poon, C.S.* Intelligent real-time quality control for 3D-printed concrete with near-nozzle secondary mixing. Automation in Construction, 160, 2024. p. 105325. **23.** *Kazemian, A., Yuan, X., Davtalab, O. and Khoshnevis, B.* Computer vision for real-time extrusion quality monitoring and control in robotic construction. Automation in Construction, 101, 2019. pp. 92–98. **24.** *Zhang, E., Li, B., Li, P. and Chen, Y.* A deep learning based printing defect classification method with imbalanced samples. Symmetry, 11(12), 2019. p. 1440. **25.** *Senthilnathan, S. and Raphael, B.* Using computer vision for monitoring the quality of 3D-printed concrete structures. Sustainability, 14(23), 2022. p. 15682. **26.** *Zhuang, Z., Xu, F., Ye, J., Hu, N., Jiang, L. and Weng, Y.* A comprehensive review of sustainable materials and toolpath optimization in 3D concrete printing. npj Materials Sustainability, 2(1), 2024. p. 12. **27.** *Ahmed, G.H.* A review of "3D concrete printing": Materials and process characterization, economic considerations and environmental sustainability. Journal of Building Engineering, 66, 2023. p. 105863. **28.** *Rehman, A.U., Perrot, A., Birru, B.M. and Kim, J.H.* Recommendations for quality control in industrial 3D concrete printing construction with mono-component concrete: A critical evaluation of ten test methods and the introduction of the performance index. Developments in the Built Environment, 16, 2023. p. 100232.

Ярослав Гаращенко, Олена Гаращенко, Харків, Україна, Руслан Кучер, Миколаїв, Україна

ГЕОМЕТРИЧНА ТОЧНІСТЬ БЕТОННИХ СТІН, ВИГОТОВЛЕНИХ ЗА ДОПОМОГОЮ 3D-ДРУКУ

Анотація. *Представлені результати одержано при теоретичному і експериментальному дослідженні геометричної точності та параметрів якості поверхні бетонних стін, виготовлених за допомогою адитивних технологій. Пророблено теоретичні аспекти класифікації дефектів та відхилень поверхонь одержаних пошаровою побудовою бетоном. У дослідженні розглядається вплив товщини шару на точність друку та утворення дефектів у процесах 3D-друку бетоном. Було виготовлено два експериментальні зразки з різною товщиною шару: 20 мм та 15 мм. Були проведені систематичні вимірювання для оцінки глибини тріщин на вертикальних поверхнях, глибини пор на горизонтальних поверхнях, варіацій ширини доріжки та відхилень від*

прямолінійної геометрії. Експериментальна методологія включала комплексні протоколи вимірювань з використанням точних приладів для оцінки геометричних параметрів та характеристик якості поверхні. Був проведений статистичний аналіз для кількісної оцінки взаємозв'язків між товщиною шару та точністю друку, включаючи розрахунки середніх значень, стандартних відхилень та коефіцієнтів варіації для всіх виміряних параметрів. Результати демонструють значне покращення геометричної точності при зменшенні товщини шару з 20 мм до 15 мм. Глибина тріщин на вертикальних поверхнях зменшилася на 56%, тоді як відхилення від прямолінійної геометрії покращилися на 32%. Найбільш помітним є значне покращення стабільності ширини колії, коефіцієнт варіації покращився на 91%, що свідчить про суттєве покращення повторюваності процесу. Конфігурація з товщиною шару 15 мм продемонструвала чудову продуктивність за всіма виміряними параметрами, демонструючи покращену адгезію шарів, зменшення дефектів поверхні та покращену розмірну стабільність. Коефіцієнт варіації глибини тріщин зменшився з 43% до 24%, а мінливість відхилення зменшилася з 32% до 12%, що підтверджує покращений контроль процесу та передбачуваність. Ці результати дають цінну інформацію для оптимізації параметрів 3D-друку бетону та встановлення протоколів контролю якості для адитивного будівництва. Дослідження сприяє розробці стандартизованих практик технології 3D-друку бетону та демонструє критичну важливість оптимізації товщини шару для досягнення високоякісних друкованих бетонних конструкцій. Результати підтверджують ефективність впровадження тонших шарів, при умові підвищених вимог до геометричної точності та якості поверхні в автоматизованих процесах будівництва бетоном. Це дослідження було проведено на базі ТОВ "Геополімер" з метою впровадження інноваційних технологій у будівельній галузі.

Ключові слова: *3D-друк бетоном; будівництво; оптимізація товщини шару; геометрична точність; контроль якості поверхні; оцінка якості; аналіз дефектів бетону.*

CONTENT

Наукове видання

РІЗАННЯ ТА ІНСТРУМЕНТИ
в технологічних системах

Збірник наукових праць

Випуск № 102

Укладач *д.т.н., проф. І.М. Пижов*
Оригинал-макет *А.М. Борзенко*
Відп. за випуск *к.т.н., проф. Є.В. Островерх*

В авторській редакції

Матеріали відтворено з авторських оригіналів

Підп. до друку 27.06.2025.Формат 60х84 1/16. ПапірСоруРарег.
Друк - ризографія. Гарнитура Таймс. Умов.друк.арк. 10,93. Облік.вид.арк. 11,0. Наклад 30 прим.
1-й завод 1-100. Зам. № 1149. Ціна договірна.

Видавничий центр НТУ «ХПІ»
Свідоцтво про державну реєстрацію ДК № 116 від 10.07.2000 р.
61002, Харків, вул. Кирпичова, 2